Dissertation

Local Lorentz Force Velocimetry
for liquid metal duct flows

Zur Erlangung des akademischen Grades Doktoringenieur (Dr.-Ing.)
vorgelegt der Fakultät für Maschinenbau
der Technischen Universität Ilmenau
von

M.Sc. Christiane Heinicke

geboren am 25. November 1985 in Wolfen, Deutschland

Abstract

Metal melts are typically hot, aggressive, and opaque, and are therefore inaccessible to conventional flow measurement techniques. Lately, a non-contact technique has been developed, termed Lorentz Force Velocimetry (LFV), which is based on the interaction of an electrically conductive moving fluid with a magnetic field. The magnet providing the field experiences a Lorentz force which can be detected and depends on the velocity of the moving metal.

Standard LFV has been studied in detail and is now operational under industrial conditions. However well working, the standard LFV is designed for volume flux measurements with large magnet systems and therefore cannot resolve local velocity disturbances as might be caused by sharp bends in the flow or deposits on the pipe wall. The thesis at hand bridges that gap and extends Lorentz Force Velocimetry to the locally resolved measurement of flow velocities with a small magnet. It shows that the claim of *local* measurements is appropriate although the magnetic field employed is generally unbounded.

Several experiments are performed to achieve this goal. All have in common that a Lorentz Force Flow meter (LFF) is equipped with a permanent magnet whose dimensions are significantly smaller than that of the duct flow under investigation. The working fluid is the eutectic alloy GaInSn which is liquid at room temperature.

A first preliminary setup uses a rectangular duct and a strain gauge-based force measurement system to prove that the principle of local LFV is feasible and the tiny forces involved can indeed be detected. The results from this setup have been used to design the more sophisticated main setup with a square duct and an interference optical force measurement system.

The obtained force profiles provide a database for validating future numerical simulations. More importantly, certain modifications to the flow help characterize the scope of the local LFF: (1) A laminar flow can reliably be distinguished from a turbulent flow. (2) The maximum of the mean flow can be located. (3) Two close jets can be readily distinguished despite the generally infinitely extending magnetic field. (4) Temporal resolution is sufficient to identify regions of particularly high turbulence and vortex shedding.

Zusammenfassung

Metallschmelzen sind heiß, chemisch aggressiv und undurchsichtig, und damit für konventionelle Strömungsmessgeräte unzugänglich. Die neu entwickelte Lorentzkraft-Anemometrie (LKA oder LFV) umgeht diese Probleme, da sie die berührungslose Messung von Strömungsgeschwindigkeiten in elektrisch leitfähigen Flüssigkeiten mit Hilfe von Magnetfeldern erlaubt. Dabei ist die Wechselwirkung zwischen dem eingesetzten Permanentmagneten und der leitfähigen, bewegten Flüssigkeit ein Maß für die Geschwindigkeit der Metallschmelze.

Die Standard-LKA wurde bereits ausgiebig untersucht und wird für den industriellen Alltag entwickelt. Bisher beschränkte sich die LKA auf Volumenstrommessungen; Störungen des Geschwindigkeitfeldes, wie sie nach Knicken im Strömungskanal oder durch Ablagerungen an der Kanalwand entstehen, konnten bislang nicht aufgelöst werden. Diese Lücke wird mit der vorliegenden Arbeit geschlossen und die Standard-LKA um die Möglichkeit der lokal aufgelösten Geschwindigkeitsmessung erweitert. Insbesondere wird belegt, dass *lokale* Messungen mit der LKA trotz der prinzipiell unendlichen Ausdehnung des Magnetfeldes möglich sind.

Zu diesem Zweck werden verschiedene Experimente durchgeführt. In allen wird ein Lorentzkraft-Anemometer (LFF) mit einem Permanentmagneten ausgestattet, der deutlich kleiner ist als die typischen Längenskalen der zu untersuchenden Strömung. Das Arbeitsmedium ist die bei Raumtemperatur flüssige Legierung GaInSn.

Mit einem Vorexperiment wird gezeigt, dass die winzigen erzeugten Kräfte tatsächlich aufgelöst werden können. Die Erkenntnisse aus dem vorläufigen Aufbau flossen in den Aufbau des Hauptexperiments, das aus einem Kanal mit quadratischem Querschnitt und einem interferenzoptischen Kraftmesssystem besteht.

Die erhaltenen Kraftprofile dienen der Validierung von zukünftigen numerischen Simulationen. Wichtiger ist jedoch die Charakterisierung der Anwendungsbereiche des lokalen LFF mit Hilfe bestimmter Modifikationen des Strömungsprofils: (1) Laminare Strömungen können von turbulenten Strömungen unterschieden werden. (2) Das Maximum der mittleren Strömung kann lokalisiert werden. (3) Zwei benachbarte Strahlen können trotz des prinzipiell unendlichen Magnetfelds voneinander unterschieden werden. (4) Die zeitliche Auflösung ist ausreichend um Bereiche besonders hoher Turbulenz und Wirbelablösung zu identifizierern.

Contents

1 Introduction

1.1 Motivation

There literally exist dozens of methods to measure the bulk velocity of a moving liquid [1, 2]. They can be categorized into mechanical flow meters, pressure-based flow meters, optical flow meters, thermal flow meters, and electromagnetic flow meters to name the most important ones. Except for the optical flow meters, they all require mechanical contact to the fluid.

A very simple example of a mechanical flow meter [1, 3] is the windmill type or propeller flow meter, whose vanes are set into rotation by the oncoming fluid. The rotation speed is a direct measure of the fluid velocity. Pressure-based flow meters [3] either measure a pressure difference or the static pressure to derive the dynamic pressure and thus the fluid velocity from Bernoulli's equation. Such a static pressure meter is the Pitot-tube, a hollow tube with one opening pointing into the fluid flow.

Thermal flow meters like the hot-wire anemometer [4, 5] generally make use of the fact that the resistance of a wire depends on its temperature. When the hot-wire anemometer is heated to some temperature above the ambient temperature, it is cooled down by the passing fluid, and the resistance of the wire gives a measure of the velocity of the fluid. The rather delicate wire restricts this flow meter to low-density fluids like air.

The only classical techniques that do not require contact to the fluid are the optical techniques, like Laser Doppler Anemometry (LDA) [6] or Particle Image Velocimetry (PIV) [7]. In LDA, the Laser light is scattered by natural or injected particles in the fluid, and the Doppler shift caused by the movement of these particles is a direct indicator for their velocity. In PIV, a series of images of the reflecting light from the particles is used to obtain vector maps of the fluid. Both techniques, however, require the fluid to be translucent to work.

Now, this brief introduction to classical flow measurement techniques illustrates one if not the major problem of flow measurement inside metal melts: Imagine a fragile device like a hot-wire anemometer or even a relatively sturdy propeller flow meter inside a flow of molten steel. At temperatures well beyond $1000\,°C$, any measurement device submerged in the flow will be either molten or dissolved in a matter of seconds [8]. Non-contact optical techniques do not present an alternative, since metals are opaque.

Fortunately, there do exist solutions to measure flow velocities inside molten metals. Most of them make use of the typically high conductivity of metals and their strong interaction with magnetic fields, as will be detailed in chapter 2. As a result, these techniques do not require direct contact with the fluid under investigation. Particularly Lorentz Force Velocimetry (see next section), a newly developed electromagnetic technique, has found its way into industrial aluminum and steel plants as a contactless flow meter [9, 10].

However, it is necessary to know not only the volume flux of the metal, but also local flow patterns in a number of industrial metal flows (e. g. [11]) and even more so in laboratory metal flows [12, 13]. Intuitive examples are questions like whether there is vortex shedding behind a bend or a solid obstacle, or if the flow is obstructed by deposits on the duct walls.

This thesis is aimed at laying the foundation for the measurement of spatially resolved flow velocities inside metal melts that are inaccessible to most other flow measurement techniques. It extends the previous works on Lorentz Force Velocimetry (see section 2.4) by downscaling the up to now solely volume flux measurement technique. Based on experimental investigations, the thesis at hand will prove that it is possible to resolve local flow structures with a magnetic field that is intrinsically unbounded.

Almost as a side effect, detailed parametric studies are undertaken to pave the way for this ambitious aim. They will serve as a database for the validation of numerical simulations [14, 15] and for the refinement of the theory of the interaction between a magnet and the flow of an electrically conductive fluid [16, 17].

1.2 Lorentz Force Velocimetry (LFV)

When an electrically conducting fluid is exposed to a magnetic field (see fig. 1.1a) that can be provided by either a permanent magnet or an electromagnet, there will be eddy currents generated inside the fluid [18] (fig. 1.1b). By Ampère's law [18], the eddy currents in turn give rise to a secondary magnetic field (fig. 1.1c). As a result, the Lorentz force acts to brake the flow (fig. 1.1d). This effect is well known [19, 20, 21] and can be observed with a simple, magnetic-brake type experiment [22].

Lorentz Force Velocimetry (LFV) makes use of Newton's third law, which states that each force is paired with a counterforce of the same magnitude; in this case the braking force on the fluid is accompanied by an accelerating force on the magnet (see fig. 1.1d). The magnitude of the force depends linearly on the volume flux of the fluid [23], making the principle suitable for flow measurement.

1.3 Objective and overview of this thesis

So far, Lorentz Force Velocimetry has been used with large magnet systems whose fields penetrate deeply into the flow. However, one of the major practical problems of LFV is that the magnetic fields decay very rapidly, giving rise to only tiny forces on the magnet system. This shortcoming is the basis for the idea to extend LFV to local velocity measurements: If the magnetic field imposed on the flow is localized like that of a magnetic dipole instead of as far-reaching like the magnet systems employed so far, the magnet surely "sees" only a small fraction of the fluid volume in its vicinity. That is, forces generated farther away are too weak to significantly contribute to the total force on the magnet. Two important questions remain: How much fluid volume belongs to the "vicinity" of the magnet, or equivalently, how fine is the spatial resolution that can be achieved with the generally unbounded magnetic field? And, can the local velocity field be uniquely reconstructed from the force on the magnet?

(a)

(b)

(c)

(d)
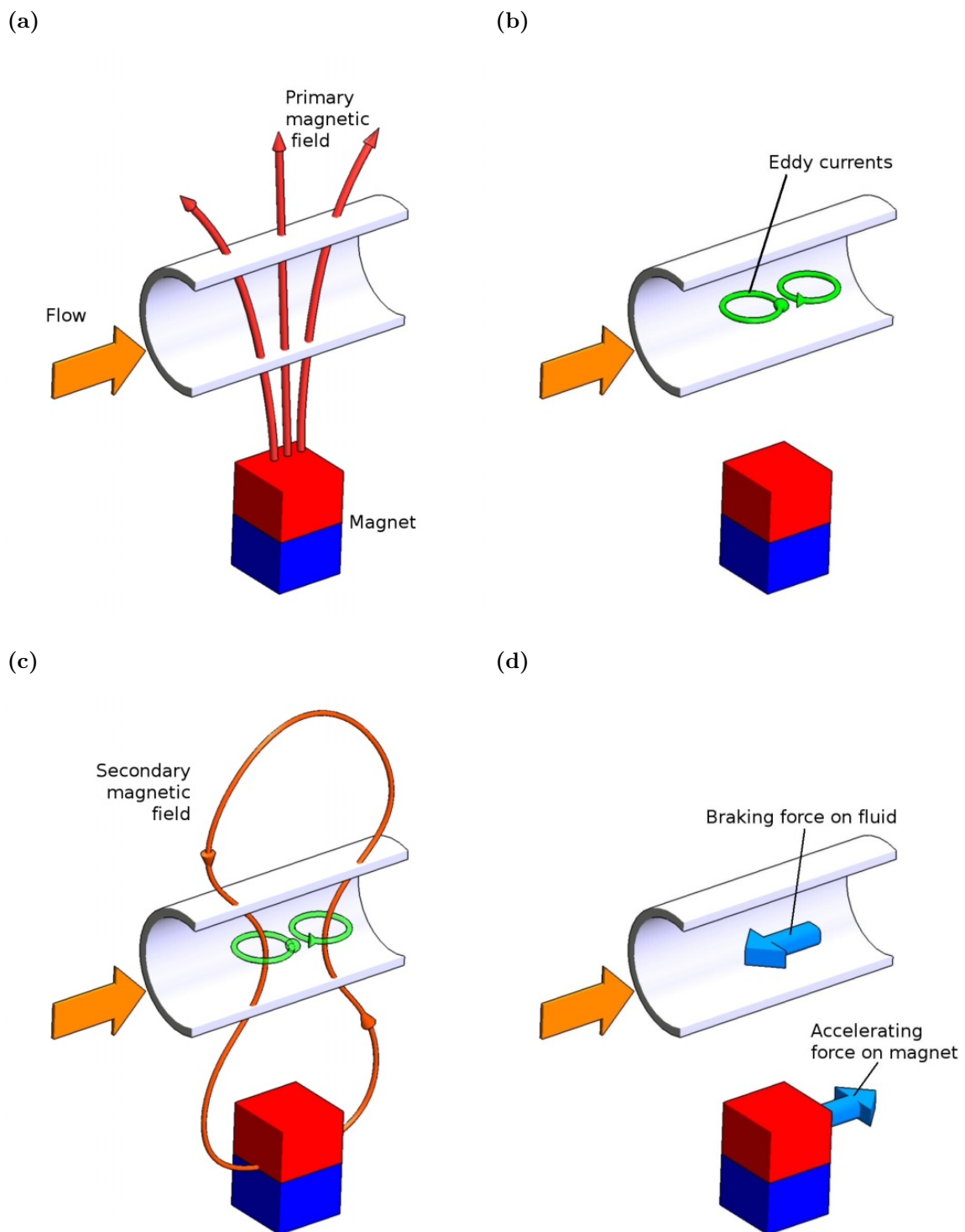
Figure 1.1: The working principle of Lorentz Force Velocimetry. (a) An electrically conductive fluid is exposed to a magnetic field. (b) The magnetic field induces eddy currents inside the fluid. (c) The eddy currents give rise to a secondary magnetic field. (d) A braking force on the fluid results, which is matched by an accelerating force on the magnet. Graphics provided by the Institute of Thermodynamics and Fluid Dynamics, Ilmenau University of Technology.

While the second question must be left open for the future, as a general solution of the inverse problem is beyond the scope of this thesis, the first question will be answered.

The object of investigation is a liquid metal flowing through a straight square duct at room temperature. Flow measurements are performed with a Lorentz Force Flow meter (LFF) placed beside the duct flow. Compared to the dimensions of the duct (5 cm wide), the magnet of the flow meter is significantly smaller (a cube of 1 cm edge length).

The following chapter 2 provides a background to basic concepts used throughout this thesis. First, a selected overview is given of both purely hydrodynamical duct flow and magnetohydrodynamics. Then, after focusing on the flow itself, attention is shifted to the flow meter. The second half of chapter 2 presents a more detailed introduction to the state of the art in flow measurement inside metal melts, with special emphasis on recent developments in Lorentz Force Velocimetry.

Chapter 3 presents the two experimental setups that have been used throughout this thesis. That is, a preliminary setup is described that consists of a rectangular duct with a $21.6\,\mathrm{cm}^2$ cross section and a strain gauge-based force measurement system, followed by an improved setup with the $25\,\mathrm{cm}^2$ square cross section mentioned above and an interference optical force measurement system.

The results from the first setup are presented in chapter 4. The preliminary setup is used to prove for the first time that the tiny forces involved with the small permanent magnet can indeed be detected.

In chapter 5, the results from the second and main setup are presented. Three variable parameters determine the magnitude of the measured force: the distance z of the magnet to the duct, the spanwise position y of the magnet relative to the duct, and – essential for a velocimeter – the velocity v of the liquid metal. Chapter 5 presents the results of the parameter studies for the unperturbed metal flow, as well as the modifications to the flow and the resulting force profiles that lead to the claim of a local resolution of LFV. Therefore, that chapter, and section 5.3 in particular, may be considered the heart of this thesis.

The final chapter 6 summarizes the major findings of this thesis and gives a brief outlook on future steps to be undertaken.

2 Background

This chapter is intended to give a brief introduction to the fluid dynamics of duct flows, (1) in the purely hydrodynamical case with no external magnetic field and (2) in the magnetohydrodynamical case where the fluid is exposed to an external magnetic field. After these first two sections, the attention in the second half is shifted to the measurement of fluid dynamical quantities in the special case when the fluid is a liquid metal. While the first two sections are necessary to understand the experimental setup and its different modifications in chapter 5, the third section gives a more thorough motivation to why yet another electromagnetic flow measurement technique (LFV) is developed, and the fourth section discusses recent advances in LFV besides the extension to local velocity measurement.

2.1 Hydrodynamic duct flow

Compared to pipe flows, duct flows have been studied relatively scarcely. Nonetheless, they provide room for some interesting flow behavior not found in pipes.

2.1.1 Velocity profiles in square ducts

The velocity profile of a purely hydrodynamic flow through a duct with no external magnetic fields and no disturbances depends on only one parameter: the *Reynolds number Re*. Defined as

$$Re := \frac{vL}{\nu},$$

the Reynolds number is a measure for the ratio of inertial forces and viscous forces inside the fluid. For a thorough elaboration on the Reynolds number see textbooks on fluid dynamics like [25] or on magnetohydrodynamics, like [19, 20, 21]. For the purpose of this thesis it is sufficient to remark that for a fixed length scale L and a fixed kinematic viscosity ν (as is the case in the experiments presented later), there exists a critical velocity v_{crit} below which the flow will be laminar, and above which the flow will be turbulent.

For duct flows, there is not (yet) consensus on the critical Reynolds number, claims on the matter range from 1678 [26] to 2060 [27]. Investigations on pipe flows have shown that turbulence has a "finite lifetime" [28], no matter how high the Reynolds number, but that at $Re > 2040 \pm 10$ turbulent "puffs" are generated faster than they decay [29, 30]. Pipe and duct flows are considered close enough that the critical Reynolds number for duct is expected to be in the vicinity of that for pipe flows [31]. Since puffs could be detected as low as at $Re = 770$ [32], the part of the experiments in this thesis that is focused on laminar flow is conducted at $Re \leq 750$.
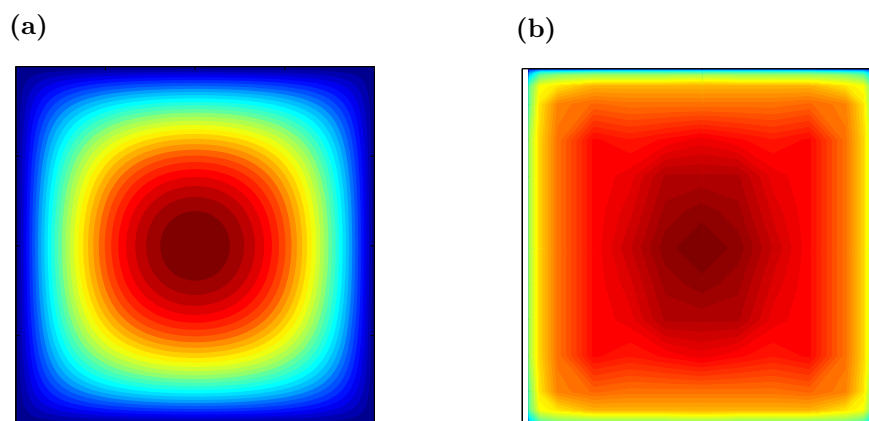
(a) **(b)**

Figure 2.1: Laminar (a) and turbulent (b) iso-velocity contours for a square duct, normalized to $v_{max} = 1$. (a) Result of a direct numerical simulation at $Re = 2000$, courtesy of S. Tympel. (b) Experimental data at $Re = 14,600$, taken from [24]. White stripes mark missing data points. Hoagland [24] actually only measured the lower left quadrant; the figure shows the quadrupled data for easier comparison with (a).

Even this restriction does not ensure that the flow profiles inside the liquid metal duct will be fully developed either laminar or turbulent. Typical hydrodynamic experiments employ test sections several meters long to let the flow develop (e.g. [24, 33]) – for comparison, the test section employed in the experiment presented here is only $\sim 40\,\text{cm}$ long before the measurement position and has a highly disturbed inlet.

For a laminar flow, the velocity distribution can be described analytically, the solution is an infinite series [34]. Fig. 2.1a visualizes such a laminar duct profile; though this has been obtained from direct numerical simulations (DNS) by S. Tympel. One can see how the isolevels of the velocity become more and more circular towards the center of the duct. The turbulent profile is shown for comparison (fig. 2.1b). It has been measured by Hoagland [24] with a hot wire anemometer inside an air flow. Directly at the wall, there is the thin boundary layer which decreases in thickness with increasing Reynolds number (apparent in the full data set of [24], but also textbook knowledge [25, 35]). Outside the boundary layer, the velocity increases faster towards the middle of the duct than in the laminar case, but the centerline velocity is significantly reduced compared to that of a laminar flow of the same volume flux.

The line profiles at mid-height of the above two velocity distributions are shown for comparison in fig. 2.2 in addition to two numerically calculated turbulent profiles. Note that here the velocities are normalized such that the volume flux is the same in all profiles.

Whereas the laminar flow inside a pipe is described by a parabola, the line profile of a laminar duct flow is best fitted by a fourth order polynomial. On the other hand, the turbulent (mean) profile v inside a pipe can be described by a sum of natural logarithms of the distance y to the pipe wall at $y = R$

$$v = C_1 \left[-\frac{1}{2} ln \left(1 + \sqrt{1 - \frac{y}{R}} \right) + \frac{1}{2} ln \left(1 - \sqrt{1 - \frac{y}{R}} \right) + \sqrt{1 - \frac{y}{R}} \right] + C_2 \quad [35].$$
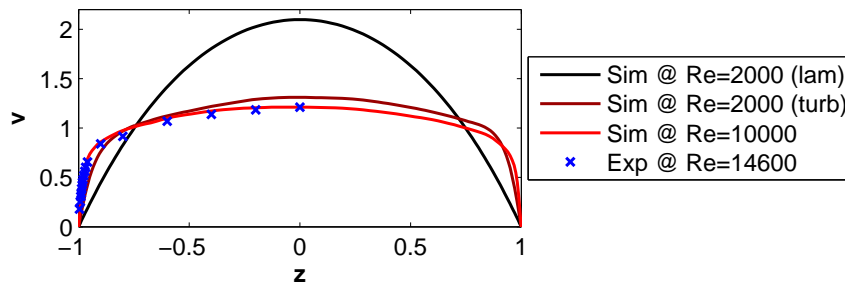
Figure 2.2: Comparison of a laminar velocity profile ($Re = 2000$, DNS without disturbances) and turbulent velocity profiles inside the square duct ($Re = 2000$ and 10000, DNS with imposed disturbances, and $Re = 14,600$, experiment [24]). Velocities are normalized such that the volume flux is equal for all profiles. Numerical data courtesy of S. Tympel.
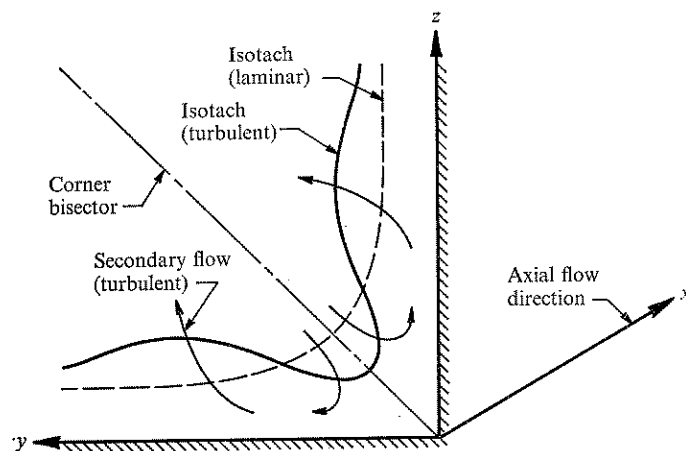
Figure 2.3: Qualitative flow pattern in the corner of a square duct indicating lines of constant velocities (isotachs). Taken from [41].

With the right constants C_1 and C_2, this curve also fits Hoagland's data for the centerline velocity. Other reasonable fits are a 10th order polynomial or the *one-seventh power law* ($v \sim (y/R)^{(1/n)}$, where n is typically 7 for many engineering applications, [31, 36]), although the latter displays some significant deviations from the experimental data.

2.1.2 Secondary flow

Secondary flow (of Prandtl's second kind) is restricted to turbulent flow through non-circular cross sections, i.e. it is never found in laminar flows [37, 38] nor in any (circular) pipe flow [33]. It was first discovered indirectly by Prandtl's student J. Nikuradse who observed a peculiar deformation of the lines of constant axial velocity inside non-circular ducts (see fig. 2.3) that could not be explained without the secondary flow [39, 40].

It then took over thirty years of progress in flow measurement techniques, until Hoagland [24] was able to quantitatively describe the secondary flows. The following description is taken from his PhD thesis (chapter 4, data presentation and interpretation):

"[...] the streamlines representing the mean flow are very nearly parallel to the duct axis but actually follow somewhat distorted helical paths wherein a fluid particle beginning near the

duct center moves gradually toward one of the corners, and upon approaching closely to the corner, turns and moves slowly out along one wall and finally returns to the center region. The streamlines are so nearly axial that the mean velocity vector at any point is essentially equal in magnitude to the axial component (with negligible error)."

Indeed, the magnitude of the secondary flow was determined by him to be about one percent of the primary flow. Later, more measurements have been performed [33, 41, 42] with increasing precision. One hot candidate for the origin of the corner flow is the gradient in the Reynolds shear stresses normal to the corner bisectors, but this theory is still being debated [43, 44]. For numerical simulations, the secondary flow proves to be a practical benchmark test (e.g. [43]).

To conclude, it was hoped that the secondary flow inside the square duct would cause a clearly measurable signal. However, two factors are opposed: First, the weak magnitude of the secondary flows, and second, probably more importantly, all cited experimental works observed the secondary flows in fully developed flows, several meters behind the inlet ([24, 33, 42]; Gessner [41] does not quote a length, but at least a sophisticated inlet). As stated earlier, the duct used throughout this work is simply too short to let the flow develop. However, considering the high resolution of the force measurement system (see section 3.4), it might be possible to detect secondary flow in longer ducts.

2.1.3 Flow around a solid obstacle

The hydrodynamic duct flow profile is the basis for understanding the experiment on the liquid metal duct flow presented in this thesis. The force measurements performed on the unperturbed duct flow lead to the database for the numerical simulations (cf. chapter 1). However, to support the claim of the local resolution of LFV certain modifications to the flow are necessary. One of these is the introduction of a solid circular cylinder, which causes perturbations to the flow detailed in this section and that can be detected by the local LFV (cf. section 5.3).

The flow around a circular cylinder has been studied for over a hundred years starting with Strouhal in 1878 [45], yet no underlying theory has been found and knowledge about the flow is still "empirical" and "descriptive" [46]. The first to visualize and investigate the wake behind the cylinder was von Kármán, followed by Prandtl [47] and others. At velocities relevant for the present work ($Re \sim 5000$), the wake behind the cylinder is a fully turbulent vortex street as shown in fig. 2.4.

The frequency f_s at which the vortices are shed is typically described by the non-dimensional Strouhal number $St = f_s d/v$ [48], with D as the diameter of the cylinder. At Reynolds numbers around a few thousand, the Strouhal number was found to be approximately 0.21 [49]. If $d = 13\,\text{mm}$ and $v = 10\,\text{cm/s}$ (cf. chapter 5), then the shedding frequency is around 1.5 Hz.

Ong and Wallace [50] measured the mean velocity and velocity fluctuations behind a cylinder at a Reynolds number comparable to the one investigated here. At the centerline of the cylinder, the mean velocity drops to a minimum of about 65% of the free stream value (at a distance $x/d = 3$ behind the cylinder) and 75% ($x/d = 4$), respectively. The velocity fluctuations are found to have a maximum both at the height of the upper and the lower edge, reaching 24% and 22% of the free stream velocity at the above distances. A (local)
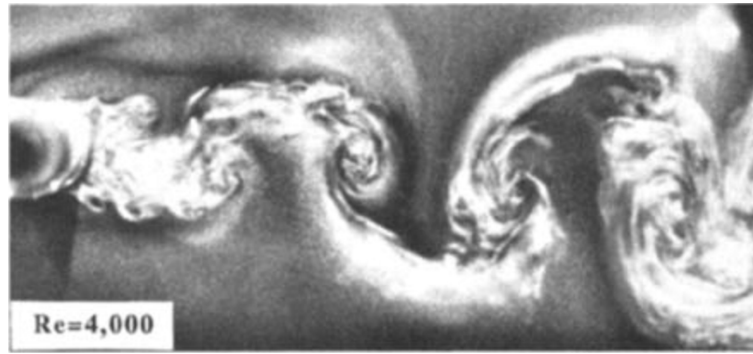
Figure 2.4: Experimental observation of the turbulent wake behind a circular cylinder. Photograph taken from [46].

minimum in velocity fluctuations is found at the centerline and is of the order of 17% of the free flow (cf. fig. 10 in [50]). When the cylinder is not exactly placed in the middle between top and bottom wall of the duct, the vortex street is found to be asymmetric [51], and consequently the two velocity maxima are not of the same magnitude, but still of the same order as stated above.

2.2 Magnetohydrodynamics

Magnetohydrodynamics is the study of flows of electrically conducting fluids that interact with magnetic fields. Unlike the name suggests, the typical MHD fluid is not water (-*hydro*-), but rather a metal melt (highly conductive) or even a glass melt or electrolyte (poorly conductive). Bordering on the more general plasma physics, magnetohydrodynamics also comprises low-density particle flows in outer space interacting with both intrinsic and extrinsic, planetary magnetic fields [21, 52, 53].

The following section elaborates on two examples of typical magnetohydrodynamic (MHD) flows. The first example is a typical industrial flow problem, intended to illustrate why it is not always sufficient to know the volume flux of a flow but rather information on local flow structures is necessary. The second example extends the scope of MHD beyond technical applications and gives an insight into a naturally occurring MHD flow. It might seem that the natural MHD flow is quite far from flow measurement inside molten metals. However, as is often the case in physics, the basic concepts underlying both phenomena are the same, albeit they occur at vastly different length scales.

2.2.1 An industrial example of MHD[1]

Steel bars are produced by melting a certain amount of steel, adding some elements to manipulate the material properties of the final product and by then casting the melt into the desired shape. If the melt was merely poured into the cast, the cooling and solidification would require a significant amount of time and result in an inhomogeneous melt and imperfections in the final product.

---

[1]This section is based on [54].

Instead, electromagnetic mixers are placed at the top of the mold. When the steel is now poured into the mold, it passes the electromagnets of the mixer and is deflected from its straight downward path towards the horizontal. The change in direction of the melt leads to a change in the direction of the force on the melt, the result being the melt spiralling down the mold.

While requiring additional power, the electromagnets homogenize the melt not only regarding its components but also regarding its temperature. Thus, the mixers not only help remove inclusions but they enhance the transfer of heat out the steel cast and reduce the time until the steel solidifies.

2.2.2 A natural example of MHD

A prominent and visible example of a naturally occurring MHD flow are the so-called Polar Lights, also known under the name Aurora Borealis (northern hemisphere) and Aurora Australis (southern hemisphere), or simply Aurora [56, 57, 58].

The Sun continuously ejects a considerable amount of charged particles. These form a plasma; that is, they interact with each other, carry along with them a magnetic field and react to external magnetic fields. Although MHD theory incorporates significant simplifications, the plasma emitted from the sun can be reasonably well described as a conductive fluid composed of two particle species, namely protons and electrons [59].

The plasma takes about 2 days to reach Earth, depending on its exact speed [60]. Once it gets close, it is abruptly decelerated by the magnetic field of the Earth. In effect, the Earth's magnetic field is deformed: it is compressed on the day-side and stretched into a tail on the night-side of the Earth [55]. As the mass flux from the sun is not a constant stream, the magnetotail pointing away from the sun is not steady but rather flaps like a flag in the wind [61].

The Earth's magnetic field effectively poses an obstacle to the flow of charged particles, most of the plasma is forced to flow around the Earth's magnetic field like it would for a solid obstacle. Through a process that is not yet fully understood [62, 63], the plasma diffuses into the magnetotail on the night side of the Earth [61, 64]. There, the charged particles preferably move along the magnetic field lines. Due to the magnetic field forming the shape of a bottleneck towards the poles, the particles are accelerated towards Earth's surface [59]. On the way, they encounter the second obstacle: Earth's atmosphere.

Hit by the plasma from the sun, the atmosphere acts like a neon tube. If nitrogen atoms or oxygen atoms are hit by an electron or ion, they enter an excited state. Being eager to return to a lower energy state, the atoms emit photons whose wavelength corresponds to the energy of the incoming plasma. Through the color and the altitude of the resulting light, the Aurora is a direct indicator for that energy [60]. For example, if the plasma is rather slow, the Aurora will be reddish and at high altitudes, because the plasma lacks energy to penetrate deeper into the atmosphere. Faster high-energy plasma generates greenish Aurorae at low altitudes, sometimes with a purple-white lower edge to them [58, 60].
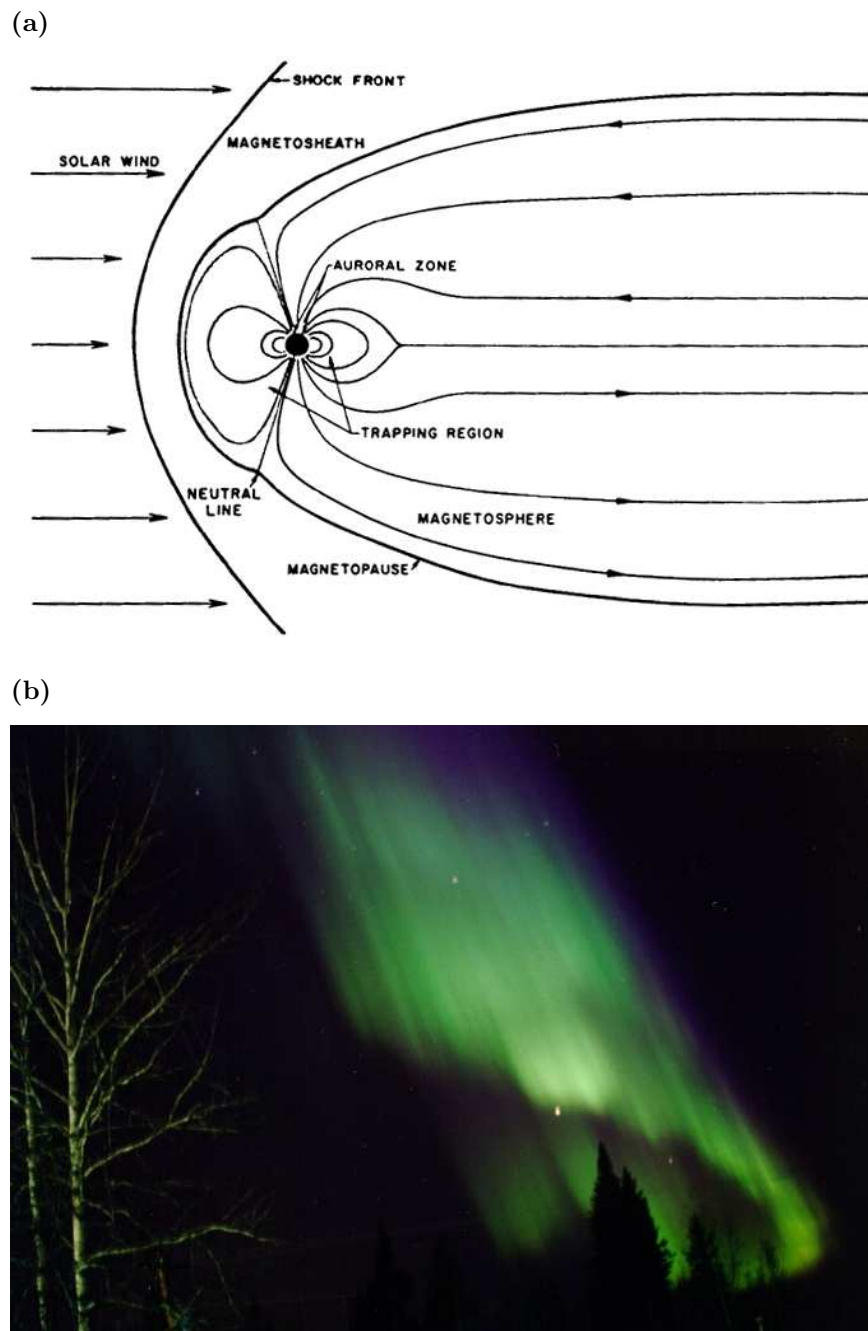
Figure 2.5: The Aurora. (a) Graphic of its formation. The solar wind "blows" on the obstacle posed by the Earth's magnetic field and deforms it. After passing the Earth, the solar wind particles enter the magnetic field through the magnetotail. From there they are accelerated along the field lines towards the polar regions of the Earth, where they ignite the Aurora. Taken from [55]. (b) Photograph of an Aurora Borealis, taken by J. Curtis.

2.2.3 Set of equations for liquid metal MHD

After this rather general excursion, the remainder of this section is explicitly restricted to the magnetohydrodynamics of liquid metals. The setup investigated in this work is the flow of a high-conductivity liquid metal through a square duct under the influence of the field of a permanent magnet. Temperature gradients are thought to be negligible. These restrictions justify certain simplifications compared to the full physical description of general MHD flows. For example, the speeds relevant here are non-relativistic, and the imposed magnetic field is assumed not to be significantly deformed by the flow of the metal [21].

Then the full set of steady-state MHD equations is for the fluid domain with the simplifications relevant to the particular physical setup considered in this thesis [20]:

- Electromagnetic equations:

$$\nabla \cdot \vec{B} = 0 \tag{2.1}$$

$$\nabla^2 \vec{B} = 0 \tag{2.2}$$

$$\vec{j} = \sigma(\vec{E} + \vec{v} \times \vec{B}) \tag{2.3}$$

$$\nabla \cdot \vec{j} = 0 \tag{2.4}$$

$$\nabla \times \vec{E} = 0. \tag{2.5}$$

- fluid mechanics equations:

$$\nabla \cdot \vec{v} = 0 \tag{2.6}$$

$$\frac{\partial \vec{v}}{\partial t} + (\vec{v} \cdot \nabla)\,\vec{v} = -\frac{\nabla p}{\rho} + \nu \nabla^2 \vec{v} + \frac{1}{\rho}(\vec{j} \times \vec{B}) \tag{2.7}$$

with the following quantities: $\vec{B}$ ... magnetic flux density, $\vec{E}$ ... electric field, $\vec{j}$ ... electric current density, $\vec{v}$ ... velocity field, σ ... electrical conductivity, ν ... kinematic viscosity, and ρ ... fluid density.

Equation 2.1 is known as one of Maxwell's equations and states that magnetic fields are source-free. The magnetic field transport equation (2.2), sometimes called induction equation [20], generally describes the change in the magnetic field due to the fluid flow. Since the generation of magnetic field by stretching and/or advecting field lines ($\vec{v} \times \vec{B}$) is negligible in liquid metals [20], eq. 2.2 states that there is no diffusion of magnetic field lines into the fluid in the steady state: the characteristic time for the magnetic diffusion ($\mu\sigma L^2$, with μ being the magnetic permeability and L a characteristic length scale) is small compared to the transit time (L/v, v being the average of the velocity over time and space) of the fluid in the laboratory case. The ratio between the two times can be defined as the *magnetic Reynolds number $Rm := \mu\sigma vL$* [21]. This number is a measure of how strongly the imposed magnetic field is distorted by the metal flow. For the liquid metal duct Rm is on the order of $10^{-2} \ll 1$, as can be seen in the next chapter and from the overview of all parameters relevant to this work that is given in table A.1 at the end of this thesis (p. 91). Such a low Rm implies that the field of the permanent magnet is altered insignificantly.

Ohm's law (eq. 2.3) yields the current density $\vec{j}$ as the result of an existing electrical field $\vec{E}$ inside a moving conductor. Eq. 2.5 is Faraday's law for the case when the magnetic field is constant, where the electrical field is irrotational and can be described by an electric potential. The charge conservation eq. 2.4 closes the set of equations.

The two fluid mechanical equations are the continuity equation for incompressible fluids (eq. 2.6) and the momentum equation, also known as the Navier-Stokes-equation (eq. 2.7). A detailed derivation and explanation of the two equations can be found in [65] and [25]; [20] gives a brief review on the topic.

Equations 2.1-2.7 are coupled by the Lorentz force $\vec{F} = \vec{j} \times \vec{B}$. Fluid dynamically, the Lorentz force inhibits the fluid flow when the magnetic field is stationary. In the case of a transversal flow meter like the LFF, the Lorentz force density scales as $f \sim \sigma v B^2$ [17, 23], i.e. the Lorentz force is directly proportional to the velocity.

It is often convenient to analyze eq. 2.7 not directly but in its non-dimensional form [65]. The necessary non-dimensionalizing parameters are the aforementioned Reynolds number $Re = vL/\nu$ and the Hartmann number $Ha = BL\sqrt{\sigma/\rho\nu}$. The Hartmann number compares electromagnetic forces to viscous forces inside the fluid. Originally, the Hartmann number was defined according to the classic setup of Hartmann with a homogeneous magnetic field [66, 67]. Since the present thesis employs small permanent magnets of highly localized fields, it is more practical to define the Hartmann number based on the maximum flux density B_{max} inside the liquid metal realm.

The resulting constant coefficient to the non-dimensional Lorentz force $\tilde{\vec{F}} = Ha^2/Re\,\tilde{\vec{j}} \times \tilde{\vec{B}}$ in eq. 2.7 is termed the interaction parameter $N = Ha^2/Re$ [16, 20]. N can be understood as the ratio of electromagnetic to inertial forces, or, equivalently, as the ratio of the time it takes for the fluid to transit through the magnetic field compared to the characteristic time of the Joule dissipation [20]. Consequently, N can be quite large even in the laboratory experiment (here: up to ~ 60) when the fluid velocities are very small. The ranges of Re, Ha, and N covered by the experiments in this thesis can be found in table A.1.

2.2.4 Flow around a magnetic obstacle

It is commonly known that magnetic fields damp the motion of electrically conducting objects, the more the stronger the magnetic field is. When the moving object is a fluid, the fluid particles will tend to flow around the magnet, leading to flow patterns somewhat similar to that around a solid obstacle [68, 69]. These patterns are pronounced particularly in shallow ducts; in higher ducts the fluid finds a second way around the obstacle. If the magnet is placed below the duct, the fluid is forced away from the magnet towards the upper boundary because clearly the braking effect is stronger where the magnetic field is stronger.

Additionally, magnetic fields act as an inhibitor to velocity fluctuations [21, 70], although at times the effect is overestimated [71]. At any rate, when a large, strong magnet spans the entire width of the duct, it should be expected that both the mean velocity and the turbulent fluctuations are reduced in the vicinity of the magnet (cf. fig. 5.24).

2.3 Flow metering in liquid metals

Flow measurement inside liquid metals has been a target for research for decades, but no all-encompassing technique exists to this day. As has been explained in chapter 1, almost all classical flow measurement techniques are non-suitable for the highly reactive environment of metal melts. In contrast, the typically high conductivities of metals allow for other approaches basing on the eddy currents induced when the metal is moving through a magnetic field. The large electrical conductivities allow the currents to be strong enough to be detected in one way or the other. Indeed, all but one of the measurement techniques in use with metal melts rely on the electromagnetic forces active in moving metal melts. The following sections give a small introduction to these techniques and discuss their applicability to industrial metal melts.

2.3.1 DC electromagnetic flow meters

2.3.1.1 Historical prelude

Faraday's law states that electrical charges moving through a magnetic field feel a force – the Lorentz force – that is perpendicular to both the magnetic field and the original direction of movement. As this force is opposite for positive and negative charges, these are deflected into two opposite directions, effectively leading to a separation of charges. The resulting electrical field can be probed with two electrodes placed across that potential drop (cf. fig. 3.11a).

Electromagnetic flow meters use this principle by applying a primary magnetic field to the fluid and measuring the potential drop between two electrodes. The first to try to apply this method was Faraday himself. He made use of the Earth's magnetic field and tried to measure the velocity of the River Thames by hanging electrodes into the river water.

However, presumably because the river bed short circuits the signal Faraday failed with his experiment [72]. The first to successfully apply Faraday's idea to a natural MHD flow was Wollaston in 1851 [73], when he was able to measure the voltages in the British Channel induced by tides. And since then the method has evolved into an accepted means of measuring tidal flows in ocean water [74].

2.3.1.2 Inductive electromagnetic flow meter

Faraday's inductive flow meter type can be bought off the rack today and is routinely being used in fields as diverse as the mining industry, water metering, and even the hygienically high-demanding pharmaceutical or food industries. In size, today's flow meter ranges in diameter from 1 mm to 3 m, with flow rates from 1 l/h to 10^8 l/h [75]. The magneto-inductive flow meter has been vastly studied, physically [16], with regard to its practical applications [75, 76], and hard-core theoretically [77]. Its major problem is the contact resistance between the electrode and the fluid, even when the electrode is completely wetted by the metal. Especially regarding high-temperature metal melts, inductive flow meters fail because their electrodes cannot withstand the aggressive environment. The only solution to this problem is to devise measurement devices that work without contact to the fluid medium, like the following devices.

2.3.1.3 Lorentz Force Flow meter

The principle of the Lorentz Force Flow meter (LFF) has already been described in the intro-duction (section 1.2). An LFF employs permanent magnets that are placed in close vicinity to the flow under investigation. The Lorentz force mentioned earlier not only generates eddy currents in the fluid but also acts as a braking force on the fluid. By Newton's third law of reacting forces, there is an accelerating force on the permanent magnet. Though rather weak, this force is detectable and can be used as a measure for the velocity of the metal. A problem of the standard LFF is that the force signal also depends on the strength of the magnetic field and the electrical conductivity, making the principle not only highly dependent on the distance of the magnet to the melt, but also on the temperature and the exact composition of the metal [78, 79]. The method is described in more depth in the next section (2.4).

2.3.1.4 Rotary flow meters

The closest relatives of LFF are the rotary flow meters which also employ permanent magnets. The counterforce in LFV also acts on the magnets in a rotary flow meter, being weaker on the far side and thus creating a torque on the magnet. Instead of measuring the torque on the magnet directly (which is possible and planned as an improvement to the measurement system used in this thesis, see section 3.4.2), the angular velocity of the resulting rotation is used as a measure for the velocity. There are different geometries for a rotary flow meter, like the flywheel-type (described and tested by Shercliff [16], and re-embodied in [23]), or the single-magnet rotary flow meter [80, 81] that employs a cylindrical magnet magnetized perpendicularly to its axis. Both types have the advantage of being independent of the electrical conductivity and thus of the temperature of the melt. Moreover, by externally applying a rotation to the magnet, the flywheel can be used as an electromagnetic pump to drive the flow, as suggested by Bucenieks [82] and employed in the experimental setup of this thesis.

2.3.2 AC electromagnetic flow meters

2.3.2.1 Eddy current flow meters

To avoid the trouble involved with the degradation of the magnetic fields of permanent mag-nets at high temperatures, several techniques have been invented that base on electromagnets. The oldest of these techniques has been proposed by Lehde and Lang [83], originally consist-ing of three coils placed inside or outside the metal. Two coils supply the primary magnetic field that induces eddy currents in the metal. The flow then drags the eddy currents along, inducing a secondary, detectable magnetic field in the third coil. Important improvements since the original invention are the increase in the number of coils [84] and an optimization of the excitation frequency [85, 86]. Though mostly applied from outside, an eddy current flow meter can also be used as a probe and submerged in the metal [87].
One great advantage of the eddy current flow meter is that the flow disturbs not only the amplitude of the AC magnetic field but also its phase distribution. The feasibility of using the phase shift as an additional indicator for the flow velocity is proven in [88].

2.3.2.2 Contactless Inductive Flow Tomography

Contactless Inductive Flow Tomography (CIFT) is a method recently proposed [89, 90] and proven to yield some degree of spatial resolution inside a bulk flow. A CIF-tomograph comprises two Helmholtz coils that induce a weak alternating magnetic field inside the vessel to be investigated. The flow inside the vessel distorts the magnetic field and the deviation – about 1% of the primary field – is detected with a number of Hall sensors. By solving an approximately linear inversion problem, the velocity field inside the vessel can be reconstructed from the magnetic field distribution at the Hall sensors outside the vessel. Improvements have been made on the numerical approach to the inversion [91] and on the experimental technique itself [92] with the prospect of further improving the depth resolution by changing the frequency of the primary magnetic field. Moreover, the method has been successfully applied to the model of a continuous steel casting process; the flow field inside a steel slab could be reconstructed with a much reduced number of sensors [93].

2.3.3 Local probes

The above sensors are generally used for the measurement of volumetric flow rates, with the CIFT being the only exception in that it is possible to reconstruct the 3D velocity field inside the vessel. The following two probes are fully local, meaning that one single measurement provides information about the velocity in one small fraction of the fluid volume.

2.3.3.1 Permanent magnet probe

The permanent magnet probe (PMP) [94, 95], sometimes termed Vivès probe after its inventor [96], is in fact a miniature DC inductive flow meter with permanent magnets in diameter as small as 2 or 3 mm. In the PMP's simplest form, the magnet is held by at least two wires which also act as electrodes that pick up the eddy currents. Vivès probes can detect liquid metal velocities in the range from 0 to 10 m/s with a sensitivity of about 1 mm/s [96], provided that the signal is corrected for external magnetic fields and outside temperature gradients in a complicated calibration procedure [97, 98, 99, 100]. Considering molten metals, the upper limit of the fluid temperature is set by the Curie temperature of the magnet; 720 °C have been reached experimentally [96]. One of the most crucial problems of the PMP is the difficult wetting of the probe which is not yet fully understood [94] but necessary to ensure zero contact resistance between fluid and probe.

2.3.3.2 Ultrasound Doppler Velocimeter

Ultrasound Doppler Velocimetry (UDV)[101] is the only technique suitable for liquid metals that does not base on induction. Rather, a cylindrical probe emits an ultrasonic beam that is reflected off seed particles in the flow. The time shift between two echoes from the same particle is a measure for the velocity of that particle. Velocity information is sampled instantaneously at defined positions along the ultrasound wave path. In principle, a UDV probe can be used non-invasively, but it always requires contact with the fluid. By the use of wave guides it is possible to decouple the sensor from the fluid, like the 620 °C-metal melt

in [102]. As with the PMP, wetting of the sensor is crucial and sometimes not easy to realize. In particular, small air gaps inhibit the acoustic coupling of the sensor to the fluid and may attenuate the sound signal beyond detectability. All in all, both PMP and UDV are tricky techniques that require careful implementation and patient tuning of the parameters [95].

A UDV probe is used as a reference sensor in the experiments of this thesis, and therefore the UDV is described in more technical detail in section 3.6.2.

2.3.4 A sensor for high-temperature local velocity measurement

At the moment, it is impossible to measure local flow velocities inside a liquid metal at elevated temperatures with any flow measurement technique, especially in the range of the melting temperature of steel. The two local probes presented in section 2.3.3 (UDV, PMP) require to be wetted by the metal melt directly (immersed sensor) or indirectly (transmission of the signal through the channel wall). In the case of high-temperature metal melts, PMPs are impracticable because the casing material cannot withstand the reactive environment. UDV probes are unusable, because even if they can be made to withstand the high temperatures, it is highly questionable if the metal fully wets the pipe or open channel wall. The AC electromagnetic flow meters are capable of probing the flow from outside, but are then not suitable for local velocity resolution (eddy current flow meters) or they are highly specialized to a certain application (CIFT). So far, the latter technique has only been used on two experimental setups [90, 93] with one especially designed sensor setup each. With the inductive flow meter being ruled out because of its contact-requiring electrodes, the only techniques feasible to be downscaled to allow local flow measurements are the rotary flow meter and the Lorentz force flow meter. With the rotary flow meters still being relatively deep in their infancy, the LFF seems a good choice to be advanced to reach local velocity resolution. The general possibility to use LFV with a small magnet is proven in [79], and, in more detail, in chapter 4 of this thesis. Furthermore, Chapter 5 then proves that it is possible to infer information about the velocity field inside a duct flow with an LFF placed outside the duct.

2.4 Recent advances in Lorentz Force Velocimetry

The operating principle of LFV has already been described in the introduction and the previous section (1.2 and 2.3), this section is intended to give a short overview of the ongoing work closely related to this thesis.

After proving the feasibility of LFV for the measurement of velocities in laboratory metal melts [23, 9], the technique is being extended into three directions:

The first branch is the development of the laboratory low-temperature sensor into a device that not only withstands the high temperatures involved in the making of aluminum or even steel, but also outputs a reliable velocity signal despite the high noise levels in an industrial plant. Calibration of the LFF is essential. A quick and cheap calibration is performed with a solid bar moved at different velocities [103, 104], and a more accurate but also more complicated calibration facility is set up at the moment with liquid tin [105]. A laboratory calibrated flow meter has been successfully tested in aluminum plants [78, 9]. Particularly

Kolesnikov et al. [9] optimistically estimate their uncertainty in flow rate measurement to be 2.3 %. A variation of the LFF developed by C. Weidermann is underway for commercial application in steel plants [10, 106] with melting temperatures of up to 2000 K. To solve the problem of the temperature dependent conductivity, a time-of-flight LFF has been devised whose signal is independent of the electrical conductivity of the metal melt [107, 108].

Second, LFF is sought to be extended to all fluid materials. So far, only applications of LFV to laboratory and industrial metal melts have been presented, where the electrical conductivities are on the order of 10^6 S/m. However, glass melts and electrolytic solutions are equally important liquids, and unfortunately equally inaccessible to common flow measurement techniques. Having a conductivity of ~ 1 S/m, they are substantially harder to probe with LFV, but not impossible as has been shown recently by A. Wegfraß [109]. A special magnet system had to be designed to generate forces in the micro Newton range [110], and a measurement system was built as delicate as Cavendish's setup [111], in which lead spheres were hung to a thin torsion wire for the detection of Earth's gravitational constant.

And finally, the third branch extends towards downsizing the LFF to local velocity measurements, the goal of this dissertation which will be pursued on the following pages, and particularly in section 5.3.

2.4.1 The reverse of LFV: Lorentz Force Sigmometry

Up to now, it was presented how the velocity of a liquid metal can be determined by measuring the Lorentz force acting on a magnet system. It was always implicitly assumed that the strength of the magnetic field and the electrical conductivity of the liquid are known. However, what happens when the conductivity is not known or only to an insufficient accuracy?

With simulations becoming better resolved the limiting factor on the quality of predictions in metallurgy is the knowledge of the thermophysical properties of the metal [112, 113] which are often known with an uncertainty of 10% or higher [114, 115]. Particularly the electrical conductivity is of interest [116], because it determines the local skin depth in metal melts, which determines the energy efficiency for the electromagnetic processing of materials including the electromagnetic stirring mentioned earlier [54]. Electromagnetic flow measurement techniques base on the assumption that the electrical conductivity is known [16, 23]. On a more fundamental level, the knowledge of the electrical conductivity of a liquid metal allows to draw inferences about the electronic transport properties and the structural heterogeneity of the metal [117].

Why is the precise measurement of thermophysical properties so difficult in high temperature melts? There currently exist three methods for measuring the electrical conductivity, namely the four-probe method [8, 118, 119, 120], the rotating magnetic field method [121, 122, 123, 124], and the electromagnetic levitation method [125, 126, 127, 112]. The first two methods have the drawback that they require mechanical contact of the metal sample to the measuring device – a problem at high temperatures, where "everything reacts with everything else" [8]. The last method avoids this mechanical contact, but encounters a high number of disturbing side effects unless employed under costly micro-gravity conditions.

Lorentz Force Sigmometry (LOFOS), a technique the author co-invented [128], is an approach to overcome the problems mentioned above. It is related to Lorentz Force Velocimetry,
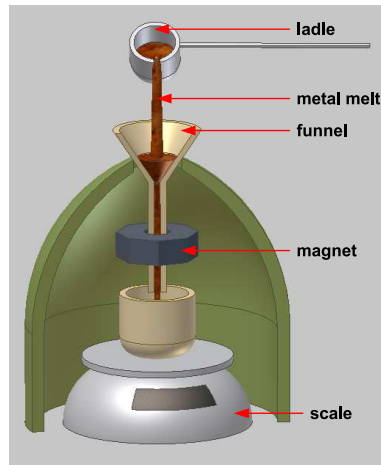
Figure 2.6: Principle sketch of the mobile LOFOS. The metal melt is poured into a funnel and then passes through a magnet system. Since the velocity of the melt is uniquely determined by the diameter of the funnel, the force measured on the magnet system is a direct indicator for the electrical conductivity of the melt by $F \sim \sigma v B^2$.

where the measured force is an indicator for the metal velocity ($F \sim \sigma v B^2$), but instead of knowing the conductivity σ and inferring the velocity v, in Lorentz Force Sigmometry a velocity field is prescribed and thus the conductivity can be inferred from the force. There exist three different implementations of the LOFOS-principle, but only the one most developed will be presented here.

The so-called *mobile LOFOS* is designed for collecting the thermophysical property data of a great number of different alloys. The focus is not on obtaining highly precise data, but rather on building a vast data base. Metallurgical plants offer a zoo of molten alloys that are routinely characterized chemically and the intention is that a robust and inexpensive mobile LOFOS is integrated as one further step of analysis. The coffeemachine-sized LOFOS (see fig. 2.6) is composed of a funnel and a force measurement system at the outlet of the funnel. The melt is filled into the funnel, passes through the magnet ring, generates the force on the magnet, and then pours into a receptacle placed on a scale. The receptacle can then be passed on to the laboratory for the usual analyses.

Unlike the other two LOFOS configurations, the mobile LOFOS has been put to test and successfully proven to work both in the laboratory and under industrial plant conditions with temperatures up to $T = 1300\,^\circ\mathrm{C}$ [129]. The measured values are found to be within 5% of the values stated in the literature. As a result, there is currently a patent pending for the idea [128].

3 Problem Definition and Experimental Setups

In this chapter, the physical problem under investigation is defined (section 3.1), followed by a definition of the relevant parameters (3.2).[1] These include the input parameters that can be adjusted in the experiments and the measured output parameters as well as some nondimensional parameters. The latter position this thesis relative to other liquid metal experiments and help to compare the experimental data with the theoretical works of S. Tympel and G. Pulugundla (projects A3 [14] and A4 [15] of the Research Training Group "Lorentz Force Velocimetry and Lorentz Force Eddy Current Testing").

During this project two experiments have been set up. Both comprise a horizontal duct system filled with a liquid metal that is driven by an electromagnetic pump. The setups differ from each other in the geometry of the test section and the force measurement system employed. The first, preliminary setup comprises a strain gauge to measure the forces generated inside a rectangular duct and is intended for verifying that LFV with a small magnet produces detectable forces. The second, final setup comprises an interference-optical force sensor with a significantly higher resolution than the strain gauge sensor. The duct employed with the final setup has a square cross section and thinner duct walls than the preliminary setup. The new setup is used to both provide an experimental basis for the two numerical projects mentioned above and to investigate how well LFV is suited for characterizing the local features of a liquid metal flow.

Sections 3.3 - 3.6 describe the different parts of the experimental setup, namely the duct itself (3.3), the two force measurement systems (3.4), the magnets that are employed with the force measurement systems (3.5), and the reference velocity sensors (3.6).

The chapter concludes with a rough estimate of the magnitude of measurement uncertainties in section 3.7.

3.1 Problem definition

The object of investigation is an electrically conducting fluid, here a liquid metal, flowing through a rectangular or square duct exposed to an inhomogeneous magnetic field. The fluid is characterized by its electrical conductivity σ, density ρ, and kinematic viscosity ν. While the magnetic field can be generated by both a permanent magnet or an electromagnet, the work here is restricted to the case of a permanent magnet. Unless stated otherwise, the permanent magnet is a cube whose edge length D is significantly smaller than the width of the duct (see fig. 3.1).

---

[1]Sections 3.1 and 3.2 have been taken from [130] with some modifications.
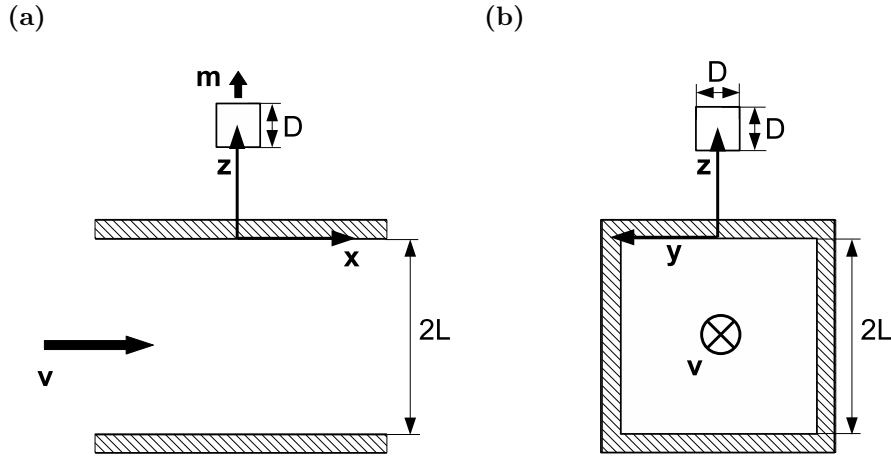
Figure 3.1: Setup of the problem. (a) Side view. (b) Rear view. – The mean velocity v of the duct flow points in the positive x-direction, the magnetization direction of the permanent magnet is along the positive z-axis. The center of the coordinate system is placed at the center of the inside of the duct wall closest to the magnet. The characteristic length scale of this setup is chosen to be the half-width L of the duct. The edge length of the magnet is denoted as D.

The geometry is described by Cartesian coordinates. The mean flow direction is named the x-direction, the direction defining the distance between the magnet and the duct is the z-direction, and y denotes the spanwise position across the duct. The origin is chosen such that $x = 0$ and $y = 0$ each lie in the middle of the duct, but $z = 0$ is on the inside of the duct wall closest to the magnet. Thus, z denotes the distance of the center of the magnet to the liquid metal. The magnetic moment $\vec{m}$ of the magnet always points in the positive z-direction, as shown in fig. 3.1. As magnets of the same size can have different magnetic moments, it is convenient to introduce the magnetization density M with $M = |\vec{m}|/D^3$. The fluid flow is driven by pressure gradients and its mean velocity v corresponds to the spatial average over the entire cross section of the duct.

3.2 Physical parameters

As explained earlier, there will be a Lorentz force F acting on the magnet, pulling it in the direction of the mean flow. The goal of this thesis is to understand how the two force components F_x and F_y depend on the various parameters of the problem, in particular on z, y, v, and D.

The bounds on these parameters are mostly given by geometrical constraints and restrictions due to the resolution of the force measurement systems. Table A.1 on page 91 gives an overview of all the parameters involved and the range they cover.

The parameters are divided into four categories. The first category comprises the material parameters of the liquid metal (GaInSn) that are fixed for both experimental setups, but also the duct half-height L (1 cm for the old setup and 2 cm for the new setup), and the wall thickness w which is fixed for each setup ($w = 8$ mm for the old setup, $w = 5$ mm for the new

setup). The material parameters include the electrical conductivity $\sigma = 3.46 \times 10^6\,\text{S/m}$, the density $\rho = 6.36 \times 10^3\,\text{kg/m}^3$, and the kinematic viscosity $\nu = 3.4 \times 10^{-7}\,\text{m}^2/\text{s}$.

The second category are the input parameters z, y, D, and v that can be adjusted independently: The magnet size ranges from $5\,\text{mm} \leq D \leq 20\,\text{mm}$, and the distance z is then bounded by the (half) magnet size and the wall thickness, $z \geq 13\,\text{mm}$ (old setup) and $z \geq 7.5\,\text{mm}$ (new setup), respectively. The velocity v is derived from the volume flux Q which is never larger than $0.29\,\text{l/s}$ (old setup) and $0.34\,\text{l/s}$ (new setup). These values roughly correspond to a maximum flow velocity of $v = 13.6\,\text{cm/s}$ for both setups. And last, the magnetic flux density maximum B_0 inside the duct depends on the magnet size D and distance z only, because all magnets have a similar magnetization density M. Accordingly, the smallest flux density ($1\,\text{mT}$) is obtained when the smallest magnet ($5\,\text{mm}$) is at the largest measured distance ($37.5\,\text{mm}$) and the largest flux density ($270\,\text{mT}$) is obtained when the biggest magnet ($15\,\text{mm}$ for the new setup) is placed immediately adjacent to the duct wall (i. e. at $z = 1.25$). However, during most measurements, the $10\,\text{mm}$ magnet has been used; this will be referred to as the standard magnet.

The third category (tab. A.1) consists of the two force components that are measured. Table A.1 presents the very maximum forces that have been measured in this project: $10\,\text{mN}$ for F_x and $0.5\,\text{mN}$ for F_y. Typical values for F_x are about $1\,\text{mN}$ or lower.

Finally, the last category summarizes the nondimensional parameters that characterize the regime of the experimental investigations presented throughout this thesis. The parameters have been defined in chapter 2. The Reynolds number (vL/ν) is a direct measure for the velocity v, because the other two parameters are constant during the experiment. Re reaches up to 4000 (old duct) and 10 000 (new duct). Similarly, the Hartmann number ($Ha = B_0 L \sqrt{\sigma/(\rho\nu)}$) is a direct measure for the strength of the magnetic field of the measurement magnet and can be up to 67 (old setup) and 270 (new setup). The interaction parameter N is on the order of 1 for most of the experiments, particularly on the old setup. For the largest magnet on the new duct ($15\,\text{mm}$) and the corresponding velocity of $9.4\,\text{cm/s}$, the interaction parameter increases to approximately 10. N is maximum, however, for the very low velocities that have been probed with the standard magnet ($v_{min} = 0.64\,\text{cm/s}$) with a value as high as 58. At this strong interaction, the velocity field is expected to be changed significantly by the magnetic field, resulting in a non-linear relationship between velocity and Lorentz force. Last, the magnetic Reynolds number ($\mu_0 \sigma v L$) is $\ll 1$ for all parameter combinations and therefore the magnetic fields of the employed permanent magnets can be considered to be unaltered during all experiments.

3.3 Liquid metal duct

The experiments are performed in a liquid metal loop as is sketched in figure 3.2. It consists of steel pipes filled with the eutectic alloy GaInSn, which is liquid at room temperature. The flow is driven by an electromagnetic pump with rotating permanent magnets, whose rotation speed determines the flow velocity [82]. Two heat exchangers keep the temperature of the fluid medium constant.
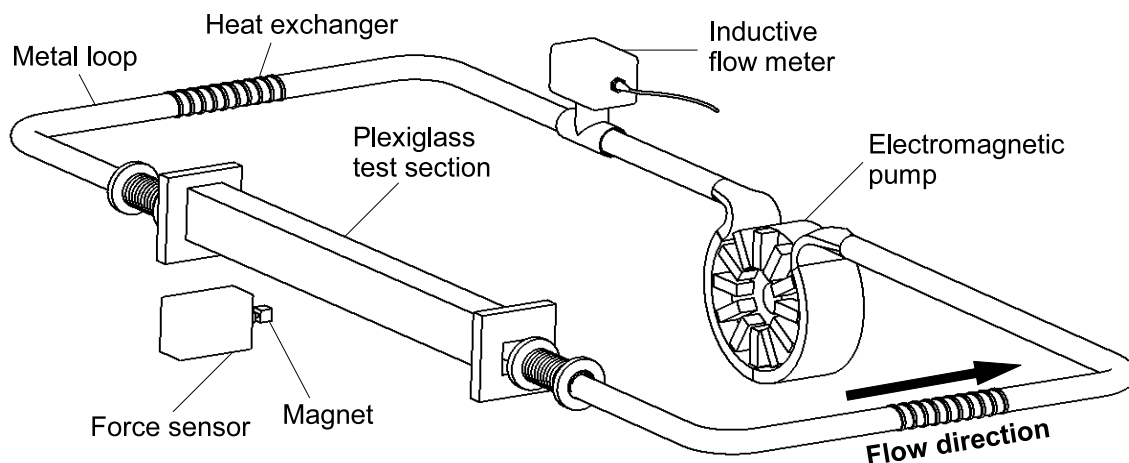
Figure 3.2: Experimental setup. The liquid metal loop consists of stainless steel pipes and a plexiglass test section. The magnet system is placed beneath (old setup) or beside the test section (new setup). Here, the distance of the magnet system to the duct has been enlarged for better visibility. Streamwise and spanwise forces are recorded one at a time. The main flow is in x-direction (from left to right inside the plexiglass in this figure), driven by the electromagnetic pump. Flow rates are recorded using a volumetric flow meter. Heat exchangers before and after the test section keep the temperature of the liquid metal constant.

3.3.1 Rectangular test section

The preliminary ("old") duct setup comprises a rectangular cross section of $108\,\mathrm{mm}$ width and $2L = 20\,\mathrm{mm}$ height on the inside and with a thickness of the bottom wall of $8\,\mathrm{mm}$. The length of the test section is approximately $90\,\mathrm{cm}$. Viewed in flow direction, the shape of the plexiglass part is that of the letter H, the two legs at the bottom adding to the stability of the duct (see fig. 3.3a). The liquid metal is covered with loose plexiglass lid sections each $22\,\mathrm{cm}$ long. This allows the duct to be mostly closed but leaves a small gap of $\approx 1\,\mathrm{cm}$ through which an additional sensor can be inserted into the flow, like a UDV probe, for example. The measurement system (section 3.4) is placed below the duct, approximately at the center of the test section, and the distance z of the magnet center to the duct is adjusted by changing the vertical position of the magnet.

3.3.2 Square test section

The final ("new") setup comprises a plexiglass test section of square inner cross section with each side being $2L = 5\,\mathrm{cm}$ long. The section has a U-shape (see fig. 3.3b), with all three walls being $5\,\mathrm{mm}$ thick. It is attached to the steel pipe with flexible bellows (shown in fig. 3.2 and marked in fig. 3.4) to decouple it from vibrations and stresses transported through the pipe that might damage the thin plexiglass walls. Since the pipe system is the same as for the old setup, the new test section is only $80\,\mathrm{cm}$ long. The liquid metal is covered with four lid sections, also leaving a gap of $1\,\mathrm{cm}$ for additional measurement probes. Unlike the old test section, the lids are tightly fixed to the duct body, thus allowing a slightly higher volume
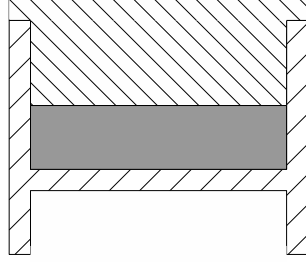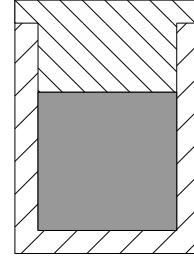
Figure 3.3: Cross sections of the two experimental setups (not to scale). The liquid metal is in the shaded areas, the plexiglass is depicted by the hatched areas. Different hatchings mark the body of the test section and the lids, respectively. (a) Preliminary test section. (b) Final test section.

flux through the test section. At the same time the cross-sectional area is larger than for the old setup up. As a result, the maximum mean velocity v in the new test section is also 13.6 cm/s, but corresponds to a Reynolds number of 10^4.

Additionally, the motor of the electromagnetic pump has been exchanged; the new motor has a computerized control that allows speed adjustments in steps of 1 rpm and runs more smoothly than the old motor. Different from the preliminary setup, the force measurement system of the new setup is placed beside the test section, as shown in figs. 3.2, 3.4, and 3.5. This allows better access to control the position of the magnet.

A complete list of changes to the setup can be found in the appendix in table B.1, and a detailed description of the construction of the new duct is provided in [131].

3.4 Force measurement systems

Throughout the duration of this project, three force measurement systems have been employed. All of them base on the deflection of a parallel spring under an applied force. The first measurement system is a 1D system that records the deflection of an aluminum spring with a strain gauge (section 3.4.1.1). This system has been applied to the preliminary duct setup. The second measurement system records the deflection of a quartz spring with an interferometer and has been applied to the new duct setup (section 3.4.2). These two measurement systems have been designed, constructed and put to test by I. Rahneberg [132, 133]. Moreover, an additional system has been built in the course of a related master's thesis [134]. It is a 2D strain gauge system and was intended for the investigation of a vertical pipe flow. Before use it needed calibration, which was performed on the new duct setup. Because it was never used to investigate the duct flow itself, it is referred to as an extra measurement system and the results it yielded occupy only a small fraction of the thesis compared to the other two measurement systems.
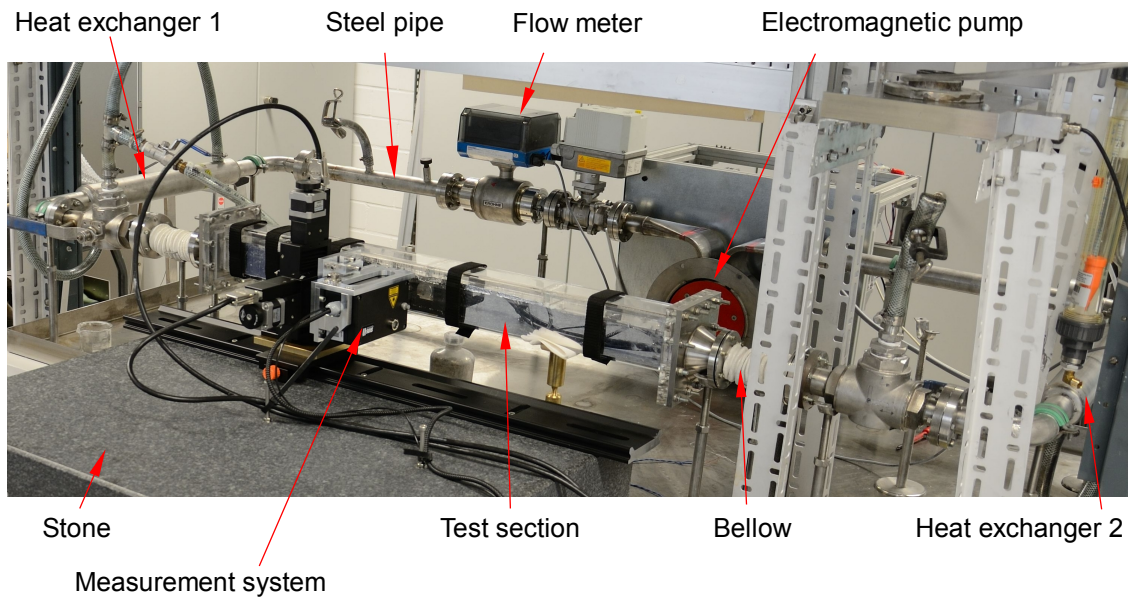
Figure 3.4: Photo of the new experimental setup. The whole metal loop comprising a steel pipe and (new) test section is placed on a table. Measurement and positioning system are mounted on the stone in front of the table, the pump stands behind the table.
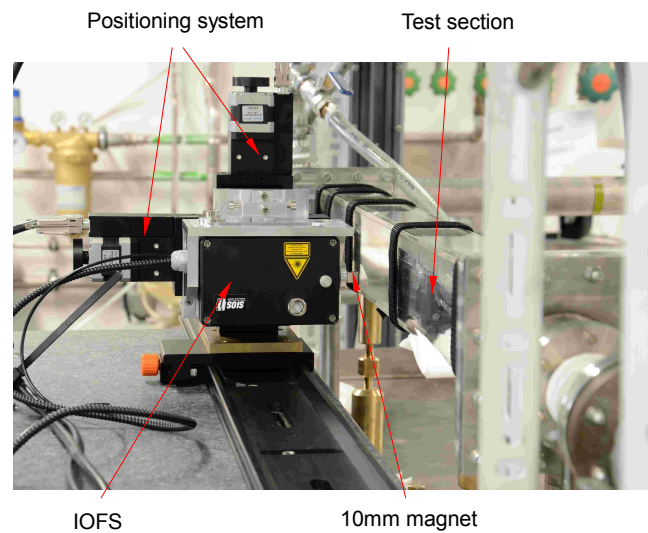

Figure 3.5: Close-up of the measurement system (interference optical force measurement system), the positioning system, the magnet, and the duct.

Magnet

Plastic extension

Deflection element
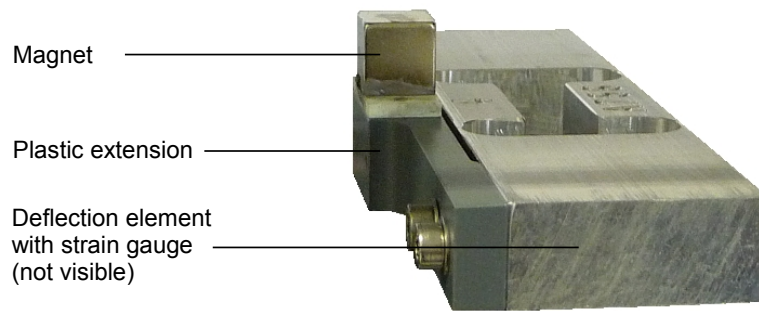with strain gauge
(not visible)

Figure 3.6: Close-up of the sensitive parts of the preliminary measurement system, the magnet and the aluminum deflection body. Edge length of the magnet is 10 mm.

3.4.1 Strain gauges

3.4.1.1 1D system

The photo in fig. 3.6 shows the aluminum parallel spring which acts as the deflection element, the permanent magnet that generates the force which is being measured, and a plastic lever that transfers the force from the magnet such that it bends the deflection element. The magnet shown is the standard magnet with the 10 mm edge length. The strain of the deflection element is measured with a strain gauge (not visible in fig. 3.6), a wire that changes its resistance when it changes its length. Several strain gauges are wired into a Wheatstone Bridge for temperature compensation, although a notable zero shift remains. The whole aluminum deflection element carries a maximum load of 1.5 N and has a resolution of 10 μN. In fig. 3.6, the sensitive direction of the parallel spring is from left to right in the plane of the paper.

The deflection element is mounted onto a standard labjack (fig. 3.7), which is used to manually adjust the height z of the magnet in the range of approximately 5 cm. The electronics visible in fig. 3.7 convert the signal of the strain gauge into a weight signal and transfer it to a PC.

The labjack is mounted on a heavy steel block, bringing the magnet closer to the duct and preventing the measurement system from being shifted by accident. The main measurement direction is parallel to the main flow (x). By turning the whole setup the y-component of the force on the magnet may be measured, as well. Thermal drifts are a major problem, and typically occur when the measurement system has been recently moved or after the electronics have just been turned on. Moreover, the system reacts sensitively to air movements (especially from the AC), temperature changes, and movements in the lab.

3.4.1.2 2D system

The 2D strain gauge system is a combination of two 1D systems (see fig. 3.8). Forces can be detected by this system in the vertical and one horizontal direction. The characteristics are similar to the 1D system, especially concerning drifts. Special care needed to be taken to reduce the dead load on the lower of the two sensors, for instance by using extra thin wires for the electronics. The maximum possible weight of the magnet is limited by the vertical
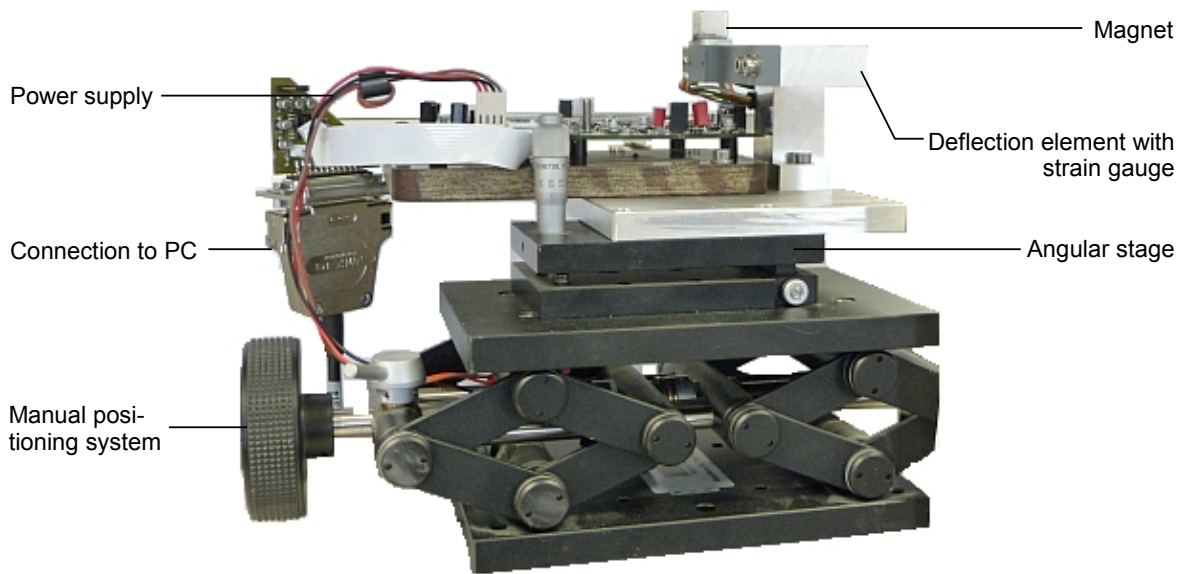
Figure 3.7: Whole 1D-strain gauge measurement system, including electronics, manual positioning system, and angular stage. Magnet size: 10 mm.

sensor that has to carry both the magnet and the horizontal sensor. Due to its intended use on a vertical pipe with thick walls, this system was mostly operated with the 2 cm magnet.

3.4.2 Interferometric sensor

In the new measurement system used on the square duct, the deflection element is made of quartz glass, which has excellent mechanical properties like a low delayed elasticity, and low thermal expansion [133, 135]. Thus, the relation between applied force and resulting deformation of the spring is highly linear. The deformation is detected to within 0.1 nm by an interferometer [135, 136] that is entirely fiber-coupled to avoid any additional heat input to the system. Due to the high sensitivity an overload protection is included in the sensor. Fig. 3.9 depicts the internal setup of the interference optical force measurement system (IOFS).

The IOFS includes an internal temperature sensor. Thus, the length values transferred by the electronics to the PC are converted to forces according to the calibration, but are also temperature-corrected. For example, the correction regards the temperature dependence of the refractive index of air and the temperature dependence of the sensitivity caused by the temperature dependence of Young's modulus [133].

In practical use, the IOFS is mounted beside the new duct, as shown in figs. 3.2, 3.4, and 3.5. When mounted as in fig. 3.5, the system measures the main force component F_x. To measure the vertical force component F_y the black box is rotated by 90 °C. Although designed for the 10 mm magnet that weighs only 7.49 g, the IOFS can also carry the weight of the 15 mm magnet (25 g).

Force measurements are performed at a sampling frequency of 8192 Hz, averaged over 128 samples and filtered (using Matlab's filter nr. 5), resulting in a time resolution of the force
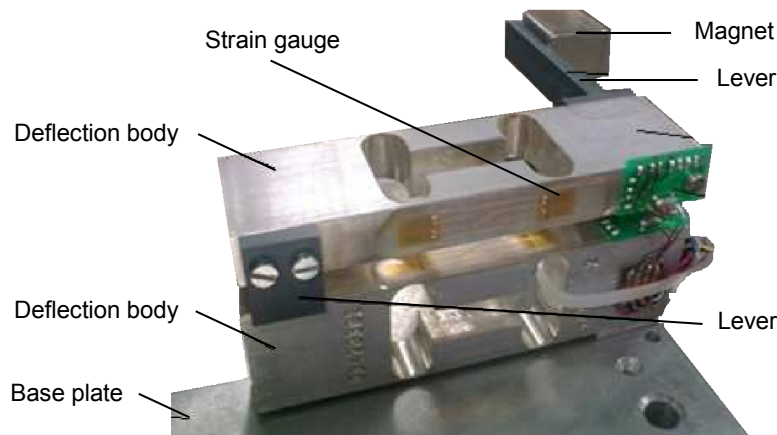
Figure 3.8: Photo of the 2D strain gauge system [134]. Two parallel springs are mounted on an aluminum base plate, the bottom spring is sensitive to vertical forces, the top spring is sensitive to horizontal forces. Wiring is kept to a minimum to reduce the dead load and offset deformation. The size of the mounted magnet is 20 mm.
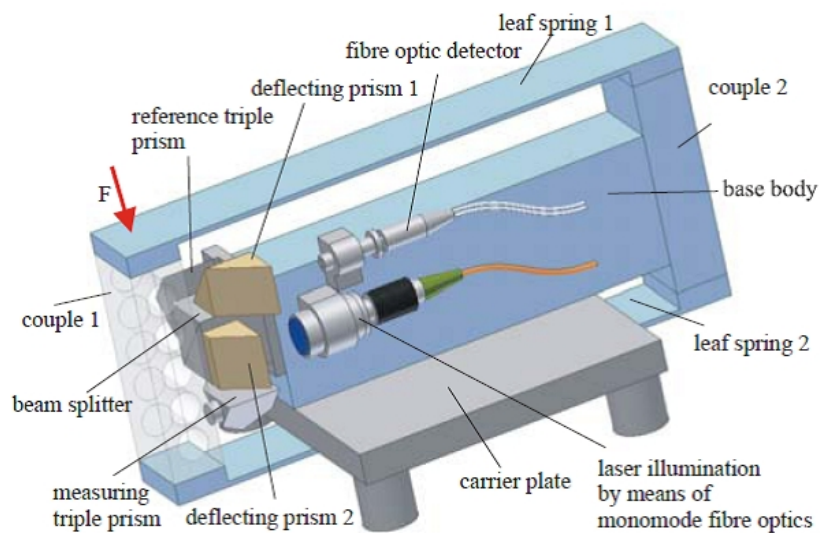

Figure 3.9: The interference optical force measurement system (IOFS). Internal setup. The magnet is attached to the left couple (grey), its magnetization pointing to the left in this figure, through an opening in the external housing (not shown). The deflection of the quartz glass parallel spring (light blue) is measured with a fiber-coupled interferometer. Courtesy of I. Rahneberg.
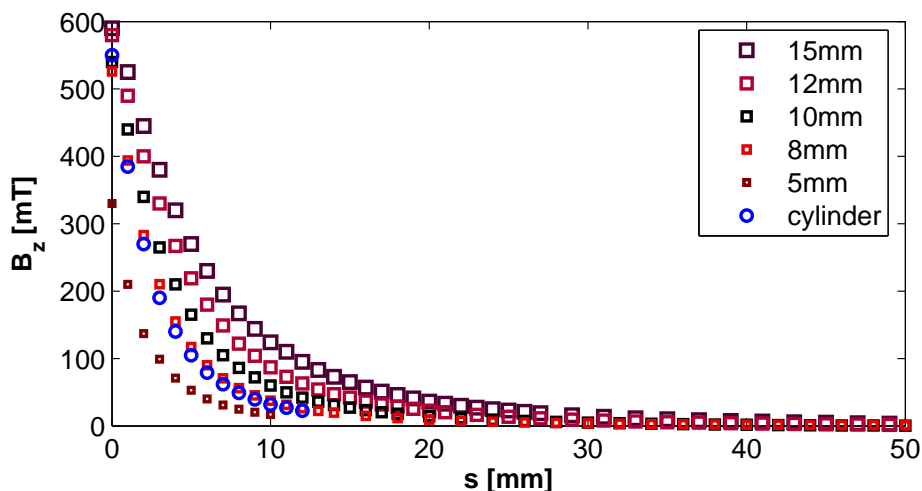
Figure 3.10: Measurements of the z-component of the B-fields along the magnetization axis of each of the six magnets employed with the IOFS. s is the distance from the magnet surface. See text for some representative values.

measurement of $6.4\,\mathrm{Hz}$. With these settings, the force resolution achieved with the IOFS is $0.015\,\mathrm{\mu N}$ [133].

The two-component positioning system was replaced in conjunction with the force measurement system. The new system allows to position the magnet with a repeatability of better than $0.05\,\mathrm{mm}$ in both y and z with two combined traversing systems. Due to the manual positioning (ruler) the repeatability in x is only about $0.5\,\mathrm{mm}$.

3.5 Magnets

Several magnets have been employed throughout the duration of the experiments, all either cubes or cylinders in shape. The $10\,\mathrm{mm}$ cube and the $15\,\mathrm{mm}$ cube have been mounted on the 1D preliminary force measurement system. The 2D strain gauge system was used with the $20\,\mathrm{mm}$ magnet cube. And the IOFS was usually mounted with the $10\,\mathrm{mm}$ cube, but was also tested with the $5\,\mathrm{mm}$, $8\,\mathrm{mm}$, $12\,\mathrm{mm}$, and $15\,\mathrm{mm}$ cubes, as well as a magnet cylinder of $10\,\mathrm{mm}$ diameter and $10\,\mathrm{mm}$ height. All magnets are NdFeB magnets, with a Curie temperature of $80°\mathrm{C}$. The grade varies for the different magnets, from N40 ($8\,\mathrm{mm}$) and N42 ($5\,\mathrm{mm}$ and $10\,\mathrm{mm}$) to N44 ($15\,\mathrm{mm}$) and N48 ($12\,\mathrm{mm}$ and cylinder).

The magnetic fields of the six magnets have been measured with a Hall probe along their magnetization axes, starting from the surface of each magnet. Fig. 3.10 shows the decay of B_z with the distance s from each magnet surface. The shape of the curves is that of an arctan [137]. Just inside the duct wall ($s = 5\,\mathrm{mm}$), the magnetic flux densities of each magnet are $270\,\mathrm{mT}$, $219\,\mathrm{mT}$, $165\,\mathrm{mT}$, $117\,\mathrm{mT}$, $53\,\mathrm{mT}$, and $105\,\mathrm{mT}$ in the order as they appear in the legend of fig. 3.10.

The magnet studied most intensively and used for most of the force measurements is the $10\,\mathrm{mm}$ magnet. It has a $475\,\mathrm{mT}$ magnetic flux density on its surface. With a positioning range of $10\,\mathrm{mm} \leq z \leq 40\,\mathrm{mm}$, the Hartmann numbers achieved with this magnet are between

(a)   **(b)**
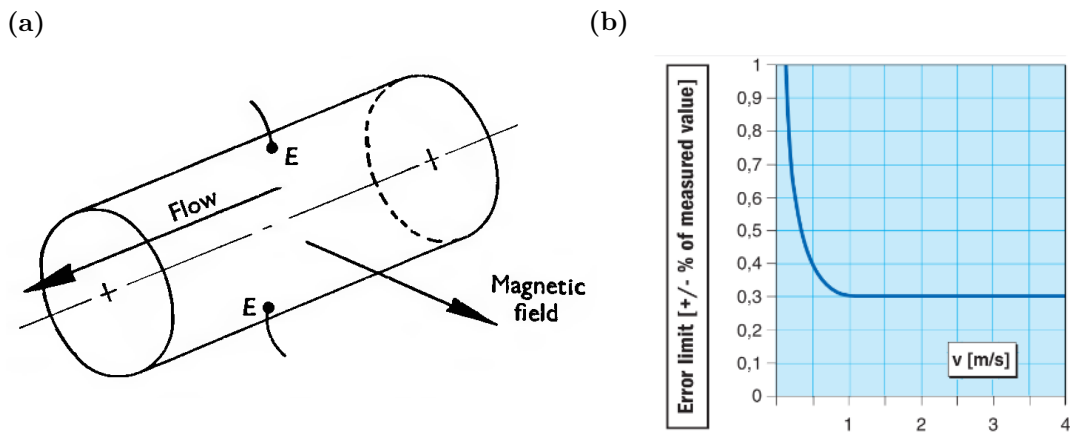

Figure 3.11: (a) Principle of a transverse inductive flow meter (from [16]). A transverse magnetic field is applied to a pipe flow and the resulting Lorentz force generates a voltage across the pipe between the electrodes E. (b) Evolution of the uncertainty of the Krohne flow meter from [75]. Uncertainties are particularly high for low flow velocities, well above 1 % for $v < 15$ cm/s.

3 and 165. The maximum Lorentz force that can be generated with this magnet is about $F_{max} = 1.6$ mN at the closest distance $z = 10$ mm and highest flow velocity $v_{max} = 13.4$ cm/s ($Re \approx 9800$). This force corresponds to roughly 1/50 of the weight of the magnet.

3.6 Reference systems

3.6.1 Inductive flow meter

Inductive flow meters have already been introduced in the previous chapter. They impose a transverse magnetic field on the fluid flow, creating an electric field perpendicular to both the flow and the magnetic field, as shown in fig. 3.11a. Shercliff [138] showed that the voltage measured on the outside of the pipe flow depends linearly on the volume flux and is independent of the velocity profile if (and only if, [139]) the velocity profile is axially symmetric.

Due to the low melting temperature of GaInSn, an inductive flow meter is incorporated in the experimental setup to provide a reference value for the volume flux. The specific instrument – a Krohne Altoflux IFS 6000 – measures flow rates up to 12 m/s [140] with an uncertainty of 0.3 % of the measured value for high velocities. However, the velocities of this experiment are below 15 cm/s, and in that range the uncertainty is 1 % and higher (see fig. 3.11b). Particularly for velocities lower than 1 cm/s the volume flux obtained from the inductive flow meter should be regarded with great care and to be an estimate at best.

3.6.2 Ultrasound Doppler Velocimeter

An Ultrasound Doppler Velocimeter (UDV) is a cylindrical transducer that emits an ultrasonic pulse. The acoustic signal is reflected off particles moving in the fluid flow and received by the transducer. In GaInSn, inhomogeneities in the metal are sufficient as reflectors such
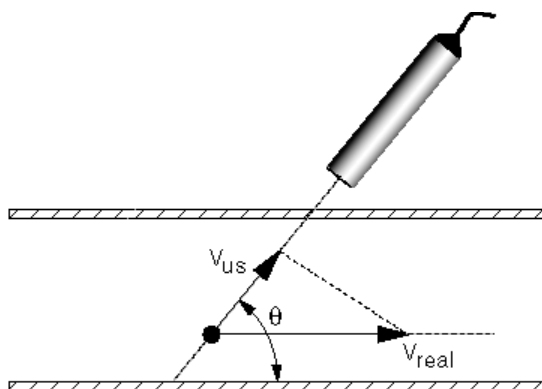
Figure 3.12: Sketch of a UDV probe that is applied at an angle to a horizontal duct. The UDV is measuring velocities parallel to the ultrasonic beam it emits, the real velocity v_{real} is a projection of the measured velocity v_{us}. This setup is infeasible for the small duct for various reasons.

that no extra seeding particles need to be added. The time delay between emitted and received reflected signal is proportional to the distance between the particle and the transducer; the difference in the time delay between two pulsed signals is used as a measure for the velocity of the particle. Since this time delay is usually very small ($< 1\,\text{us}$), not the time shift itself is taken, but the phase shift of the echo.

Typically, the UDV transducer is placed at an angle to the expected flow direction like in fig. 3.12. As the UDV records a line profile of the velocity v_{us} along the ultrasound beam, it is possible to obtain a depth profile of the (here horizontal) velocity v_{real} inside the duct if the angle θ is known.

However, there are some practical disadvantages that need to be considered when using a UDV probe in a liquid metal such as the one used here:

- Contact between sensor and liquid is absolutely critical for transmitting the ultrasound signal into the liquid (cf. [102]).
- The sensor receives echoes not only from moving particles in the fluid, but also from the duct walls. The echoes may be used for calibrating distances inside the fluid, but they also superpose the signal from the fluid velocity when the sensor is placed inappropriately.
- The transducer is insensitive to the flow immediately outside its casing.
- Any angle the sensor is placed at other than the sensor being parallel to the flow introduces further uncertainty to the velocity measurement.

To reduce problems due to the above points, the sensor is placed inside the liquid metal and parallel to the flow. As a result, the number of measurements necessary for 2D velocity profiles increases significantly, but the improvement in signal quality more than outweighs this disadvantage.

The sensor employed in taking the velocity profiles is a 4 MHz probe, about 7 cm long, which makes it easier to align with the duct, and with a 7 mm diameter at the sensor tip. Thus, any point in the profiles presented later (cf. figs. 5.21, 5.24, and 5.26) is an average over a 7 mm-diameter circle, and the nearest the probe could be placed to the wall is with the

probe center 3.5 cm away from it. In addition to the 2D profiles that are necessary for the comparison of the local velocity profile inside the duct, the UDV is used as a reference measurement system for low velocities $< 1 \, \text{cm/s}$ that are beyond the resolution of the inductive flow meter.

3.7 Uncertainties

The measurement resolutions of the two force measurement systems are $10 \, \text{mN}$ and $0.015 \, \text{µN}$, respectively. Often, the uncertainty of an averaged measurement value is determined as $u = s/\sqrt{n}$, where s is the standard deviation of the signal and n the number of data points that have been used to obtain the average [141]. In the case of the experiment of this thesis that translates into an uncertainty of less than $1 \, \%$ of the force average. However, such an uncertainty seems overly optimistic considering that the input quantities z, y, and v are significantly uncertain. Particularly in the case of the distance z the finite precision of the input parameters leads to a relatively high uncertainty of the quantity $F(z, y, v)$.

Instead of using errorbars for the presentation of the measurement results – which would be misleading, since the measurement error itself is indeed typically $u = 15 \, \%/\sqrt{300} \approx 1 \, \%$ – the uncertainty of the forces measured in this thesis is estimated separately in the remainder of this chapter. The estimate will be such that when the input parameters are set to any of the values stated throughout this thesis (to within their respective uncertainty that is), the measured force signal will be the corresponding stated force to within the now calculated uncertainty.

Exemplarily, the uncertainties are calculated for the maximum forces that are obtained with the 10 mm magnet on the preliminary duct (3.7.1) and on the new duct (3.7.2).

3.7.1 Preliminary setup

At $v = 13.6 \, \text{cm/s}$, $z = 13 \, \text{mm}$, and $y = 0$, the 1D strain gauge yields a mean force of $0.59 \, \text{mN}$ (see chapter 4).

The uncertainty in the distance Δz is estimated to be as high as 1 mm for the preliminary setup, due to the fact that the magnet is behind one of the vertical duct walls when it is brought into position (cf. fig. 3.3a). The same is true for the horizontal positioning, such that Δy is also estimated to be 1 mm. Since v is not directly measured but calculated from the volume flux Q and the cross-sectional area of the duct A, the uncertainty Δv must be determined by propagation of uncertainty [141]:

$$\Delta v = \left| \frac{d}{dQ} \left[v(Q, A) \right] \right| \Delta Q + \left| \frac{d}{dA} \left[v(Q, A) \right] \right| \Delta A = \frac{\Delta Q}{A} + \frac{Q \, \Delta A}{A^2}. \tag{3.1}$$

First, let us estimate the uncertainty in cross-sectional area. All duct walls have an uncertainty in their thickness of about $0.3 \, \text{mm}$. Additionally, the vertical duct walls are slightly leaning outward, and the lids are not firmly placed. Overall, the uncertainty of the cross-sectional area can be estimated to be about $0.5 \, \text{mm} \times 0.5 \, \text{mm}$. The manufacturer's uncertainty for the flow meter is $\Delta Q = 1 \, \% \, Q$ [75], which yields an uncertainty of the velocity

	Parameter		Uncertainty		Contribution to ΔF	
Distance z	13	mm	1	mm	186	μN
Spanwise position y	0	mm	1	mm	-	
Velocity v	13.6	cm/s	0.9	cm/s	26	μN
Force F	590	μN		±	212	μN

Table 3.1: Overview of the parameters that the measured force depends on and whose uncertainty adds to the uncertainty of the measured force. Old setup. Repeated measurements reveal that the total uncertainty ΔF is overly optimistic and should rather be 50 % of the measured mean force or even higher.

of $\Delta v = 0.9\,\text{cm/s}$ at $v \approx 13.6\,\text{cm/s}$. Table 3.1 summarizes the uncertainties of the three parameters and their respective contribution to the overall uncertainty in the mean force.

From the measurement results in chapter 4 it is known that the measured force depends on the distance roughly as $F = 11400z^{-3.82}$. The velocity v has a linear influence on the force, with a (probably underestimated) slope of 0.029. The dependence of the force on y cannot be estimated from the measurements on the preliminary duct, but from the estimates for the square duct (see next section) it can safely be assumed that the influence of Δy is much weaker than that of Δz and Δv.

Using the propagation of uncertainty analogously to eq. 3.1, the major contributions to the uncertainty of the force are 0.19 mN by the positioning uncertainty and 0.03 mN by the velocity uncertainty, yielding a total uncertainty of 0.21 mN (the difference is due to rounding error). This is about 1/3 of the measured mean value (0.59 mN), a seemingly high uncertainty. However, considering that during a measurement series with comparable parameters a force of 0.35 mN was measured (cf. section 4.2.1.4), this uncertainty is still rather too optimistic. Clearly, the reproducibility between different measurement campaigns is to within 50 % at best. On the other hand, the repeatability within one campaign is probably much better than to within 1/3, because the *relative* positioning is better than $\Delta z = 1\,\text{mm}$, between 0.3 mm for small distances and 0.5 mm for large distances.

[2]Additionally, there is the possibility that the measured forces are affected by changes in the magnetic field. However, changes in magnetic flux density due to temperature fluctuations are estimated to be of the order of 0.2 %. This estimate is calculated from the manufacturers data by measuring the average temperature fluctuation in a given day (which is approximately 4 K) in the laboratory where the experiments are performed. This temperature induced error is in the order of the stray field strength in the laboratory. Further random error sources are the air flow caused by the air conditioning system and mechanical vibrations inside the laboratory, but these are harder to quantify and do not affect the mean of the forces which has been used here.

---

[2]This paragraph is taken from [79]

	Parameter		Uncertainty		Contribution to ΔF	
Distance z	10	mm	0.3	mm	135	µN
Spanwise position y	0	mm	0.5	mm	0.1	µN
Velocity v	13.6	cm/s	0.9	cm/s	36	µN
Force F	900	µN	$\pm$		171	µN

Table 3.2: Same as tab. 3.1, but for the new setup. The overall force uncertainty is consistent with the reproducibility of the force measurement values. Within one measurement campaign the uncertainty is significantly lower, i.e. the repeatability is better.

3.7.2 Final force measurement setup

The general procedure for finding the measurement uncertainty of the new setup is similar to the one for the old setup. Spanwise position y and velocity v are the same as for the old setup, but the distance z here is 10 mm. A realistic uncertainty for the latter value is $\Delta z = 0.3$ mm, and $\Delta y = 0.5$ mm for the vertical placement. The uncertainty in velocity is determined as above; due to the only slightly different cross section Δv also amounts to 0.9 cm/s. For the new setup, the force is found to depend on z, y, v as follows (see section 5.2):

$$F = 7489 \, z_{[mm]}^{-3.80},$$
$$F = -1.409 \times 10^{-3} \, y_{[mm]}^2 + 0.256 \times 10^{-3} \, y_{[mm]} + 0.966, \text{ and}$$
$$F = 0.125 \, v_{[cm/s]} - 0.055.$$

Here, propagation of uncertainty yields the contributions $\Delta F_z = 0.135$ mN, $\Delta F_y = 0.1$ µN, and $\Delta F_v = 0.036$ mN and a total uncertainty of $\Delta F = 0.17$ mN (tab. 3.2). On the other hand, at different measurement campaigns the measured forces varied as much as 0.90 mN, 1.00 mN, and 1.05 mN although the parameters are the same as stated above.

Three things should be pointed out here: Although almost 20 % is still a high uncertainty, it seems to be rather realistic as it covers the whole range of forces that are obtained for the particular set of parameters ($z = 10$ mm, $y = 0$, $v = 13.6$ cm/s). Second, the high uncertainty is mostly due to the uncertainty in positioning and the large gradient of the force. For example, at a distance of an additional centimeter, i.e. at $z = 20$ mm, $\Delta F_z = 0.005$ mN and the resulting uncertainty in force is $\Delta F = 0.041$ mN. Since the force itself is decreased to 0.096 mN at that distance, the relative uncertainty is as high as 43 %. And last, but not least, within one measurement campaign the force is *repeatable* to within 4.3 % (a minimum of 0.864 mN and a maximum of 0.901 mN from 6 independent values of one campaign with the above parameters). This low value may be attributed mostly to the improved positioning system.

4 Results from the Preliminary Setup and Discussion

This chapter presents the results obtained with the preliminary force measurement setup. The results not only give a first impression on the magnitude of the Lorentz forces that can be generated in a laboratory experiment with a small magnet, but they are also used to find flaws in the setup and sources of errors that can be avoided.

In section 4.1, a rough estimate is presented for the forces that can be expected to be obtained with the strain gauge setup. Forces are predicted for both strain gauge systems. As explained in chapter 3, the 1D-strain gauge system has been used on the old duct ($10.8\,\text{cm} \times 2\,\text{cm}$ cross section, $8\,\text{mm}$ wall thickness), and the 2D-strain gauge system was set up on the new duct ($5\,\text{cm} \times 5\,\text{cm}$ cross section, $5\,\text{mm}$ wall thickness). Moreover, the 1D-system employs a $10\,\text{mm}$ and a $15\,\text{mm}$ magnet cube, whereas the 2D-system uses a $20\,\text{mm}$ cube for generating the Lorentz force. And last, the flow velocities deviate from each other by $1\,\text{cm}$, being $11.4\,\text{cm/s}$ for the 1D-system and $12.4\,\text{cm/s}$ for the 2D-system. These differences should be kept in mind when the data sets from the two setups are compared.

The measurement results for the 1D-system are summarized in section 4.2. It should be noted here that all measurements presented in this chapter have a high uncertainty of up to 50%, which is not depicted explicitly in the graphs. Section 4.3 comprises a selection of the measurements performed with the 2D-system. While the 1D-system was a test system to find what needed to be improved for the new setup, the inclusion of the results from the 2D-system is intended to show that the force measurement technique can in principle be extended to more-component measurement systems.

Two data sets of section 4.2 are being published in [79], namely the distance dependence and the velocity dependence of the Lorentz force for the $10\,\text{mm}$ magnet. In [79], the data obtained with the 1D strain gauge is used as a basis of validation for the numerical simulations of G. Pulugundla's project. Curiously, the kinematic simulations are found to be closer to the experiment than their dynamic counterparts, but this effect may safely be assumed to be due to the high measurement uncertainty.

4.1 Expected forces

The forces on the small magnet in the vicinity of the metal flow can be predicted according to the theoretical analysis in [17]. There, the authors assume a fluid layer of thickness d and of electrical conductivity σ. A magnetic dipole is placed beside the fluid at some distance z. The fluid moves at uniform velocity, and the velocity field is not affected by the magnetic field (kinematic approximation). The authors themselves extend their theory to cubic magnets by substituting the magnetic moment m of the magnet by the product of the magnetization

		D [cm]							
		1.0			1.5			2.0*	
		T	E	R	T	E	R	T	E	R
z [cm]	1.30	662	581	1.1						
	1.55	381	300	1.3	4344	2309	1.9			
	1.80	237	214	1.1	2704	1601	1.7	16524	9146	1.8
	2.00	169	115	1.5	1930	1162	1.7	11794	7218	1.6

Table 4.1: Drag forces in µN for the three employed magnets at various distances. T ... theoretical prediction; E ... experimental value; R ... ratio of T and E. The theoretical prediction always over-estimates the forces, with increasing error for the larger magnets. Average flow velocities are 11.4 cm/s except for the largest magnet (∗), where $v = 12.4$ cm/s.

density M and the magnet volume V. The resulting analytical formula for estimating the force on the magnet then is [17]:

$$\vec{F} = \frac{1}{128\pi} \frac{\mu_0^2 (MD^3)^2 \sigma v}{z^3} \left(1 - \frac{1}{(1 + d/z)^3} \right) \vec{e_x}$$ (4.1)

with the parameters:

magnet size	D	=	$1\,\text{cm}, 1.5\,\text{cm}, 2\,\text{cm}$
magnet distance	z	=	$1.3\,\text{cm} \ldots 2\,\text{cm}$
magnetization density	M	=	$1 \times 10^6\,\text{A/m}$
electrical conductivity	σ	=	$3.46 \times 10^6\,1/\Omega\text{m}$
flow velocity	v	=	$11.4\,\text{cm/s}, 12.4\,\text{cm/s}$
fluid density	ρ	=	$6360\,\text{kg/m}^3$
magnetic permeability	μ_0	=	$4\pi \times 10^{-7}\,\text{N/A}^2$.

Table 4.1 summarizes the forces for the three magnet sizes and four selected distances between magnet center and duct that have also been probed experimentally. The theoretical predictions are found in the columns marked with 'T'. The experimentally measured values are marked with 'E' and the ratio between the two is marked with 'R'. While the first two magnet columns were obtained at average flow velocities of 11.4 cm/s, the column marked with the asterisk (∗) are obtained for a slightly higher velocity and therefore the three magnet size columns should not be compared with each other directly. However, looking at the ratio of the predicted and the measured forces, one can see that the estimate works reasonably well for the smallest magnet but predicts forces that are too large by almost a factor of 2 for the two larger magnets whose fields deviate significantly from that of a point dipole.

4.2 1D strain gauge

The 1D-force measurement system has been employed with the rectangular duct setup that has a $10.8\,\text{cm} \times 2\,\text{cm}$ cross section and $8\,\text{mm}$ thick walls. The measurement system is placed
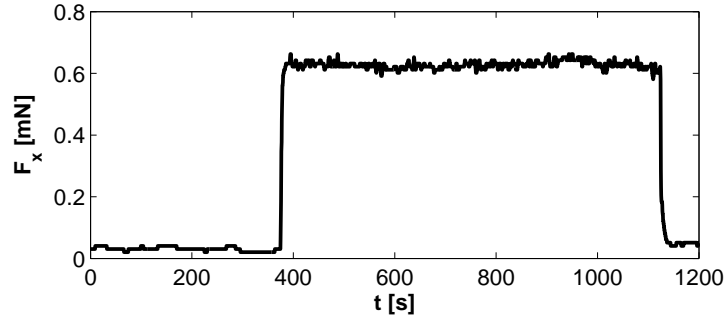
Figure 4.1: Sample time series of the streamwise Lorentz force component. Velocity is increased from 0 to 13 cm/s at $t = 360$ s and decreased to 0 at $t = 1100$ s. Force offset between the two measurements at $v = 0$ is due to parasitic effects of the force measurement system (see text for details).

below the duct and generally measures in the horizontal direction, either parallel or perpendicular to the main flow direction.

4.2.1 Streamwise force F_x

4.2.1.1 On/off measurement

Maximum forces are achieved when the magnet is placed immediately below the bottom of the duct, almost touching the bottom wall. Then the distance between the liquid metal and the center of the magnet is 13 mm for the small 10 mm magnet cube and 15.5 mm for the 15 mm magnet cube, respectively. The flow velocities for the two magnets are set to 13.0 cm/s and 12.3 cm/s, producing streamwise forces of 0.65 mN (small magnet) and 2.35 mN (15 mm cube). Note that the force produced by the larger magnet is higher by about the same factor as the magnet volume is higher (a factor of 3.6 as compared to a factor of 3.4).

It is worthwhile to take a closer look at how the force values are obtained. Fig. 4.1 shows the converted output of the force sensor over time for the 10 mm magnet. First, the pump is turned off and the fluid is at rest. At $t = 360$ s the pump is being turned on and the fluid moves at 13 cm/s until $t = 1100$ s, when the pump is turned off again. The force signal reacts quickly when the pump speed is changed, reaching the new level within 12 s both at the beginning and at the end of the plateau. Values are recorded at a rate of approximately 5 Hz.

Seemingly simple, this very basic measurement reveals a major issue encountered when measuring forces with strain gauges: The neutral signal of the measurement device (i. e. at zero flow velocity) varies before and after the plateau. In fig. 4.1 the difference amounts to a reading of 0.031 mN at the left zero signal and 0.051 mN at the right zero signal. This offset is not reproducible in its magnitude and seems to be due to thermal drift of the measurement system. The offset is negligible only for the shorter measurements and at relatively high forces. Moreover, since the neutral signal is not zero, every measurement of the force when the fluid is flowing must be accompanied by a force measurement during which the fluid is at rest, with the difference between the two being equivalent to the absolute force acting on the magnet during the fluid flow.
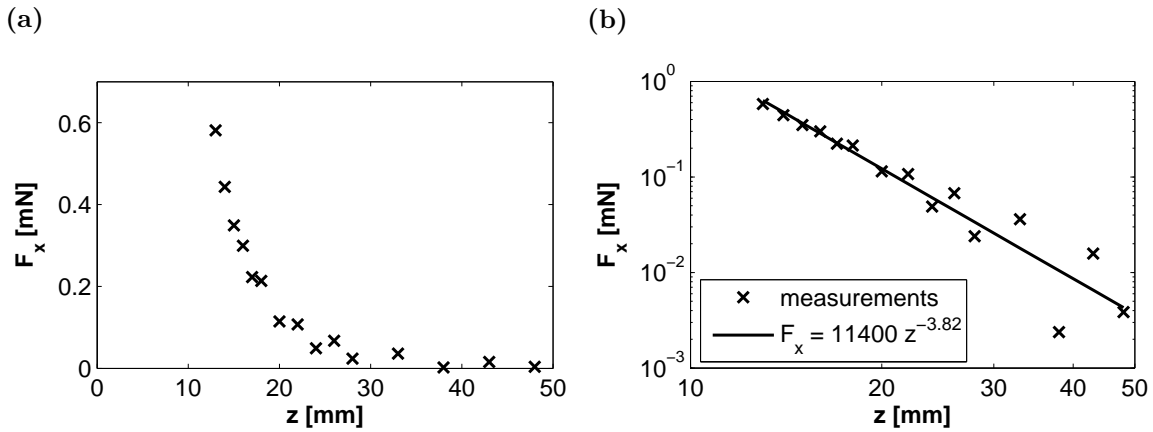
(a)

(b)

Figure 4.2: Distance dependence of the streamwise Lorentz force component, every data point is an average over 300 s. Distance z is measured from the center of the magnet to the inside of the bottom wall which is 8 mm thick. Therefore, at the smallest distance $z = 13$ mm the magnet almost touches the duct wall. Average flow velocity is $v \approx 11.4$ cm/s. (a) Linear F_x-z-diagram. (b) Log-log diagram of the same data illustrating the exponent of decay of -3.8. Forces above the straight line correspond to an on-off step measurement, and forces below the line are recorded when the motor was first off and then turned on.

4.2.1.2 Distance dependence $F_x(z)$

The dependence of the streamwise force component on the distance of the magnet to the liquid metal is found by varying the vertical position of the magnet. The distance is smallest with the magnet surface (almost) touching the bottom wall, and is then increased in steps of 1 mm (13 mm $\leq z \leq 18$ mm), 2 mm (18 mm $\leq z \leq 28$ mm) and 5 mm (28 mm $\leq z \leq 43$ mm). Force values are obtained by averaging over 300 s at $v = 11.4$ cm/s for each distance z.

Fig. 4.2 shows the resulting force behavior for the 10 mm magnet, with a linear plot in fig. 4.2a and the same data in a log-log plot in fig. 4.2b. As expected, the force is decreasing with increasing distance of the magnet to the duct. The best fit is found to be the power-law $F \sim z^{3.8}$. Remember, however, that the uncertainty of each data point is approximately 50% of the respective absolute value.

An attentive observer may see that the measurement splits into two distinct curves for larger distances. This coincides with the following pattern: The lower forces are recorded when (a) the fluid was first at rest and then the pump was turned on, and the higher forces correspond to when the fluid was originally moving and the pump then turned off. No physical explanation could be found for this behavior, especially since it is not observed with the new duct setup. Throughout the remainder of the strain gauge measurements the latter procedure (on-off) is followed, avoiding to have to adjust the velocity with the delicate motor dial during a running measurement.

The F-z-dependence is re-measured with the 15 mm magnet following the above improved procedure and no bifurcation is found (fig. 4.3). Here, the decline in force is determined to be $\sim z^{-3.4}$, i.e. slightly more gradual than for the 10 mm magnet.
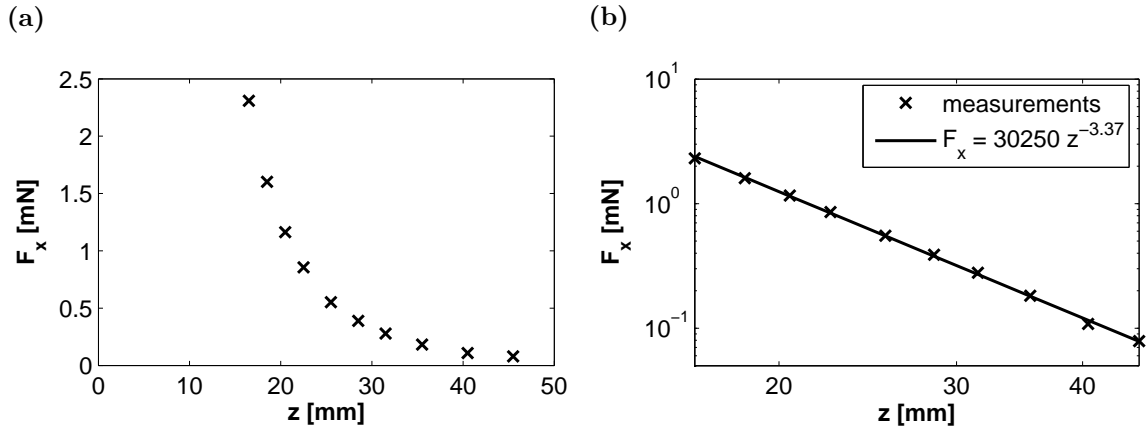
(a)   **(b)**

Figure 4.3: Same as fig. 4.2, but with the 15 mm magnet cube. Force values are obtained at each position by averaging over 300 s at $v = 11.4$ cm/s and subtracting the average over 300 s at $v = 0$. The decrease in force is slower for increasing distances than in fig. 4.2, therefore the slope of the log-log plot is less steep (-3.4) than for the 10 mm magnet (-3.8).
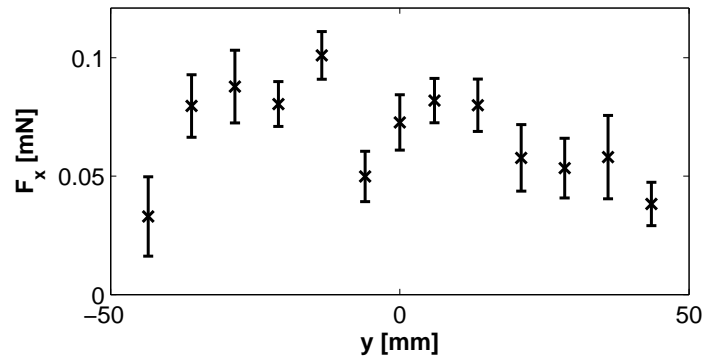

Figure 4.4: Dependence of the streamwise force component on the spanwise position of the magnet, measured with the 10 mm magnet. Flow velocity is 11.1 cm/s. Error bars represent the standard deviation of the raw time signal. The distance of the magnet to the duct is as large as 23 mm because of geometrical restrictions.

4.2.1.3 Spanwise position dependence $F_x(y)$

Determining the spanwise position dependence is hindered by the H-shape of the plexiglass test section which prevents the magnet from being placed close to the bottom wall at the sides of the duct (cf. fig. 3.3a). Thus, the deflection element has to be placed below the two legs of the H and the distance of the magnet center to the liquid metal is therefore $z = 23$ mm. Positioning in y-direction is achieved by sliding the whole block on which the measurement system is mounted into the desired position.

In addition to this crude means of positioning, the test section is found to be inclined, affecting the vertical distance z at each placement in y. Since the area below the duct is hard to access with a ruler or tape, the total uncertainty of the positioning is estimated to be at least 1 mm in both y- and z-direction.
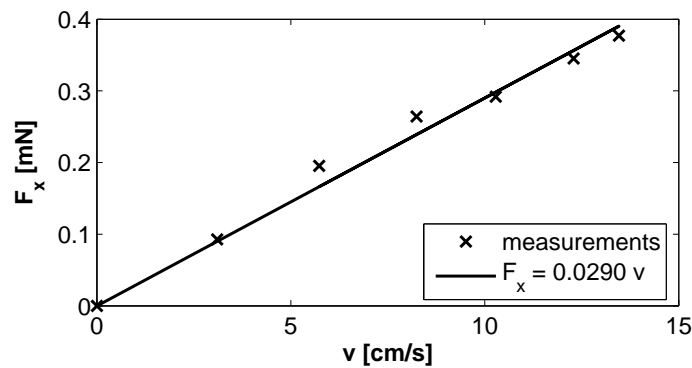
Figure 4.5: The dependence of the streamwise Lorentz force on the mean flow velocity of the liquid metal. Measured with the 10 mm magnet at $z = 13$ mm and $y = 0$.

Fig. 4.4 shows the result of this rather crude measurement series. Each data point represents 900 s of measurement: 300 s for setting the flow velocity and adjusting the position of the measurement system, 300 s for measuring at the maximum flow velocity, and the final 300 s for recording the neutral signal. From the latter two 300 s blocks the first 100 s are discarded to ensure the flow is steady or completely at rest, respectively.

Note that the errorbars in fig. 4.4 do not depict the uncertainty of the measurement (which is 50%), but only the standard deviation. The random signal fluctuations are high compared to the magnitude of the signal. As a result, there is no clear dependence of the Lorentz force on the spanwise position besides the marginal trend to be smaller at the corners of the flow than at its center.

4.2.1.4 Velocity dependence $F_x(v)$

For the velocity dependence the 10 mm magnet is placed back at $y = 0$ and $z = 13$ mm. The flow velocity is varied from 0 to 13.5 cm/s (see fig. 4.5), which is the very maximum the duct can sustain. For comparison, a velocity of 13.5 cm/s in the old setup corresponds to a maximum Reynolds number of about 4000. In that range, the Lorentz force depends linearly on the flow rate – a fit as good as a fit can be with measurement uncertainties ranging around 50% of each measurement value and only six non-zero data points.

One outlier at $v \approx 0$ has been omitted from fig. 4.5. Although the liquid metal was not moving, the flow meter gave a non-zero reading. More to the point, the electromagnetic reference flow meter does not produce any reliable values at velocities around or lower than 1 cm/s.

Another problem becomes apparent when comparing fig. 4.5 closely to fig. 4.2: While fig. 4.2 states a force of 0.59 mN for the closest magnet-duct position and a flow rate of 11.4 cm/s, fig. 4.5 implies a force of 0.35 mN for the same distance but a slightly higher flow rate of 12.2 cm/s. The most plausible explanation for this discrepancy is that the magnet is not placed at the exact same distance in both measurement series, despite all efforts.

The data of fig. 4.5 is being published in [79] along with the distance dependence in fig. 4.2. Although the uncertainties in force measurement range from 20% to 30%, the comparison
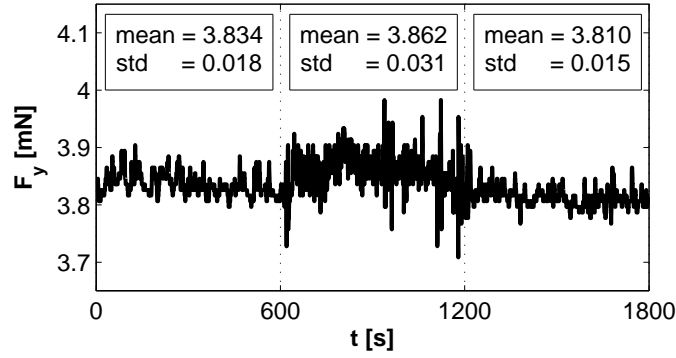
Figure 4.6: Time series for the spanwise force component recorded with the 15 mm magnet. The flow velocity is zero for $t < 600$ s and $t > 1200$ s and 12.8 cm/s in the interval 600 s $< t < 1200$ s. The change in force signal implies a force on the magnet of at least 28 μN when the flow velocity is $v > 0$. The resolution of the measurement system is 10 μN.

of the two measurement series reveals that the reproducibility of the force measurement is much poorer and the estimate found in chapter 3 is likely to be more realistic.

These pessimistic results notwithstanding it should be kept in mind that they have been obtained with a preliminary setup that was mostly intended to test the reliability of the theoretical prediction and to improve the overall duct setup. Despite the high uncertainty to them, the findings provide a valuable indication that the theory in [17] predicts the forces on small magnets reasonably well – a trait that was questioned for the large-magnet setup by C. Weidermann [142].

4.2.2 Spanwise force F_y

Although being a 1D system, the measurement system can record the spanwise force component when rotated by 90°. However, no signal could be detected using the 10 mm magnet. Only the 15 mm magnet produced – however weak – a signal. Fig. 4.6 shows the time series of the spanwise force that has been obtained like in section 4.2.1.1: During the first ten minutes of the half-hour measurement the liquid metal is at rest. At $t = 600$ s, the motor is turned on and the velocity set to 12.8 cm/s for 10 min. For the final 10 min, the motor is turned off again. As before, the absolute value of the force is of no importance, but only the difference between zero and maximum signal.

Comparison of the zero signals before and after the flow intervals reconfirms the poor repeatability of the neutral signal. But even with the more pessimistic neutral value of the final 10 min, the increase in the Lorentz force amounts to 28 μN when the motor is turned on. However, this is only three times larger than the nominal resolution of the scale of 10 μN. While this signal is very weak, it is (a) in the range of the predicted values for this setup and (b) promises to be clearly detectable by the new, optical measurement system.

4.3 2D strain gauge

The extension of the strain gauge system to a 2D system is quite straight-forward: Two independent 1D sensors are joined together, one sensitive in the horizontal direction, as before, and the other sensor sensitive in the vertical direction (cf. section 3.4.1.2).

For the horizontal force sensor, calibrations can be performed on the new duct setup with the $5\,cm \times 5\,cm$ cross sectional test section (section 3.3.2). Calibration of the vertical sensor must be performed on a vertically oriented duct, which is not part of this thesis. Nevertheless, measurements are performed with both sensors simultaneously for several velocities and at three different distances by M. Münster in the frame of his master's thesis. The results are shown in fig. 4.7 for both measured force components, F_x and F_y.

Clearly, the horizontal force depends linearly on the average velocity (fig. 4.7a), whereas the vertical force does not show a clear dependence on the velocity and is barely above the resolution threshold (fig. 4.7b) – which is not surprising considering the horizontal nature of the setup. Nevertheless, the calibration experiment proves the general feasibility of extending the strain gauge system to a 2D force measurement system without losing the high precision the single sensors.

After calibration, the 2D strain gauge setup was used at a vertical pipe flow to investigate if the latter has a horizontal component or not, i.e. if the fluid is moving in a swirling manner inside the pipe or principally straight. There, the fluid is moving inside a pipe with 16 mm thick walls, but has an electrical conductivity and flow velocities similar to the Ilmenau duct. Because of the high melting temperature of the flow medium (MCP137) of $137\,°C$, an additional 4 mm air gap needs to be allowed between the magnet and the pipe. To reliably detect the fluid velocity at this distance, the strain gauge system is equipped with a 20 mm magnet cube, corresponding to a minimum distance of $z = 30\,mm$. This distance has been covered in the calibration experiments (fig. 4.7a). Unfortunately, measurements at the vertical pipe had to be abandoned due to a leakage before the measurement system could be put to operation.

4.4 Conclusions

The preliminary force measurement setup comprising a 1D strain gauge was successfully used to perform force measurements on the liquid metal duct with the old test section. Despite the rudimentary positioning system, the streamwise Lorentz force component is found to depend on the distance of the magnet to the duct ($\sim z^{-3.8}$ for the 10 mm magnet) and on the average flow velocity (roughly linearly). A tendency is recognizable for the force to decline towards the edges of the duct. It is possible to detect a slight change in the spanwise force signal with the 15 mm magnet.

The preliminary measurement setup was helpful in designing the new test section. Among the realized improvements (see table B.1) are a more precise positioning system, a thinner duct wall, a new pump, and the addition of a UDV reference measurement system, particularly for low flow velocities. Especially helpful was the affirmation that the theoretically
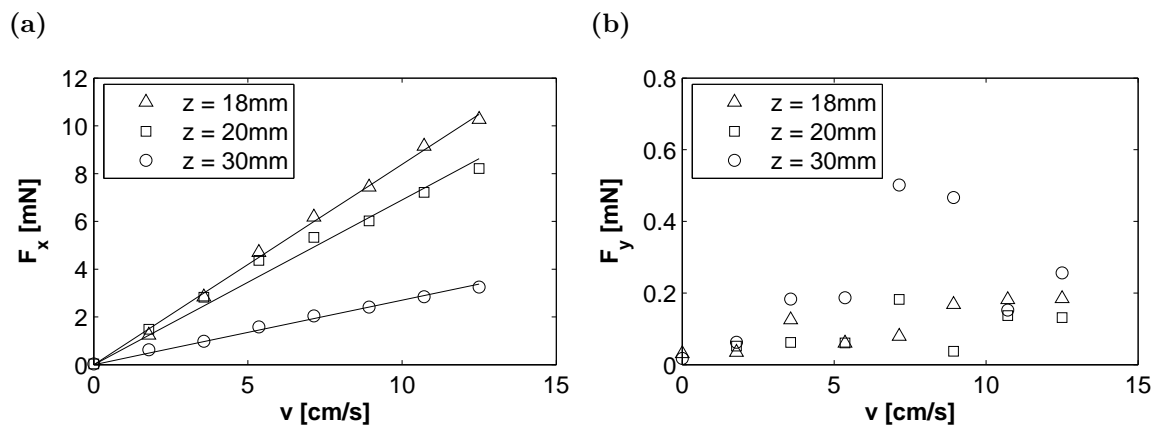
(a)

(b)

Figure 4.7: Velocity dependence of the two force components at three different distances of the 20 mm magnet to the duct. Measurements are performed on the Ilmenau duct, where the main flow direction is horizontal. The measurement system is placed beside the test section on the lab table. (a) Streamwise (horizontal) force component. (b) Spanwise (vertical) force component. Both components are measured simultaneously. Data recorded by M. Münster.

predicted forces are reasonably close to the eventually measured values and could therefore be used for designing and dimensioning the optical force measurement system.

The 2D measurement setup proved the general feasibility of extending the 1D strain gauge system to a 2D system of good resolution and suitable for the use as a velocimeter.

5 Results from the Final Setup and Discussion

This chapter is the core of the entire thesis. It presents the full experimental results obtained with the new, square-duct setup. Among other improvements, the resolution of the force measurement system has been improved and the magnitude of the force itself has been increased compared to the previous setup. The details of the improvements have been discussed in chapter 3 and are summarized in table B.1.

The first section of this chapter (5.1) characterizes the physical behavior of the experimental setup. Questions addressed include a prediction of the force that can be obtained, the drift of the force signal with changes in the ambient temperature, the influence of vibrations on the force signal, and the repeatability of the force signal. Further details can be found in [133], especially regarding calibration procedures and the design of hardware, electronics, and software.

Section 5.2 presents how the force depends on the four input parameters velocity v, distance z, vertical spanwise position y, and magnet size D for the unperturbed duct flow. Specifically, the streamwise force component $F_x(v, z, y, D)$ and the spanwise force component $F_y(v, z, y)$ are presented. The measurement results form the basis for validation of numerical codes and provide the reference for the results that follow. Two measurement series (namely $F_x(z)$ and $F_x(v)$) have been published [130].

In section 5.3 a number of modifications to the duct setup are introduced that change the flow profile significantly. The resulting deviations of the force profile from the standard profiles in section 5.2 demonstrate the spatial resolution of the LFF that has been claimed in a number of publications [79, 130] and in the introduction to this thesis. The main result of section 5.3 is being published [143].

Section 5.4 discusses the temporal resolution of the results achieved in section 5.3. Turbulent fluctuations in the flow are within the scope of the local LFF.

The chapter concludes in section 5.5 with a summary of the results obtained with the new duct setup.

5.1 Characterization of the measurement system

5.1.1 Expected forces

The estimation of the forces follows the analysis sketched in section 4.1, but with the changed parameters:

$$v = 0.1 \, \text{m/s},$$
$$D = 5 \, \text{mm} \dots 15 \, \text{mm}, \text{ and}$$
$$z = 7.5 \, \text{mm} \dots 12.5 \, \text{mm}.$$

		D [cm]				
		0.5	0.8	1.0	1.2	1.5
	0.75	48				
	0.90	28	463			
z [cm]	1.00	20	337	1285		
	1.10	15	253	964	2879	
	1.25	10	172	656	1958	7468

Table 5.1: Drag forces in µN expected from eq. 4.1 for all magnets that have been used with the new setup. The diagonal corresponds to the closest distance for each magnet. Each row represents the forces for a fixed distance between magnet center and liquid metal.

The range of the magnets used has been extended from the earlier $D = 10\,\text{mm}$ magnet to the 5, 8, 10, 12, and 15 mm magnets. Since the force measurement system was designed for the 10 mm magnet, the 20 mm magnet from section 4.3 could not be employed; the 15 mm magnet is the heaviest that the measurement system can carry. The absolute distance z of the magnet center to the inside of the duct wall is smaller than in section 4.1, because the wall thickness is reduced to 5 mm in the new setup.

With the use of eq. 4.1, the expected forces for each magnet have been calculated. Table 5.1 shows both the maximum forces that can be achieved with each magnet (along the diagonal) and the forces for a fixed position of the magnet center (rows). One can see that although the largest magnet (15 mm) has a volume 27 times as large as that of the smallest magnet (5 mm), the maximum obtainable force at $z = 12.5\,\text{mm}$ is more than 700 (27^2) times higher for that magnet. That is because the magnet size enters eq. 4.1 via the square of the magnetization: $m^2 = M^2 D^6$. However, the estimate via eq. 4.1 becomes increasingly inaccurate for larger magnets, as the experiments in section 5.2 (tab. 5.2) will show.

For the standard 1 cm magnet the estimate predicts a force of 1.3 mN at the closest distance and for $v = 10\,\text{cm/s}$. This is stronger than for the preliminary setup by a factor of 2 – the sole reason for this increase is the reduced wall thickness.

5.1.2 Long-term measurement

Figures 5.1a and b shows a long-term measurement over nearly a week. The measurement was started on late Friday afternoon, when the air-conditioning was turned off and most colleagues had left work. Temperatures were recorded both inside the casing of the measurement system and outside but in close vicinity to the casing. Both temperatures display a 24 h variation, which the force signal follows during the first 60 hours of signal recording, until early Monday morning. During the second half of the measurement the temperature drift of the force signal is masked by strong fluctuations, presumably due to air currents caused by the air-conditioning and people entering and passing through the laboratory.

Although the first 60 hours of the long-term measurement seem to show a temperature-dependent force variation, the force drift can unfortunately not be predicted from the temperature, even without the fluctuations. In fig. 5.1c the force is plotted as a function of the
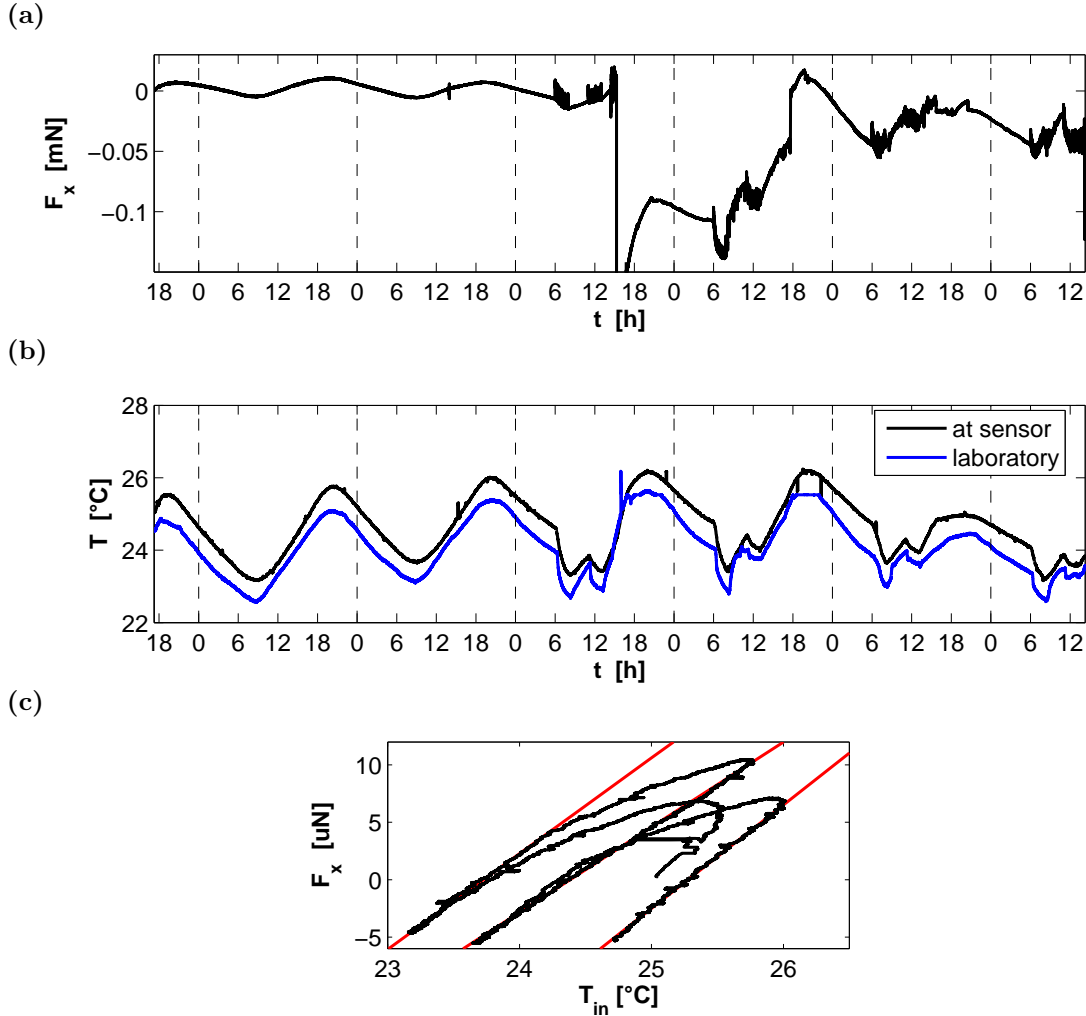
Figure 5.1: A 150-hour long-term measurement starting Friday afternoon and ending Thursday at noon. (a) Raw force signal. The onset of fluctuations in the force signal coincides with the start of work inside the lab building (Monday, 6 am). In the following days air currents cause strong fluctuations in the force signal that hide the periodic temperature-induced drift. (b) Temperature inside the casing of the measurement system (black line) and laboratory temperature (blue). (c) Force signal versus temperature inside the casing during the first 60 hours of the measurement, when fluctuations are minimal. Even then, the force is not uniquely related to the temperature. However, the force signal does change linearly with temperature for periods of a few hours each. During these periods, the force signal changes with 8.26 μN/K on average (red lines).

temperature. Not only is the function not unique, but the times when the force increases linearly with temperature have different slopes, making a temperature correction of the force signal for times of non-linear drifts impossible.

A styrofoam casing has been built in order to suppress temperature variations at the measurement system. However, the effect of the casing was only to delay the variations by a constant offset, their amplitude remained the same. The casing did, however, help to suppress the air currents, reducing the force signal fluctuations during the day significantly.

Due to the unpredictable effect of temperature drifts on the force signal, measurement campaigns are run during times when the temperature and force change is roughly linear, i.e. during the very late afternoon or very early morning. The total measurement time is therefore limited to around 7 hours; the majority of the measurement campaigns are undertaken within 2.5 hours, and sometimes extended to 5 hours.

5.1.3 Vibrations

When measuring forces with a magnet, one might expect that the driving pump, which itself consists of rotating magnets, has an effect on the measurement signal. Therefore, a large steel plate was placed between measurement system and electromagnetic pump but revealed that the rotating pump has no direct effect on the measured force signal.

The measurement system, however, is affected by the pump magnets through vibrations. The pump rotor consists of 12 magnet blocks that are fixed on a circular disk (see fig. 3.2), each giving a discrete pulse to the fluid flow. Consequently, one rotation per minute (rpm) of the disk results in a pulsing frequency of 0.2 Hz. Since the rotational speed never exceeds 80 rpm, the liquid metal is always dragged along in distinct pulses – which propagate through the pipe system and cause the duct to vibrate.

To prove this, the duct has been probed for vibrations with a vibrometer at different rotation speeds. The output was manually read from an oscilloscope. The frequencies detected are shown in fig. 5.2. In the transversal direction (along z, fig. 5.2a), the duct vibrates at a mixture of frequencies that are both dependent (triangles and squares) and independent (crosses and asterisks) of the fluid velocity. The same is true for the longitudinal vibrations (along x, fig. 5.2b). Symbols in both graphs have no physical meaning, other than to help depict the different frequency trends.

The velocity-independent vibrations in fig. 5.2 are at 8.0 Hz and 19.6 Hz (transversal) and at 5 Hz and 15.6 Hz (longitudinal). The velocity-dependent vibrations grow with the pump speed, at the rate of 0.213 Hz per 1 rpm for both vibration directions (represented by the squares). This value is very close to the 0.2 Hz/rpm stated above and may be considered well within the uncertainty of the pump speed. The other increasing frequency (triangles) is the second harmonic of the main frequency.

Fig. 5.3 shows the dominant frequencies at the force measurement system for different pump speeds. Generally, the system has a temporal resolution of 6.3 Hz, but removing all filters increases the sampling frequency to 780 Hz. In the force spectrum, three stationary frequencies are apparent at 10.3 Hz, 15.84 Hz and around 34 Hz, though these are not as constant as the eigenfrequencies of the duct and deviate slightly for different pump speeds.
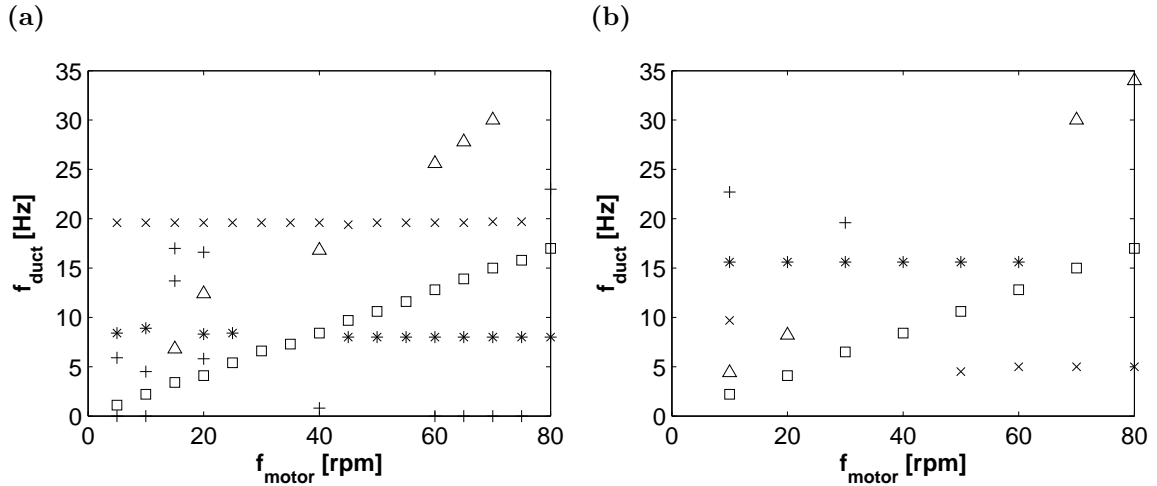
(a)   **(b)**

Figure 5.2: Duct vibrations recorded with a vibrometer in dependence of the pump speed. Each data point represents a peak in the power spectrum of the vibrometer at the respective pump or motor speed. Thus, different symbols do not have a physical meaning, but help identify the trends. (a) Transversal vibrations (along z). For example, when the motor speed is set to 20 rpm, six peaks are visible in the power spectrum: one that belongs to the vibration frequency that depends linearly on the pump speed ($\square$), one that belongs to the second harmonic of that frequency ($\triangle$), two constant frequency peaks ($*$ and $\times$), and two peaks that cannot be attributed to any trend ($+$). (b) Longitudinal vibrations (along x).

The pump-speed-dependent frequencies are found to increase with 0.214 Hz/rpm times the motor speed (squares), with the second harmonic also apparent.

Consequently, the magnet of the measurement system 'feels' the pulses of the electromagnetic pump. For the standard pump speed of 50 rpm the transported vibrations (10 Hz) are faster than the sampling rate of the measurement system (6.3 Hz) and therefore cannot be picked up by the measurement system. At pump speeds of 40 rpm or lower ($\leq$ 10 cm/s), the pulses appear in the raw force signal. However, calculating a mean force at these velocities is still feasible if the measurement time comprises a sufficient number of cycles.

5.1.4 Resolution and repeatability of F_x and F_y

In this subsection two questions will be addressed:

- Can both force components F_x and F_y be resolved with the new measurement setup?
- How good is the repeatability of streamwise and spanwise force measurements?

5.1.4.1 Streamwise force F_x

The streamwise force component F_x is the main force component in the direction of which the signal is strongest. Figure 5.4 shows a step measurement of F_x (5.4a), where the fluid velocity is alternating between 0 and 8.7 cm/s (fig. 5.4b). The magnet is placed immediately adjacent to the duct wall ($z = 10$ mm) and at the vertical center of the duct ($y = 0$). The force has been recorded for at least 500 s at each velocity interval.

With these settings, a maximum force of 1.13 mN is obtained, which is well above the resolution of the measurement system. The force clearly fluctuates around the plateaus;
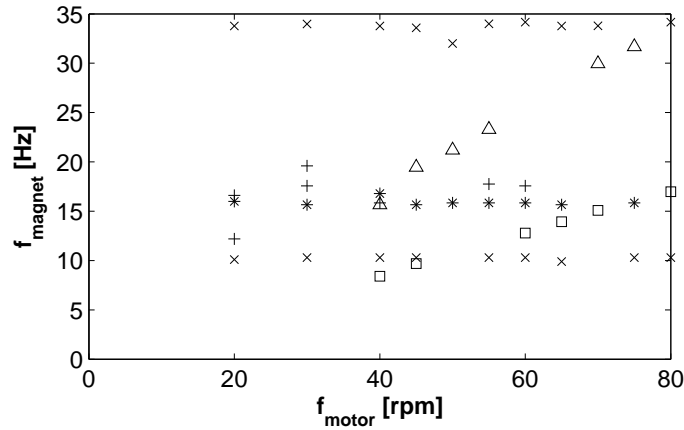
Figure 5.3: Prominent frequencies as they appear in the frequency spectrum of the force signal for different pump speeds. Here, sampling frequency is 781.25 Hz. Symbols signify the same as in fig. 5.2. As in the frequency spectrum for the duct, the magnet vibrates with different frequencies: two depending linearly on the pump speed ($\square$ and $\triangle$) and three frequencies that are independent of the pump speed ($\ast$ and $\times$).

tab. 5.4c gives an overview of the exact heights of the four plateaus and the five recorded zero signals. The plateaus differ from each other by less than 2 %, and the zero signals lie within a range of 2 μN. For comparison: the velocity signals shown in fig. 5.4b differ by slightly less than 1 % from each other at the plateaus, and the larger force plateaus correspond to the larger velocity plateaus.

Another obvious feature in fig. 5.4a is the onset of fluctuations when the fluid starts flowing: At rest, the force signal is fluctuating by less than 1 μN (standard deviation). Once the motor is turned on, the fluctuations reach 75 μN. While at this point it is impossible to say if these fluctuations stem from the duct vibrations or from turbulent fluctuations inside the metal flow, it is worthwhile to note that the measurement system samples fast enough to resolve these fluctuations. A discussion of the origin of the fluctuations is presented in section 5.4.

In summary, F_x can easily be resolved. For $v = 8.6$ cm/s and $z = 10$ mm the force amounts to 10^4 times the nominal resolution of the measurement system. Measurements at lower velocities and larger distances are therefore easy to realize. The repeatability of F_x is to within 2 % of the mean force. This is a rather pessimistic estimate, because some of the error has been induced by the slightly different velocity inputs. On the other hand, the error may increase when the magnet is readjusted between measurements (cf. section 3.7).

5.1.4.2 Spanwise force F_y

A similar measurement series has been performed for the spanwise force F_y. Here, the height of the velocity plateaus is 9.6 cm/s; but the magnet is placed as above to yield maximum forces. The step measurement has been repeated three times, all three resulting force signals are shown in fig. 5.5. The plateaus are marked with dashed lines for better comparison with the zero signals.

The difference in force between $v = 9.6$ cm/s and $v = 0$ is around 5 μN. While the nominal resolution of the measurement system is 0.015 μN [133], the mean signal is almost completely

(a)

(b)

(c)

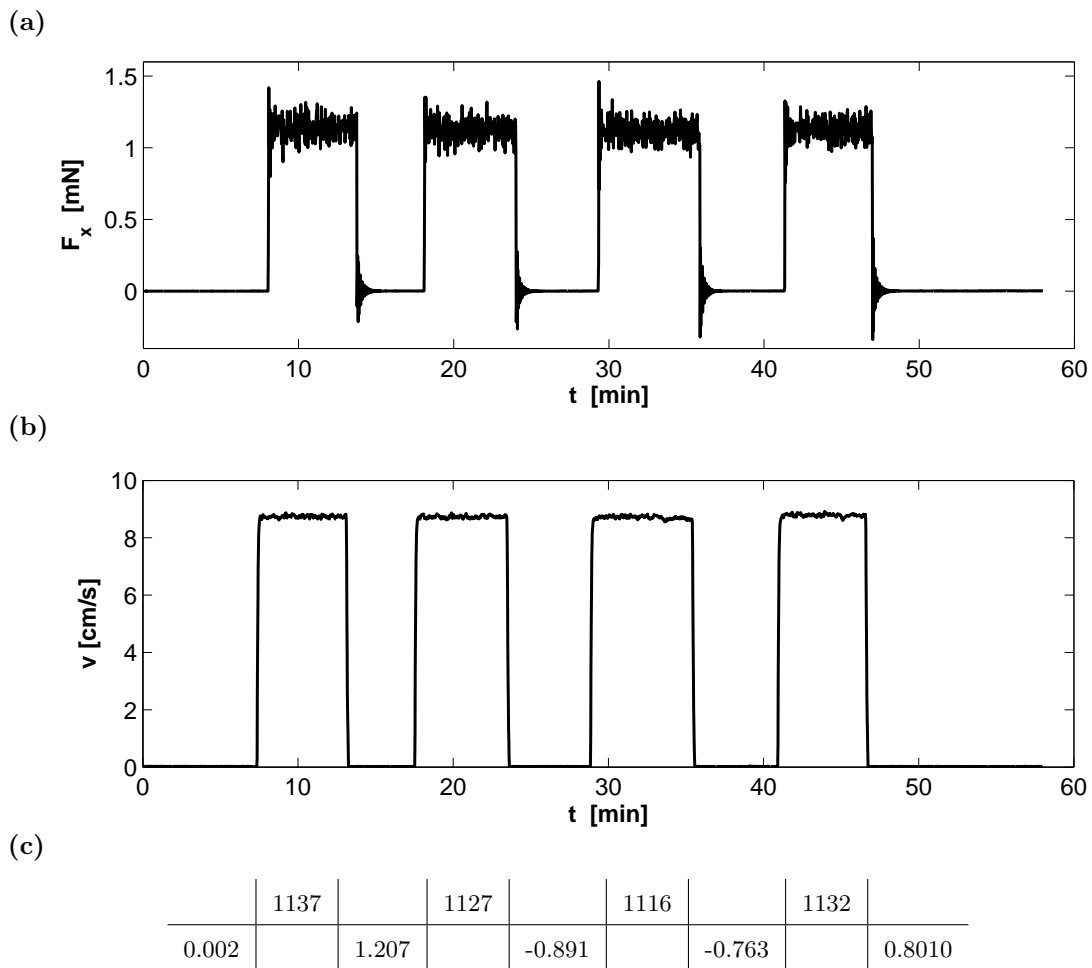|	1137		1127		1116		1132	
0.002		1.207		-0.891		-0.763		0.8010

Figure 5.4: Step measurements of the streamwise force component F_x on the 10 mm magnet. (a) Force signal for $z = 10$ mm and $v = 8.7$ cm/s. (b) Velocity input: The pump has been repeatedly turned on and off for at least 500 s each. (c) Table displaying the means of the force signal, both at the plateaus (top row) and for the zero signals (bottom row). Horizontal position of the numbers is matched to the raw data above for better readability.

obscured by the fluctuations that set on when the fluid is flowing ($\sim 50\,\mu\text{N}$). Additionally, even a slight drift such as that in fig. 5.5b is sufficient to conceal the signal. The repeatability of F_y is only to within $15\,\%$, of which the mean velocity uncertainty accounts for only a very small amount. The standard deviations of the three signals for F_y differ by $38\,\%$ (F_x: $6\,\%$). Possibly this increased uncertainty is due to the highly turbulent flow inside the duct.

5.1.5 Reaction time

A deeper analysis of the data presented in fig. 5.4 will answer the question of how fast the measurement system is reacting to a change in velocity, or in our case, how long it takes until the force signal has reached the plateau value. For this, about ten minutes of the measurement in fig. 5.4 have been extracted and displayed in fig. 5.6. In addition to the raw signal (black), the mean values of both the plateau and the two adjacent zero signals are shown (red). At each force jump, the last value of the old steady state and the first value of the new steady state are marked with a red cross. That is, the first two red crosses mark the times when the force starts rising (last value below the zero line) and finishes rising (first value above the plateau), and the last two crosses mark the start and end of the reverse process.

The upward jump in force (first two crosses) takes only about 3 seconds. This is negligible considering that the duration of a typical measurement must be several dozens of seconds in order to be able to average out the turbulent fluctuations. The drop in force (last two crosses) after turning the pump off is equally fast. However, there is an overshoot followed by some oscillations when the pump is turned off that last for about one and a half minute. The reason for these oscillations becomes clear if one recalls how the measurement system works: The magnet sits on a short rod-like extension from the measurement box and is dragged along with the fluid flow. When the pump is turned off abruptly, the fluid comes to a halt, releasing the magnet that snaps back to its neutral position. Inertia causes the magnet to overshoot, resulting in the observed oscillations. Consequently, if a second zero signal is needed for drift correction at the end of a long force measurement series, it should be significantly longer than the stated $1.5\,\text{min}$.

5.1.6 Measurement procedure

The above findings must be taken into account when conducting measurements on the liquid metal duct. A detailed summary of how measurements are performed can be found in appendix C (spiced with some practical advice). Here, only the most important conclusions are presented:

1. Positioning the magnet close to the duct is crucial, but the duct vibrations prohibit the magnet being placed too close to the duct wall. Therefore, the magnet should always be positioned when the pump is running at its maximum speed ($\omega = 70$ or $80\,\text{rpm}$). The force signal becomes unstable when the magnet is mechanically touching the duct wall, thus keeping an eye on the force signal helps to place the magnet just out of reach of the duct vibrations.
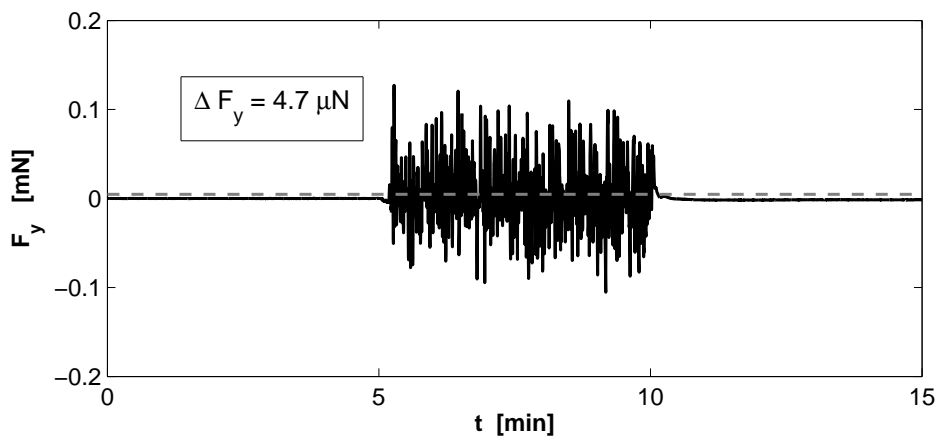
(a)
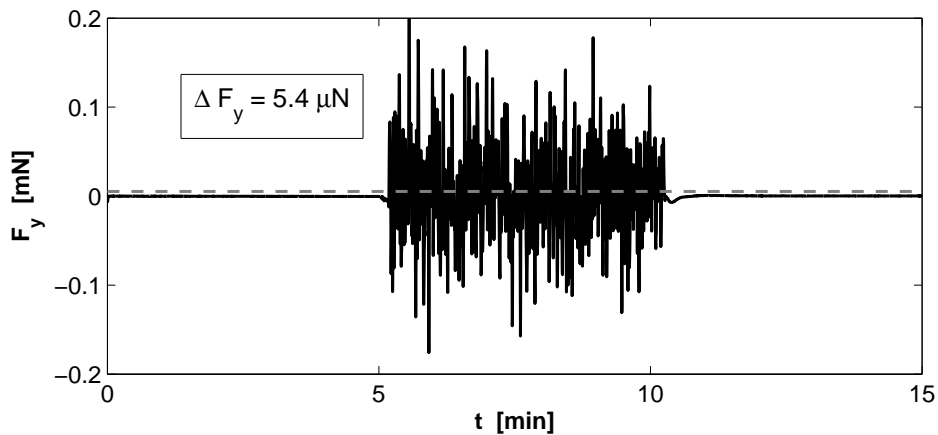
(b)
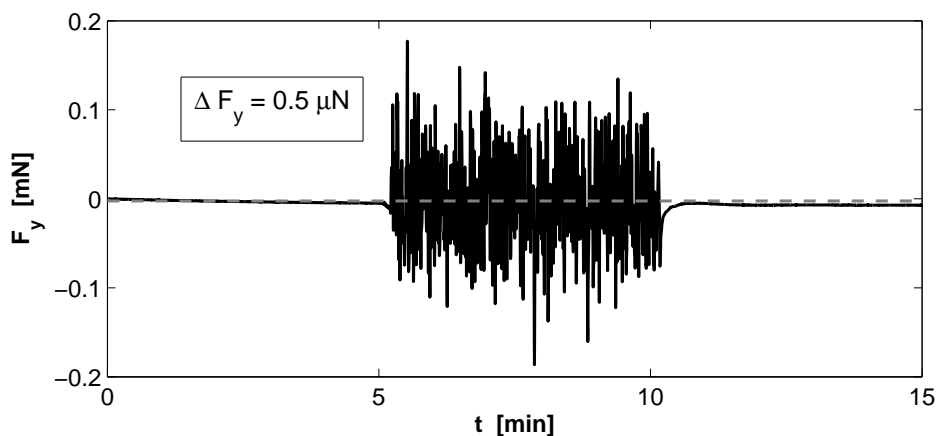
(c)

Figure 5.5: Three iterations of the same step measurement of the spanwise force component F_y on the 10 mm magnet with $z = 10\,\text{mm}$ and $v = 9.7\,\text{cm/s}$ in the interval $300\,\text{s} \le t \le 600\,\text{s}$. Dashed horizontal lines mark the mean of the force signal between 5 min and 10 min. They are extended across the entire figures for easier comparison with the zero signal. (a), (b), and (c) are identical in their settings. (b) stands out in that a slight drift is obscuring the difference between the mean of the plateau and the mean of the zero signal.
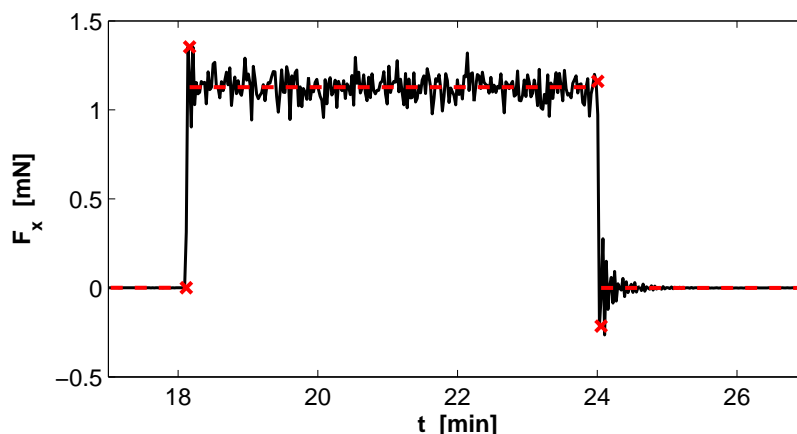
Figure 5.6: Excerpt of the measurement shown in fig. 5.4. Dashed red lines mark the mean values of the force signal and red crosses mark the start and end of the jumps in the signal. Both pairs of crosses are each about 3 s apart. After the pump has been turned off, the force signal shows oscillations about the zero signal for about 1.5 min.

2. The typical measurement duration is 50 s for each data point. At the sampling frequency of 6.35 Hz, this yields approximately 300 values.
3. Waiting times for the velocity series are at least 200 s.
4. By all means, it should be avoided to try to bake a raspberry cake in the furnace neighboring the duct setup.
5. The first measurement step is always with still motor to obtain the zero signal.
6. With typically 60 steps in z and 100 steps in y each 0.5 mm (placement always back and forth), the total duration of a measurement series is 2 to 3 hours.

5.2 Parameter studies on the unperturbed duct flow

This section presents the results for the unperturbed duct flow in the new measurement setup. First, parameter studies of the streamwise force F_x are presented varying the distance z of the magnet to the duct, the vertical position y of the magnet beside the duct, the mean velocity v, and the magnet size D. Then follow the same parameter studies for the spanwise force F_y, only omitting magnet size dependence.

5.2.1 Streamwise force $F_x(z, y, v, D)$

5.2.1.1 Distance dependence $F_x(z)$

The magnet is placed at mid-height of the duct and the pump speed is set to the maximum velocity of 9.6 cm/s. The distance of the magnet to the duct is gradually decreased from 4 cm to 1 cm and then increased again. The first half of the resulting force signal is plotted in fig. 5.7a. The motor remained turned off for the first 50 s of the measurement series in order to be able to determine the absolute forces from the zero signal; the corresponding data point lies on the abscissas in figs. 5.7b and 5.7c at $z = 40$ mm. Then the motor has been turned on, and the magnet moved in steps of 0.5 mm every further 50 s.

The mean of the streamwise force is displayed in fig. 5.7b, and as one can see from the inset, the force-distance relationship can be approximated by a power-law with an exponent of -3.8, which is the same as the one found in chapter 4. The deviations from this law at distances beyond 3.5 cm are not reproducible and rather seem to be an artefact due to the signal being on the edge of the resolution of the measurement system. Note that the power-law is only approximate, as the distances displayed are in the transition region between the far-distance power-law ($F_x \sim z^{-7}$) and the close-distance power-law ($F_x \sim z^{-2}$, cf. [130]).

As one can see from the raw signal in fig. 5.7a, placing the magnet closer to the duct increases not only the mean force, but also the force fluctuations. Accordingly, the standard deviation of the force signal shows a very similar behavior to the mean force (see fig. 5.7c), including a similar exponent of decay with distance (-4.0). To prove that the standard deviation is practically increasing at the same rate as the mean force, the ratio of the two has been plotted in fig. 5.7d. Again, the deviations at distances larger than 3.5 cm coincide with the very weak mean force signal, meaning that small deviations are amplified because they are in the denominator. The outliers at $z = 10$ mm are not reproducible.

5.2.1.2 Spanwise position dependence $F_x(y)$

The spanwise position of the magnet is changed experimentally by moving the magnet in the vertical direction beside the duct wall. The setup is such that the middle of the possible positions is not coinciding with the mid-height of the duct ($y = 0$), but is about 4.5 mm above it. Thus, the resulting force profile extends beyond the upper region of the duct (positive y-direction) but does not reach the bottom (negative y-direction).

The measurement has been performed with the same settings as for the $F_x(z)$-dependence, namely with $v = 9.6$ cm/s and sampling durations of $t = 50$ s. The magnet has been placed immediately adjacent to the duct wall at $z = 1$ cm, and the vertical position has been scanned between -20.5 mm $< y < 29.5$ mm in steps of 0.5 mm.

Fig. 5.8a shows the raw force signal for one scan starting at the upper limit and ending at the bottom. The small offset just after the start of the measurement is again due to the initial recording of the zero signal. The data point representing the zero signal can be found both in the mean force diagram (fig. 5.8b) and in the standard deviation diagram (fig. 5.8c), both at $y = 29.5$ mm. In fig. 5.8d, the ratio of the standard deviation to the mean force (signal-to-noise-ratio) is shown.

The shape of the mean force distribution resembles a parabola within the boundaries of the liquid metal $|y| \leq 25$ mm, with forces significantly smaller at the edges of the duct. It should be noted here that the metal flow is highly turbulent ($Re = 7100$), the consequence being that the force profile does *not* resemble the (mean) velocity profile along the (center of the) duct. As the magnet is mostly influenced by liquid metal flowing close to the duct walls, the force profile in fig. 5.8b merely indicates that velocities beyond the boundary layers are higher at mid-height of the duct than at either bottom or top.

The standard deviation again shows a similar behavior like the mean force signal, but at about a tenth of the magnitude and with higher noise. As the force fluctuations are likely to be caused by duct vibrations, this behavior is presumably a result of the magnet "seeing" the full duct volume at mid-height, and only a fraction at the upper and lower edge.
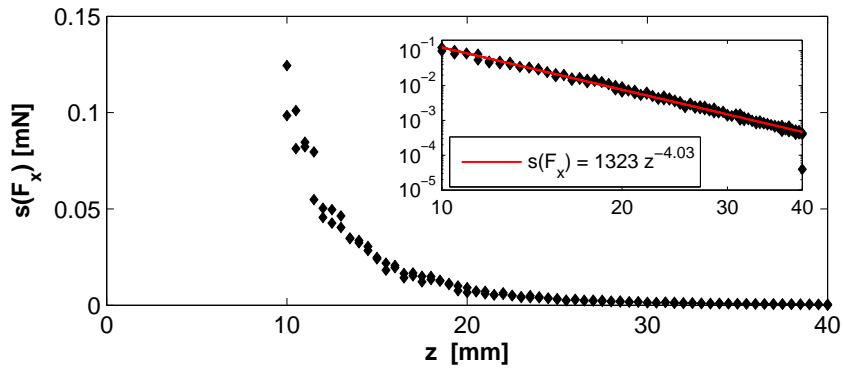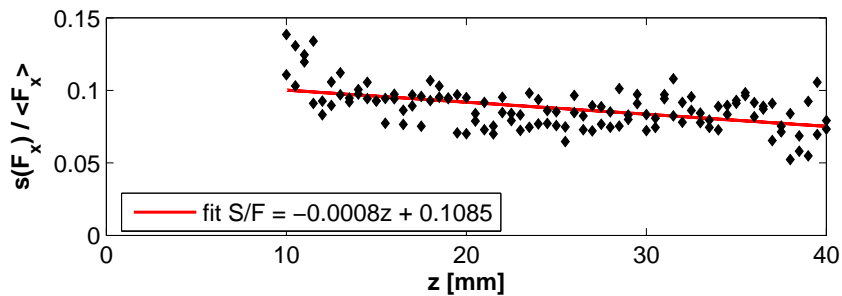
(a)
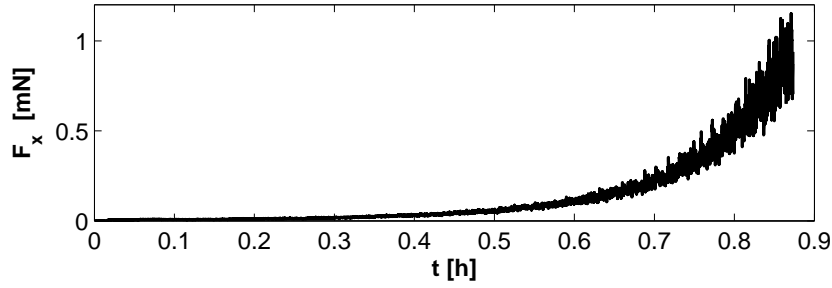
(b)
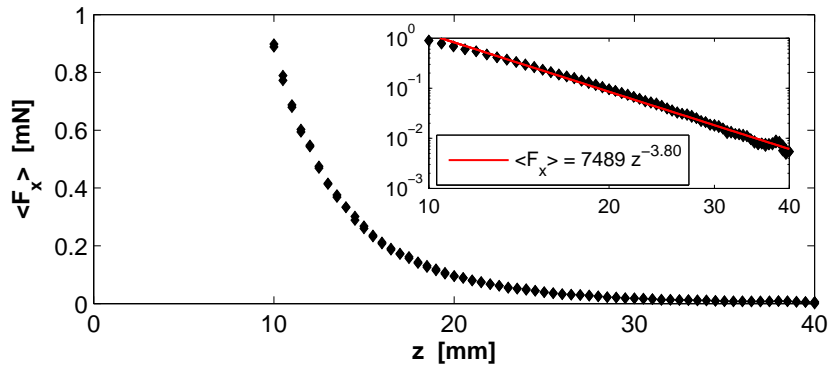
(c)

(d)

Figure 5.7: Dependence of the streamwise force F_x on the (horizontal) distance of the magnet to the duct. The fluid flows at the mean velocity of $9.6\,\mathrm{cm/s}$ and the magnet is vertically positioned at $y = 0$. (a) Raw force signal. Distance decreases every $50\,\mathrm{s}$. (b) Mean of the force signal versus distance. The inset shows a logarithmic plot of the mean force (black symbols) with a power-law fit (red line). (c) Standard deviation. Logarithmic plot (black symbols) with power-law fit (red line) in the inset. The "outlier" at $z = 40\,\mathrm{mm}$ corresponds to the first $50\,\mathrm{s}$ when the motor is turned off. (d) Ratio of the standard deviation to the force mean – practically constant for all distances.
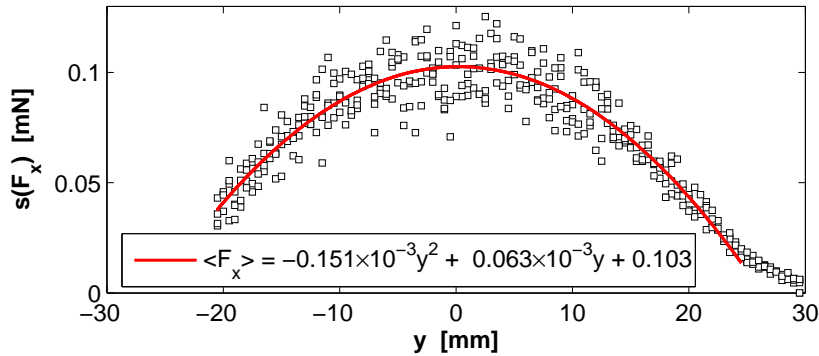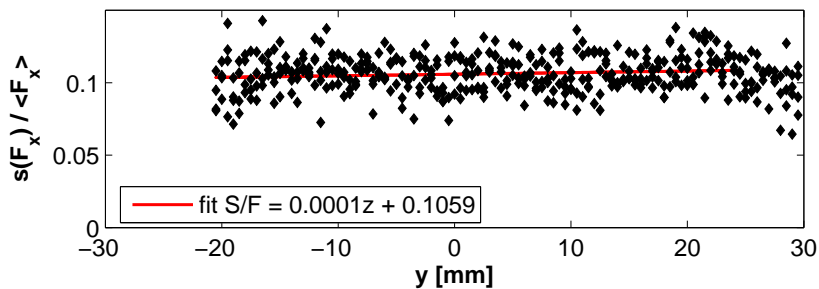
(a)
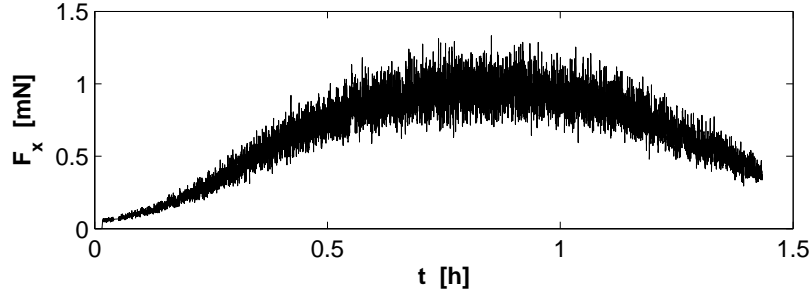
(b)
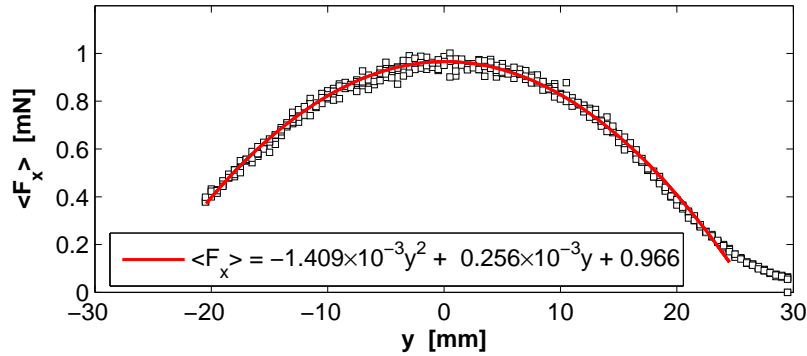
(c)

(d)

Figure 5.8: Dependence of the streamwise force F_x on the spanwise position y. Mean velocity is $9.6\,\text{cm/s}$ and distance to the duct is $z = 10\,\text{mm}$. (a) Raw signal. Magnet is shifted downward every $50\,\text{s}$, starting from the top of the duct ($y = 29.5\,\text{mm}$). (b) Mean of the force signal versus spanwise position. The shape of the force profile can be fitted with a parabola (red line). (c) Standard deviation. The shape is similar to the mean force signal, magnitude is about a tenth. Accordingly, the shape of the fit is a parabola, too (red line). The "outlier" on the abscissas in (b) and (c) corresponds to the zero signal of the first $50\,\text{s}$ when the motor is turned off. (d) Ratio of standard deviation and mean force over the width of the duct.

5.2.1.3 Velocity dependence $F_x(v)$

This section aims at determining how the streamwise force F_x depends on the mean velocity of the liquid metal. To produce maximum forces, the magnet is placed at the closest possible distance to the duct at mid-height, i.e. at $z = 10\,\text{mm}$ and $y = 0$. Although the velocity changes within a few seconds after the pump speed is changed, measurements were taken over 5 minutes each, and the pump speed has been either increased or decreased in steps of 5 or 10 rpm to exclude hysteresis effects.

For the raw force signal shown in fig. 5.9a, the pump speed has been increased in steps of 5 rpm from 0 to 80 rpm, corresponding to a velocity change of around 1 cm from 0 to 13.5 cm/s. This average velocity is obtained with the volume flow meter, i.e., it is the time-averaged global flux divided by the cross sectional area of the test section.

As fig. 5.9b shows, the streamwise force depends on the mean velocity linearly in the interval $1\,\text{cm/s} < v < 14\,\text{cm/s}$. For velocities below 1 cm/s the force is expected to deviate from this linear behavior, because the velocity field is significantly altered by the magnetic field ($N \gg 1$). Velocities above 13.6 cm/s cannot be reached with the current setup.

The standard deviation again follows the behavior of the mean force and increases linearly with velocity; the ratio of $s(F_x)$ and F_x remains constant at about 1/15 for all measured velocities.

5.2.1.4 Magnet size dependence $F_x(D)$

So far, the standard magnet cube of 1 cm edge length has been used for all measurements. The resolution of the measurement system is high enough to allow measurements with smaller magnets that produce weaker forces. Although designed for the 1 cm cube weighing 8 grams, the measurement system can carry larger magnets up to the 1.5 cm edge length cube. The magnets used for measurements are: 5 mm, 8 mm, 10 mm, 12 mm, and 15 mm cubes, and one cylindrical magnet of 1 cm diameter and 1 cm height.

The above three measurement series have been repeated with all these magnets and the results are presented in figs. 5.10, 5.13, and 5.14.
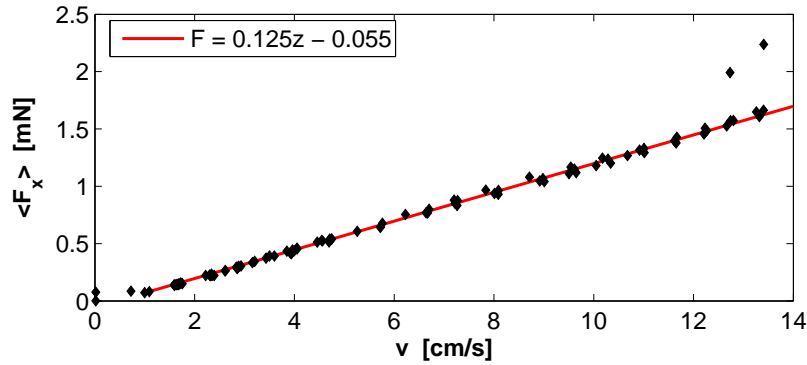
Distance dependence

For the distance variation, each magnet is placed such that at minimum distance one side of the cube is (almost) touching the duct wall and the maximum distance is exactly 3 cm away from the minimum. Since the distance is always determined from the magnet center, the minimum distance is different for every magnet. That is, the smallest cube (5 mm) is placed in the range $7.5\,\text{mm} \leq z \leq 37.5\,\text{mm}$, with the smallest distance given by the wall thickness w and half the magnet size, and the largest cube (15 mm) is placed within $12.5\,\text{mm} \leq z \leq 42.5\,\text{mm}$. The cylinder is positioned with its bottom parallel to the duct wall and is thus placed like the 10 mm-cube, i.e. within $10\,\text{mm} \leq z \leq 40\,\text{mm}$.

The measurement procedure is the same as for the previous measurements, i.e. first, 50 seconds of zero signal are recorded, then the motor is turned on to yield a flow velocity of 9.6 cm/s and after every 50 s the magnet is positioned closer to or farther away from the duct in steps of 0.5 mm.
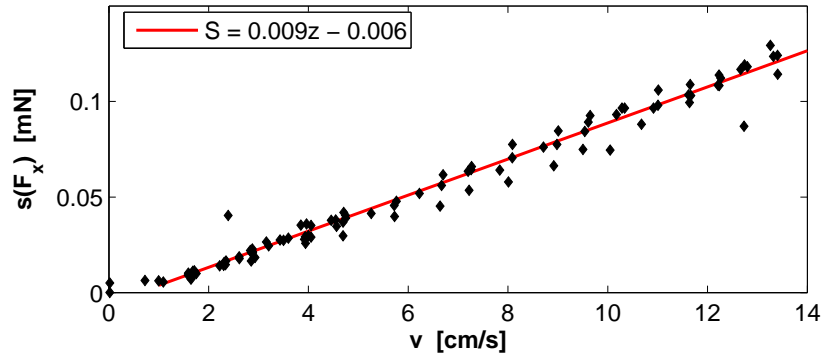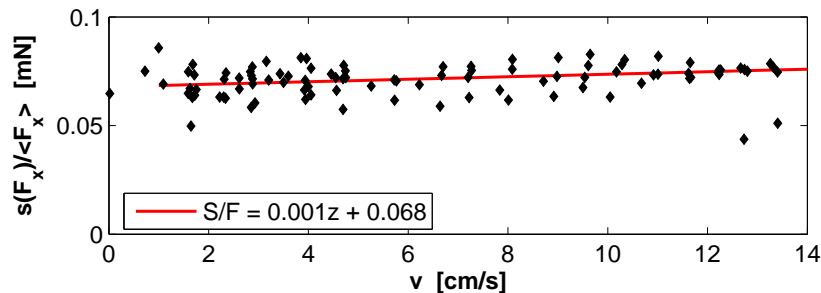
(a)
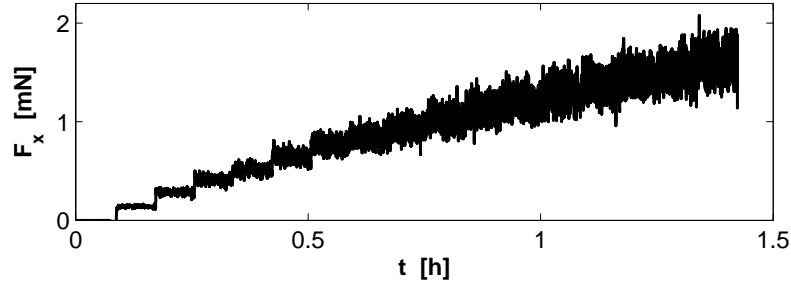
(b)

(c)

(d)

Figure 5.9: Dependence of the streamwise force F_x on the mean velocity v. Vertical position of the magnet is at mid-height of the duct $y = 0$ and the distance is $z = 10$ mm. The measurement has been repeated several times in varying step sizes of v. (a) Raw signal of the first 15 steps. Velocity is increased in steps of around 1 cm/s from 0 to 13.5 cm/s in intervals of 5 minutes each. (b) Mean of the force signal versus mean velocity. The data can be fitted with a straight line in the range of 1 cm/s $< v <$ 13.5 cm/s. Larger velocities cannot be reached in the current setup. (c) Standard deviation. The increase is linear. (d) Ratio of standard deviation and mean force, remaining constant at around 0.07 over the entire velocity range.

(a)
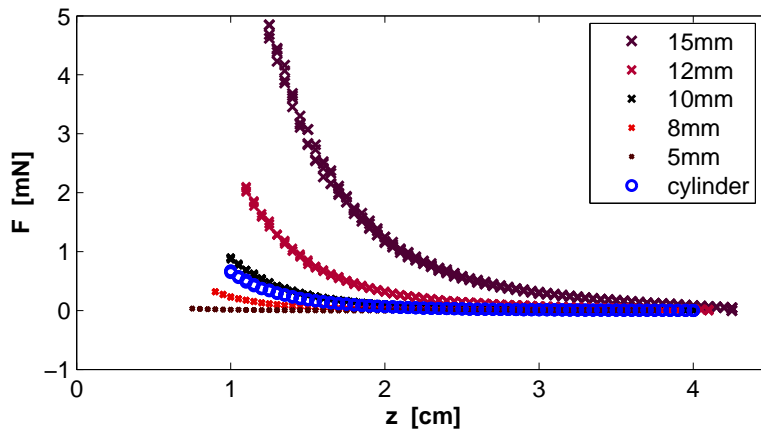
(b)
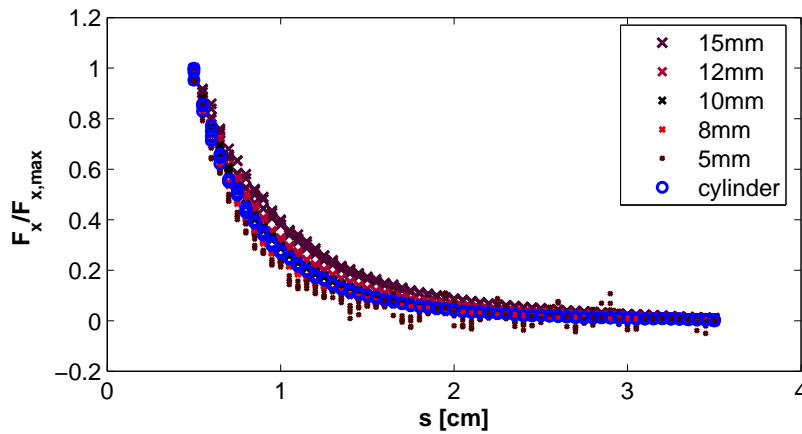
(c)
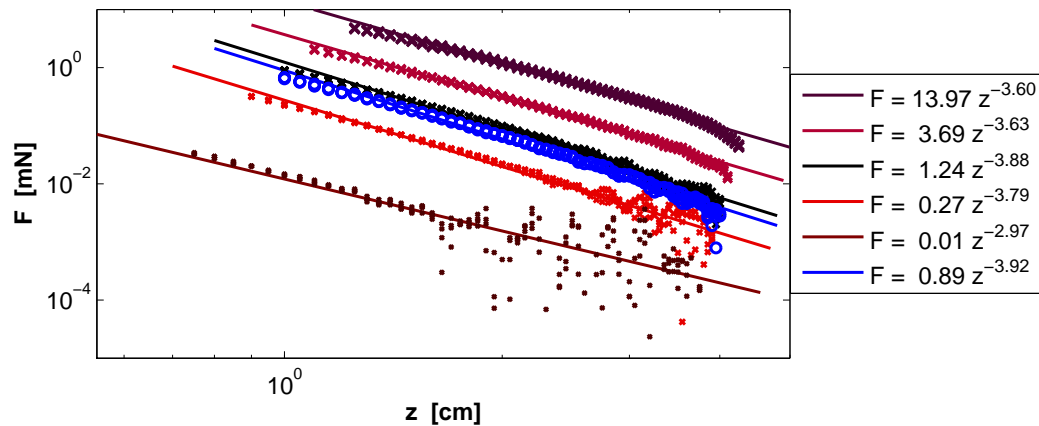
Figure 5.10: Dependence of the streamwise force F_x on the distance z for different magnets. Vertical position is always $y = 0$ and mean velocity is $v = 9.6\,\mathrm{cm/s}$. (a) Mean force versus distance to the duct z. (b) Normalized forces vs. the distance s of the magnet *surface* to the duct. Normalization is performed by dividing each force profile by its respective maximum at $s = 0.5\,\mathrm{cm}$. (c) Log-log plot of the mean force to distinguish the different power-laws.

The resulting mean forces are plotted for all six magnets in fig. 5.10a. One can see that the general behavior of a fast, continuous decay is the same for all magnets. The magnitude of the force is highest for the largest magnet and lowest for the smallest magnet, with the force being about 150 times higher for the 15 mm magnet than for the 5 mm magnet when the magnet is immediately adjacent to the duct wall. Remember that the theory predicted a 700 times higher force (tab. 5.1). The cylindrical magnet, comparable in size to the 1 cm cube, produces forces only slightly smaller than the cube (670 μN as compared to 898 μN at $z = 1$ cm).

Figure 5.10b shows the same data as fig. 5.10a, but normalized such that the maximum force of all magnets is 1 and the distance range is shifted into a common 3 cm-intervall. Despite the curves being very close to each other one can make out the steeper slope of decay for the smaller magnets and the slower decay for the larger magnets.

The same trend is visible in fig. 5.10c, where the data is plotted in a log-log-plot: Besides the apparent drop in forces with decreasing magnet size, power-law fits reveal that also the slope of decay is steepening from -3.6 for the 15 mm magnet to -3.8 for the 8 mm magnet. The fit for the 5 mm magnet shows an exponent of -3.0, but this should be treated with caution, as the data scatters very strongly around the straight line, and a somewhat oscillating behavior is apparent for the 5 mm magnet in fig. 5.10b at distances just beyond 1 cm. Although not understood in detail, the oddity seems to be an effect of the measurement system carrying too small a dead weight.

Now one could ask, 'how much force one gets for their magnet'. That is, how much does the resulting force increase if larger magnets of comparable magnetization density are employed. To answer this question, the measured force is divided by the respective volume of the magnet and the magnetic field (see y-axis in fig. 5.11). As the decay of the force with increasing distance is chiefly determined by the decay of the magnetic field, and the decay of the magnetic field is different for each magnet, the normalizing B-field factor is chosen not to be a constant (like the maximum flux density obtainable inside the duct, $B(s = 5$ mm$)$), but rather the force at each distance from the magnet surface ($s \geq 5$ mm) is divided by the magnetic flux density at that distance. That is, the force corresponding to the magnet being placed immediately beside the duct is divided by the magnetic flux density that is measured 5 mm off the magnet surface, but the force at a distance of 1 cm is divided by $B(s = 1$ cm$)$ of the respective magnet. For more details on the fields of the six magnets, see fig. 3.10.

The result of the normalization is shown in fig. 5.11. The x-axis shows the distance s from the magnet surface to allow for direct comparison of the magnets. Note the difference between s and z: s denotes the distance to the magnet *surface*, z denotes the distance to the magnet *center*. The y-axis shows the force in mN that is obtained per cm^3 magnet material and T magnet strength. Since force and B-field decay at different rates, the resulting curve is not a straight line. Still, one can see that for magnet cubes very near to the duct the relative forces coincide. The amount of magnetic material needed to generate a higher force is directly proportional to the gain in force, as long as the magnetization density of the magnets is similar. This remains true at some distance from the duct for the larger three magnet cubes, as the curves coalesce even for higher distances. However, the smaller two cubes clearly deviate from this result, possibly due to higher manufacturing inaccuracies.
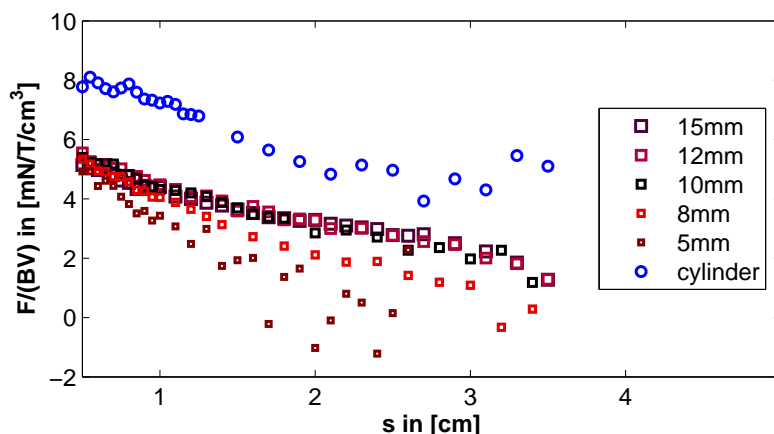
Figure 5.11: Compensated force vs. distance of the magnet surface from the duct. The three larger cube magnets all produce the same force per cm^3 magnet material. The smaller cubes deviate from this proportionality. The cylindrical magnet produces a significantly higher force per cm^3 material. All magnets have a similar magnetization density.
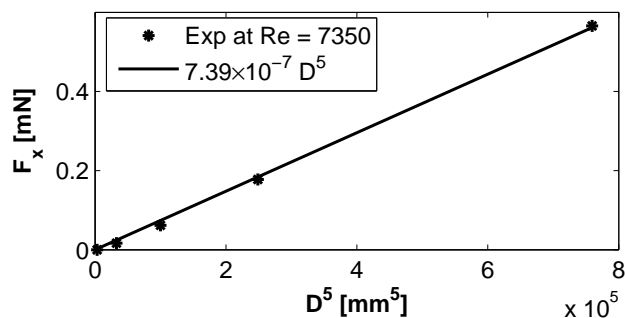

Figure 5.12: The dependence of the streamwise force component F_x on the size of the magnet (edge length). $v = 9.6\,\text{cm/s}$, $y = 0$, and $s = 5\,\text{mm}$.

Nonetheless, the strongest deviation stems from the cylindrical magnet. This is probably due to the different shape of the magnetic field compared to the cube magnets. However, further measurements with cylindrical magnets would be necessary to exclude side effects of the measurement system such as for the 5 mm magnet.

How does the force increase with increasing magnet size? Fig. 5.12 compares the forces produced by each magnet with the size of the respective magnet. For this, the magnization densities of the cubes are assumed to be equal and the forces are extracted from measurements with the same parameters, i.e. $v = 9.6\,\text{cm/s}$ and $z = 1.25\,\text{cm}$ for all magnets. The chosen distance corresponds to the minimum distance for the largest magnet (15 mm magnet), so that all magnets are placed with their center at the same position. The best fit for the force was found for $F_x \sim D^5$. The zero y-intercept suggests that there is no force on a dipole, which is certainly not true. However, remember that the fit is obtained with only five data points, out of which four are obtained with magnets that the force measurement system is not designed for, so the obtained proportionality should be regarded as qualitative.

Velocity dependence

| | | L [cm] | | | | | | | | | | | | | | |
| | | 0.5 | | | 0.8 | | | 1.0 | | | 1.2 | | | 1.5 | | |
		THEORY	EXPERIMENT	RATIO	THEORY	EXPERIMENT	RATIO	THEORY	EXPERIMENT	RATIO	THEORY	EXPERIMENT	RATIO	THEORY	EXPERIMENT	RATIO
	0.75	48	32	1.5												
	0.90	28	20	1.4	463	316	1.5									
	1.00	20	14	1.4	337	238	1.4	1285	888	1.4						
	1.10	15	10	1.5	253	177	1.4	964	679	1.4	2879	2013	1.4			
z [cm]	1.25	10	8	1.3	172	114	1.5	656	469	1.4	1958	1516	1.3	7468	4842	1.5
	1.75	4	2	1.8	62	37	1.7	237	162	1.5	707	503	1.4	2696	1919	1.4
	2.25	2			29	16	1.8	110	61	1.8	328	209	1.6	1252	839	1.5
	2.75	1			16	8	1.9	59	27	2.2	177	106	1.7	675	425	1.6
	3.25	1			9	4	2.3	35	12	2.9	105	59	1.8	402	236	1.7
	3.75				6	3	2.0	23	8	2.8	67	29	2.3	257	122	2.1

Table 5.2: Measured drag forces (in µN) for the five employed magnet sizes. Structure of the table is analogous to table 4.1. Data gaps for the 5mm magnet are due to the unphysical jumps at larger distances (see fig. 5.10). Theoretical prediction overestimates the forces by a factor of about 1.5 that is roughly constant for the five magnets, but increases to about 2 for the largest distances of the magnets to the duct.
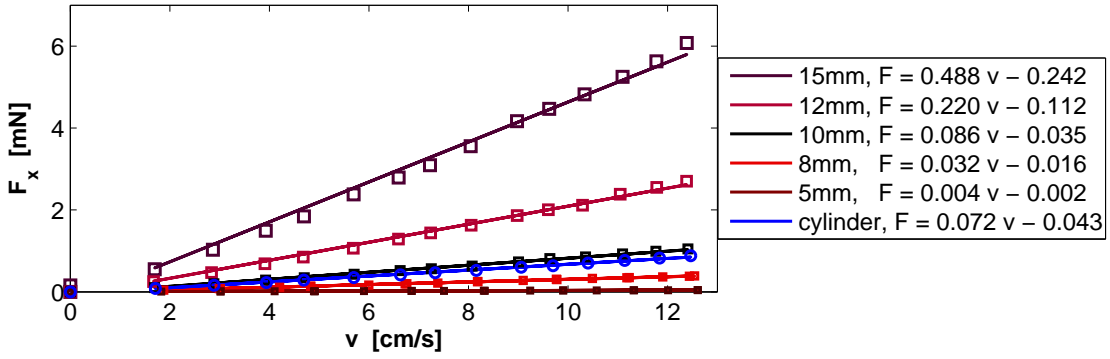
Figure 5.13: Dependence of the streamwise forces produced with the six different magnets on the mean velocity. Vertical position is always at mid-height, and horizontal position is such that the magnet surfaces are directly at the duct wall. Behavior between 0 and $1\,\text{cm/s}$ is expected to be nonlinear and therefore is excluded from the straight line fit (interaction parameter $N \gg 1$).

To determine the velocity dependence, the magnets have always been placed at the closest possible distance to the duct, that is with their surfaces (almost) touching the duct wall. Vertically, they are aligned such that their centers are at mid-height of the duct. This way, forces produced are always maximum. The velocities investigated lie in the range $0 \leq v \leq 12.6\,\text{cm/s}$.

The resulting data points are plotted in fig. 5.13. All six curves could be fitted with a straight line, with steeper slopes for the larger magnets. The cylindrical magnet produces forces slightly lower than that for the $10\,\text{mm}$ cube. As the force is expected to behave non-linearly at very low velocities, none of the straight lines passes through the origin.

Spanwise position dependence

To measure the dependence of the streamwise force on the vertical position, the magnets are placed immediately adjacent to the duct wall, irrespective of their size. The pump speed is set to $9.6\,\text{cm/s}$. Magnets are then positioned along the side of the duct with the range in vertical positions being slightly off center, as explained previously.

The results are visualized in fig. 5.14. The mean forces are shown in fig. 5.14a, in order to compare the magnitudes of the forces produced by the different magnets. A comparison of the shapes of the force profiles is shown in fig. 5.14b, where the data are normalized with the maximum force corresponding to each magnet, i. e. the plot shows the force F_x of each magnet divided by the maximum force $F_{x,max}$ of the same magnet. One can see that most of the profiles are coinciding with only very minor deviations. The only magnet differing significantly from the common curve is the small $5\,\text{mm}$ magnet, presumably for the same reasons as above.

Last, let us address the question how well the measured forces correspond to the forces predicted in section 5.1. Table 5.2 gives an overview of the forces obtained both from theory and experiment. All theoretical values are close to the experimentally obtained values, but overestimate the experimental data by a factor of 1.4 that is constant for all magnets. This factor, however, increases as the magnets are placed farther from the duct and forces become significantly weaker. Nonetheless, considering the unrealistic assumptions of the model,

(a)
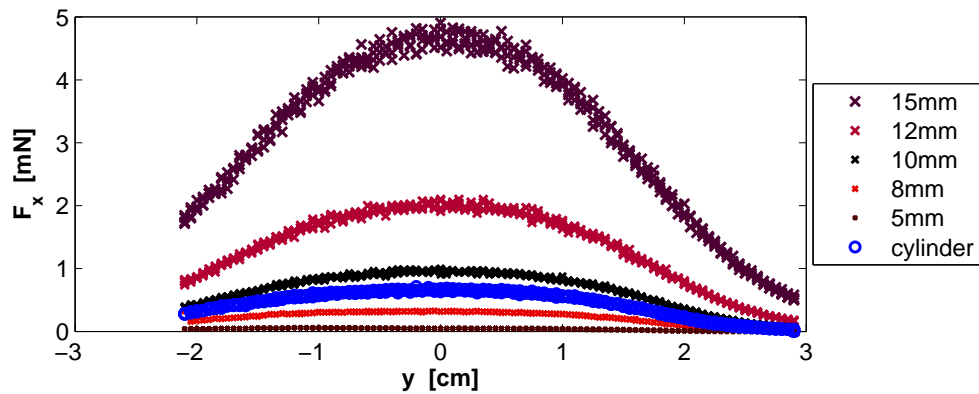
(b)
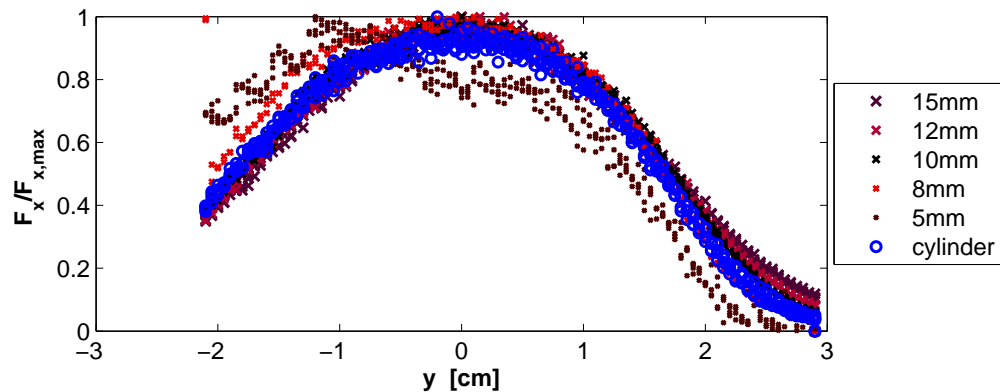
Figure 5.14: Dependence on the vertical position of the streamwise forces for the six magnets. Horizontal position is always with the magnet (almost) touching the duct wall ($s = 5$ mm, flow velocity is always $v = 9.6$ cm/s. (a) Mean forces. Maximum for each magnet is at 4.9 mN, 2.1 mN, 1.0 mN, 330 µN, 60 µN, and 720 µN in the order as the magnets appear in the legend. (b) Mean forces normalized with the respective maximum force of each magnet. Except for the two magnets smaller than the standard magnet, the curves of all magnets collapse onto one.

the theoretical predictions are surprisingly good. Experiments with larger magnets were significantly farther off [142].

5.2.2 Spanwise force $F_y(z, y, v)$

So far, only the streamwise force component has been investigated. To measure the spanwise force component, the measurement system is rotated by $90\,°$ such that the sensitive direction coincides with the direction of gravity.

The flow velocity in the vertical direction is expected to be very low. Indeed, the streamwise force component is the strongest, and a spanwise force is expected only as a result of turbulent fluctuations and, possibly, of secondary flows in the corners of the duct (cf. section 2.1.2).

5.2.2.1 Distance dependence $F_y(z)$

The measurement of the distance dependence of the spanwise force proves to be rather tricky. Although thermal drifts are very small over the measurement periods presented here, they are in the order of the expected force signal. Additionally, the force signal stemming from the duct flow is superimposed with a signal stemming from the mere positioning of the magnet. To show this, the raw signal for the distance dependence at $9.6\,\mathrm{cm/s}$ in fig. 5.15a is accompanied by the same measurement series but for the zero signal in the inset. In both cases, the magnet is moved from $z = 4\,\mathrm{cm}$ to $z = 1\,\mathrm{cm}$ in intervals of $50\,\mathrm{s}$. Thus, the tiny steps barely visible in the first half hour of the measurement in the main window of fig. 5.15a are entirely due to the change of the magnet position relative to the duct. The zero signal in the inset is due to magnetic parts in the vicinity of the measurement system and is subtracted from the total signal after averaging.

The resulting mean forces are shown in fig. 5.15b for three different velocities. While being practically zero at large distances, the force mean increases for all three velocities when the magnet is approaching the duct. However, the noise is so strong that the values are highly scattered at close distances, impeding any attempt at reasonably fitting the behavior. To the contrary, the standard deviation, resembling the fluctuations on the raw force signal, proves to follow a clear power-law. Even more so, the standard deviation of the force generated by faster fluid flows is higher than that for slower flow velocities.

Since secondary flow is expected to be mainly in the duct corners, the measurements have been repeated at the lower edge of the duct instead of mid-height. However, the result is similar to that shown in fig. 5.15: The mean force is highly scattered in the vicinity of the duct, but both the standard deviation and the mean force are slightly less in magnitude than at mid-height.
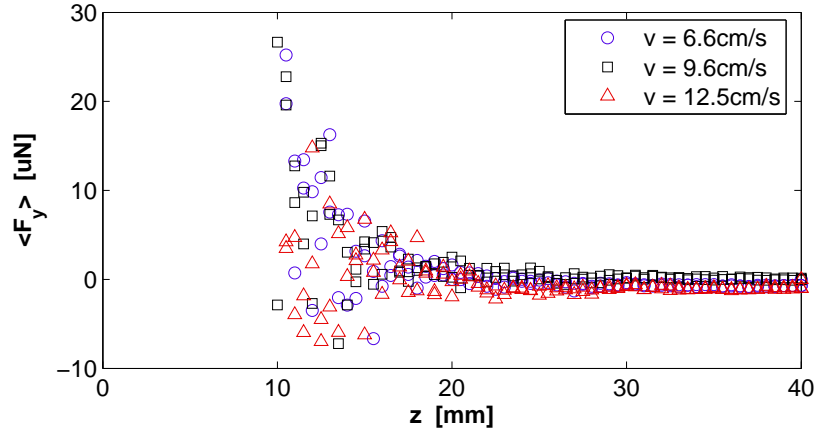
5.2.2.2 Velocity dependence $F_y(v)$

The velocity dependence measurement of the spanwise force is performed analogously to the measurement of the streamwise force. The $10\,\mathrm{mm}$ magnet cube is placed immediately adjacent to the duct wall at mid-height of the duct, and the velocity is varied in different step sizes both upward and downward.

(a)
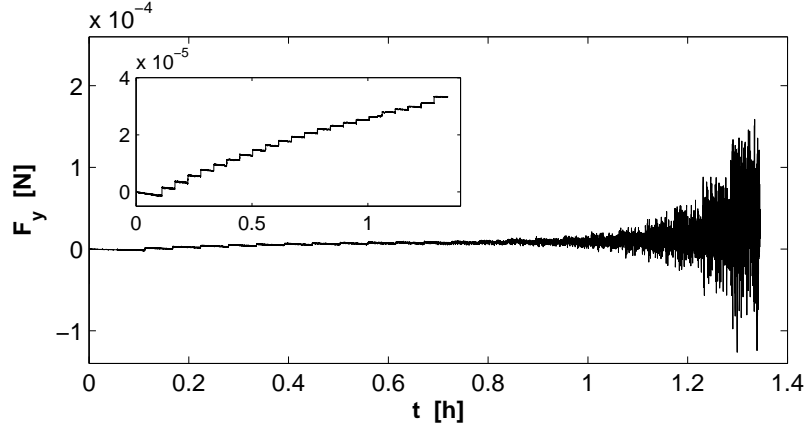
(b)

(c)
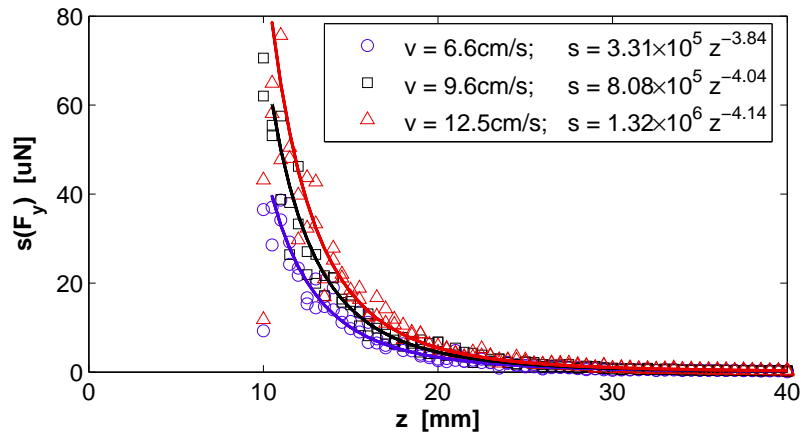
Figure 5.15: Dependence of the spanwise force on the horizontal distance of the magnet center to the inside of the duct wall. Vertical position is at mid-height. (a) Raw force signal (excerpt) at $v = 9.6\,\mathrm{cm/s}$. Magnet is moved closer to the duct in steps of $0.5\,\mathrm{mm}$ after $50\,\mathrm{s}$. The inset shows a raw zero signal with the same settings. Visible steps are parasitic effects from magnetic material nearby the measurement setup. The zero signal is subtracted from the main signal to yield the pure magnetohydrodynamic force. The slight decrease during each step is due to thermal drift. (b) Mean force for different velocities. The trend for higher force closer to the duct is obscured by strong scatter. (c) Standard deviation. Fluctuations clearly increase with decreasing distance according to a power-law, and also increase with increasing velocity. Note that the magnitude of the standard deviation is higher than the force mean by at least a factor of 2.

One raw measurement series is shown in fig. 5.16a, with the red line marking the position of the zero signal for better comparison. In figs. 5.16a and b, one can see that the force mean signal is clearly positive, despite the large fluctuations. The strongest fluctuations coincide with the fastest rotation speeds of the pump, as is shown in fig. 5.16c which depicts the standard deviation. The dependence of the standard deviation on the flow velocity is clearly linear. The mean forces (fig. 5.16b) display a tendency to be higher for faster duct flows, but the trend is somewhat hidden behind the large scatter of the data points. Even more so, the repeatability of the mean forces is rather poor: the data points corresponding to the depicted raw signal are marked with a red rim. Considering the red-rimmed points alone, one can already see a large deviation between the force signal corresponding to an increasing velocity and the force signal corresponding to a decreasing velocity. Taking into account all the black data points that have been recorded with the exact same settings but at a later time, one finds a significant deviation between the forces at the same velocities, which is quite to the contrary of the standard deviation behavior. Note that the measurement time for each data point is at least 5 min to avoid effects purely due to hydrodynamical turbulence.

5.2.2.3 Spanwise position dependence $F_y(y)$

The settings for the spanwise position dependence of the spanwise force component deviate from those of the streamwise force component. Here, the magnet is put at the vertical positions $-22\,\text{mm} \leq y \leq 29\,\text{mm}$ in steps of $3\,\text{mm}$ to allow longer measurements of $200\,\text{s}$ at each point but still have a short enough measurement to not be affected by the non-linearity of the thermal drift. The measurement series is repeated for four different velocities.

One raw signal is presented in fig. 5.17a. During the first $200\,\text{s}$ the motor is at a standstill, where the signal is a flat, straight line. The mid-height of the duct is reached after about $0.7\,\text{h}$, where the signal is noisiest. The spikes that are particularly visible at $t = 7\,\text{min}$, $10\,\text{min}$, $13\,\text{min}$, $17\,\text{min}$ mark the times when the positioning system is active, because during this measurement the sensitive direction of the measurement system coincides with the direction in which the magnet is moved.

Fig. 5.17b shows the mean force extracted from the raw signals for the different velocities. As is typical for the spanwise force, the scatter is high and there is no clear trend visible. Contrarily, the standard deviations in fig. 5.17c follow the clear pattern of parabolic behavior like in the streamwise case, with deviations having a higher magnitudes for higher velocities. Curiously, the maximum of the standard deviations is about half of the maximum values shown in fig. 5.15c. The most probable cause for this is a difference in placement of the magnet, especially since the side wall is not perfectly vertical, and so the magnet has to be placed slightly farther away from the duct to avoid contact with the duct wall at the bottom positions. This shows the necessity of an improvement in the fixture of the duct and in the (absolute) positioning of the magnet.

5.3 Local resolution

The main question of this thesis is, if velocities can be resolved locally with Lorentz Force Velocimetry using a small permanent magnet. Clearly, the small magnet cubes employed are

(a)
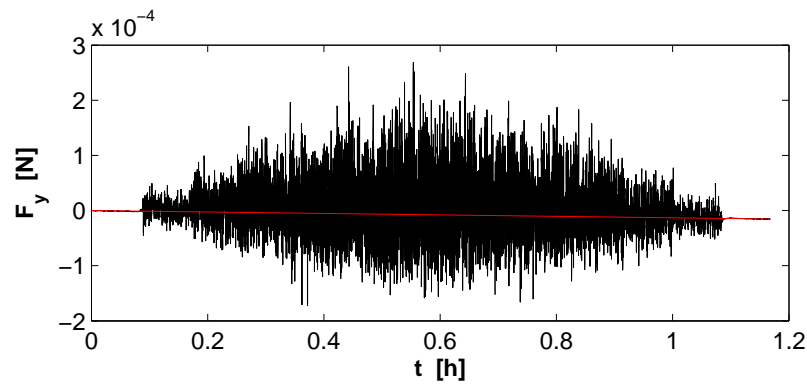
(b)
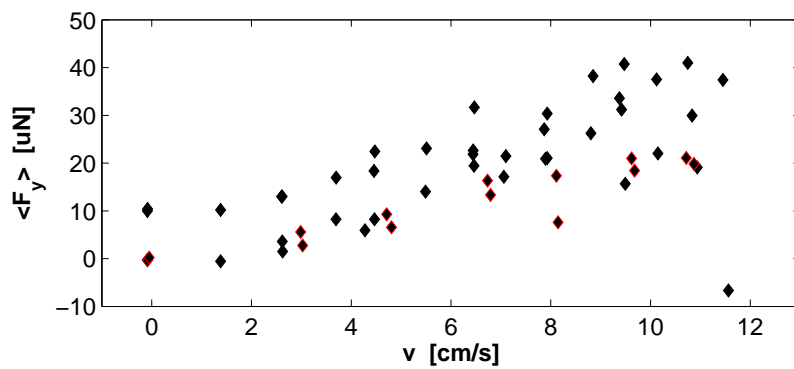
(c)
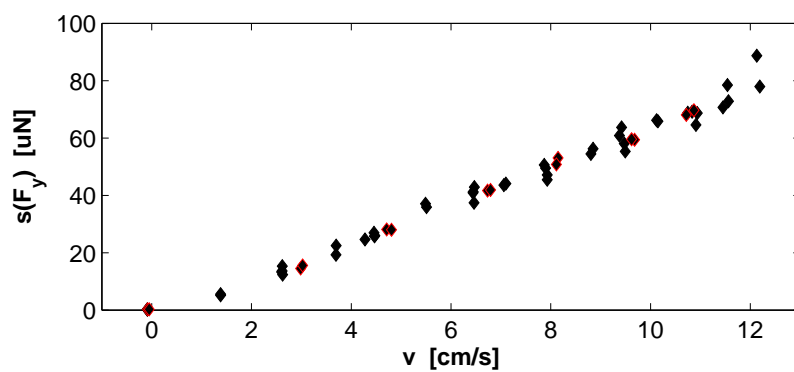
Figure 5.16: Dependence of the spanwise force F_y on the mean flow velocity at mid-height ($y = 0$) and minimum distance ($z = 10$ mm). (a) Raw signal. Red line marks the position of the zero signal that follows a slight but linear drift. (b) Mean force versus velocity. (c) Standard deviation. The red-rimmed points correspond to the data excerpt shown in (a).

(a)
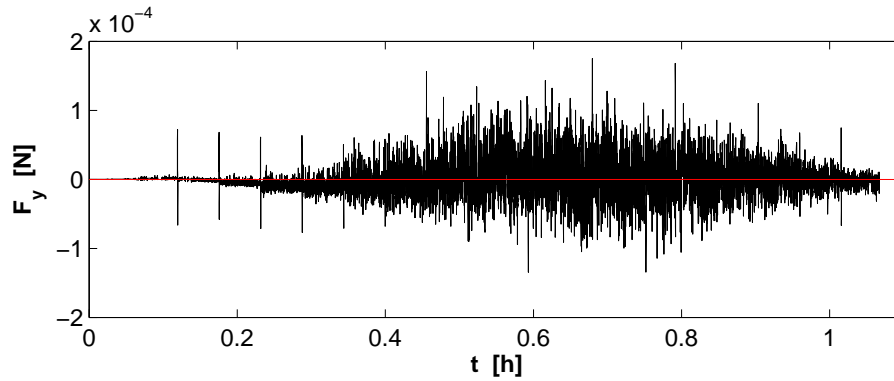
(b)
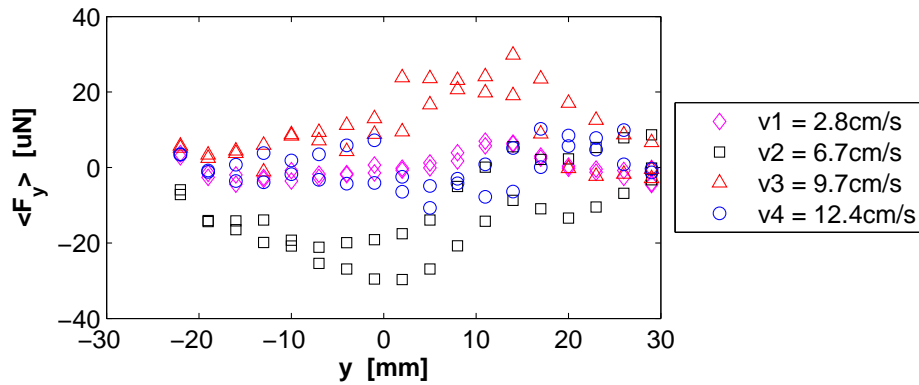
(c)
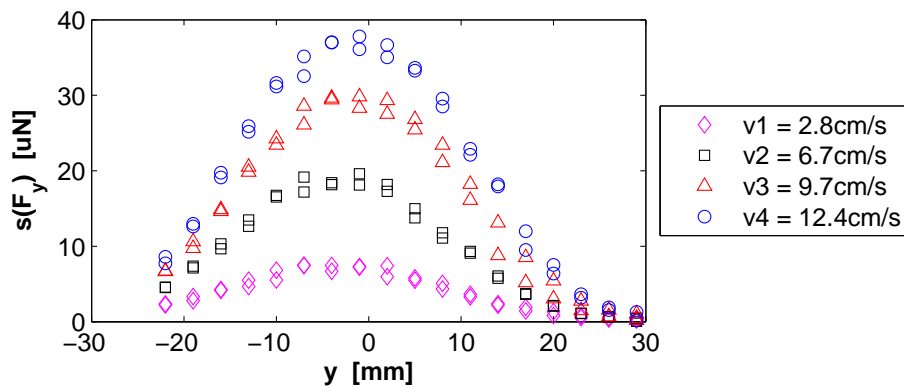
Figure 5.17: Dependence of the spanwise force on the vertical position of the magnet for $z = 10$ mm. (a) Raw signal at $v = 12.4$ cm/s showing the weakness of the mean signal compared to the high fluctuations. (b) Mean forces for different velocities. No clear trend can be observed. (c) Standard deviations. Shape of the curves is identical to that for the streamwise force component (fig. 5.8c), but with a third of the magnitude (at $v = 9.7$ cm/s) and significantly less scatter.

less influenced by the liquid metal flowing at the far side of the duct, but the larger part of the force generated inside the fluid must stem from the vicinity of the magnet. The question addressed in this section is, what distances still belong to this "vicinity" and what distances are far enough away from the magnet so that their contribution to the force can be neglected. Put differently, how large is the fluid "volume of influence" that contributes the lion's share to the total force felt by the magnet?

A first approach to answer this question is a simplified semi-analytical estimate of the volume which is presented in subsection 5.3.1.

The introductory considerations are followed by experimental investigations (section 5.3.2). The experimental data from the liquid metal duct are compared to the experimental data of a related experiment conducted with a solid bar. Besides some minor differences in the experimental setup, the two experiments differ mostly in the velocity profile of the moving object. Therefore, differences in the force profiles may be attributed mainly to the difference in the velocity profiles. Additionally, the turbulent data of section 5.2 is compared to experiments on laminar flows in section 5.3.3. The comparisons will show that LFV with the current setup can distinguish different velocity profiles in moving (liquid) metals.

In a second experiment, a large magnetic obstacle is introduced to the setup: A large magnet is fixed to the bottom of the duct and the resulting force profiles are presented in subsection 5.3.4 along with a comparative measurement of the velocity profile.

Last, a cylindrical object is placed in the middle of the duct, spanning the whole duct width. Even more than the magnetic obstacle, this solid obstacle perturbs the duct flow significantly. Resulting velocity profiles and corresponding force profiles are presented in subsection 5.3.5.

5.3.1 Simulation results

The goal of the following analysis is to determine the fraction of the fluid volume which generates the greater part of the Lorentz force that eventually acts on the magnet. After determining the total force $F_{x,total}$ on the magnet it is therefore necessary to find out inside which radius for example 95% of the total force are generated. The simplified geometry of the volume of influence will be detailed later on.

The semi-analytic estimate for the volume of influence is based on the following simplifying assumptions:

1. The velocity profile is given by a laminar Poiseuille profile between two plane walls, with $\vec{v} = v_x \vec{e}_x$ and $v_x = \nabla p/(2\eta)(2L - z)z$. The side walls of the duct are ignored.

2. The permanent magnetic field $\vec{B}_{PM}$ is composed of a discrete and finite number ($\sim$ 1000) of dipoles with $\vec{B}_{PM} = \sum_{(x,y,z)} \vec{B}_{dipole}$ and

$$B_{dipole,x} = \frac{\mu_0 m}{4\pi} \left[\frac{3\Delta x \Delta z}{r^5} \right],$$

$$B_{dipole,y} = \frac{\mu_0 m}{4\pi} \left[\frac{3\Delta y \Delta z}{r^5} \right],$$

$$B_{dipole,z} = \frac{\mu_0 m}{4\pi} \left[\frac{3(\Delta z)^2}{r^5} - \frac{1}{r^3} \right],$$

where $r = ((\Delta x)^2 + (\Delta y)^2 + (\Delta z)^2)^{1/2}$ with $\Delta x = x - x_{dipole}$, $\Delta y = y - y_{dipole}$, and $\Delta z = z - z_{dipole}$.

3. The flow can be described kinematically and the magnetic Reynolds number Rm is negligibly low, i. e. the magnetic field and the flow field do not mutually influence each other.

The Lorentz force per unit volume is defined as $\vec{F} = \vec{J} \times \vec{B}$ [21]. The electric current $\vec{J}$ can be determined by Ohm's law $\vec{J} = \sigma(\vec{E} + \vec{u} \times \vec{B})$. Although neglecting the electric field $\vec{E}$ can seriously distort the result in some cases [144, 145], the further analysis here is restricted to the second addend $\vec{u} \times \vec{B}$ for simplicity. An analysis with the inclusion of the electric field is beyond the scope of this experimental thesis, but can be performed with large-scale simulations like in [15]. Note that here not the magnitude of the Lorentz force is of interest, but the approximate volume where it is generated. Comparison with one sample RANS simulation at the experimental parameters shows that the volume *size* estimates are similar, in spite of the *shapes* of the volumes deviating significantly [15].

With the above assumptions the simplification leads to the following Lorentz force $F_{x,total}$ on the magnet: $F_{x,total} = -\sigma v_x \left(B_{PM,y}^2 + B_{PM,z}^2 \right) V_{duct}$, with V_{duct} being the volume of the entire duct. Whereas v_x is described analytically by the Poiseuille profile in point 1, there exists no straightforward description of the magnetic field of a magnetic cube. Therefore, $\vec{B}$ is calculated numerically according to point 2.

The numerical magnetic fields can be validated with the magnetic fields of the real magnet cubes. As seen earlier (section 3.5), the magnetic field decays more slowly the larger the magnet is. Fig. 5.18 shows the distance at which the magnetic field of different magnet sizes is decayed to 5% of its maximum value at the surface. The calculated distances show the same trend as the experimental distances. Note however, that the simulations assume a perfect magnet and therefore yield a magnetic field slower-decaying than the naturally imperfect real magnets. From fig. 5.18, a magnetic dipole ($D = 0$) has a decay distance of less than 1 cm, whereas the standard 1 cm cube has a decay distance of 1.9 cm (simulation) or 1.5 cm (measurement).

To find the volume of influence, however, it is necessary to look for where 95 % of the force are generated rather than where the 95 % magnetic field boundary is. For simplicity, let us assume the 95 % volume to be a sphere cap with the center of the sphere coinciding with the center of the magnet. The desired quantity now is the radius r_{95} that defines the 95% volume.

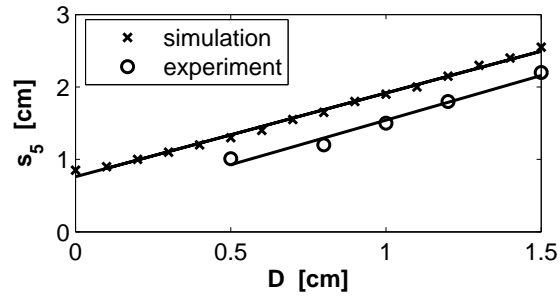The steps that need to be undertaken are:

Figure 5.18: Distance s from the magnet surface at which the magnetic field of different cubes has decayed to 5 % of the value on the magnet surface, i. e. where $B = 5\% \, Bmax$. Simulations yield higher values, because the cubes are assumed to have perfect magnetization.

1. Find the Lorentz force F_{total} generated by the full duct.
2. Find the radius r_{95} that defines a sphere cap inside which 95 % of the total force F_{total} are generated.
3. Compare the radius for different magnet sizes and distances.

Fig. 5.19 shows the simulation results for different magnet sizes D and magnet distances from the duct. Note that not the force itself is given, but the distance into duct inside which 95% of the force are generated. The parameter s denotes the distance of the magnet surface to the duct, thus $s = 0.5$ cm corresponds to the experimentally accessible regime dictated by the 5 mm duct wall. For the 1 cm magnet cube, the 95 % cut-off radius is almost 4.4 cm. This distance is measured from the magnet center, i. e. the volume of influence extends from the inside of the wall 3.4 cm into the duct. The radius increases for larger magnets, but the dependence is weak. Even an ideal magnetic dipole would still penetrate 2.5 cm deep into the flow, if placed outside the same 5 mm duct wall. Only when the duct walls are thin ($s = 0.1$ cm), does a dipole promise to be a significant improvement over the 1 cm cube (1.1 cm penetration depth from the wall versus 2.7 cm).

Similar simulations show that if the cut-off is reduced from 95% to 50%, the influence radius for the 1 cm cube is only 2 cm from the magnet center, corresponding to a penetration depth of 1 cm. That is, half of the force acting on the magnet is generated inside a region extending only 1 cm into the liquid metal flow. All the remaining metal outside the sphere cap, including the metal in the duct center having the highest velocity, contributes to the other half.

5.3.2 Comparison with solid body experiment

An experiment similar to the liquid metal duct flow of this project is performed by R. Uhlig (project C1). Instead of using a metal melt, his object of investigation is a solid aluminum bar, with a cross section of 5 cm by 5 cm and a length of 25 cm. The bar is moved past a small magnet with a speed of 2 m/s (maximum speed is 3.75 m/s). The magnet is placed above the moving specimen and is of cylindrical shape with a typical diameter of 15 mm and a length of 12 mm. The magnet is attached to a 3-component force measurement system. A full description of the setup can be found in R. Uhlig's dissertation [146].
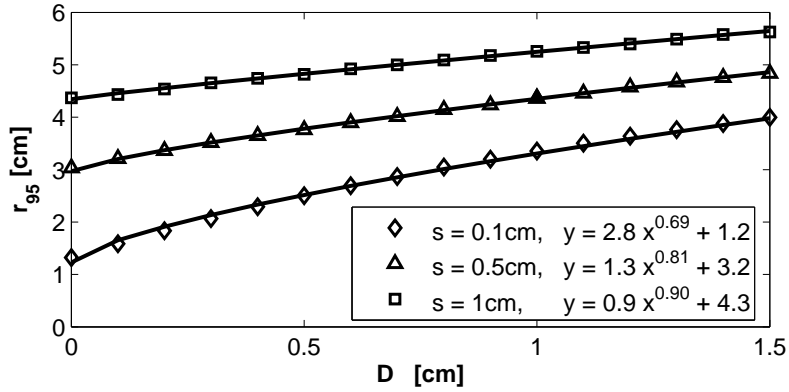
Figure 5.19: Distance r_{95} that defines a sphere cap extending into the liquid metal. Dependence of the magnet size D is shown for three different distances s of the liquid metal from the magnet surface. Center of the sphere coincides with the magnet center. Inside the volume of the sphere cap 95% of the total Lorentz force are generated, $F(r_{95}) = 95\,\%F_{total}$. The parameters of the standard measurement setup are $D = 1\,\text{cm}$ and $s = 0.5\,\text{cm}$, yielding a penetration depth into the liquid metal of $r_{95} - s - D/2 = 3.4\,\text{cm}$ from the inside wall (solid triangle marker).

The results of both setups cannot be compared directly, as their parameters differ considerably. For example, the solid bar moves at $2\,\text{m/s}$, whereas the mean velocity of the liquid metal is $9.5\,\text{cm/s}$. The magnets of the two setups are of different shape and size. The aluminum bar has an approximately three times higher electrical conductivity than the liquid metal. With these settings, the streamwise force component for the solid bar is around $570\,\text{mN}$ and the spanwise force component is around $20\,\text{mN}$. For comparison, the liquid metal setup gives forces around $1\,\text{mN}$ and $30\,\text{uN}$, respectively. In both cases, however, the spanwise force component is on the edge of measurement system resolution.

For the streamwise components, the force profiles can be compared when the forces are normalized with their respective maximum (see fig. 5.20). The upper figure (5.20a) displays the two profiles of the force component F_x across the height of the duct, i.e. along y; the lower figure (5.20b) shows the two force profiles along the z-direction for the two experimental setups. A comparison of the spanwise force components has been omitted due to the high scatter in the liquid metal experiments.

The solid body measurements have been recorded only for the half-width of the duct as they are symmetric about the origin. To be consistent with the previously shown y-profiles, the data has been duplicated onto the other half of the bar. Therefore, the solid bar data to the left of the origin in fig. 5.20a is identical to the data to the right. The liquid metal measurements are plotted only once.

Closely comparing the drag forces for the two setups, one can see a slight difference between the two. The solid bar forces coincide with the liquid metal forces between $-20\,\text{mm}$ and $20\,\text{mm}$, but they are larger than the liquid metal forces around the upper edge region at $y = 25\,\text{mm}$ by up to around $50\,\%$.

A comparative velocity measurement has been performed with a UDV probe (see section 3.6.2). The color coded velocity profile for a standard measurement at $9.6\,\text{cm/s}$ mean velocity is shown in fig. 5.21. It should be mentioned here that there is a notable discrepancy

(a)
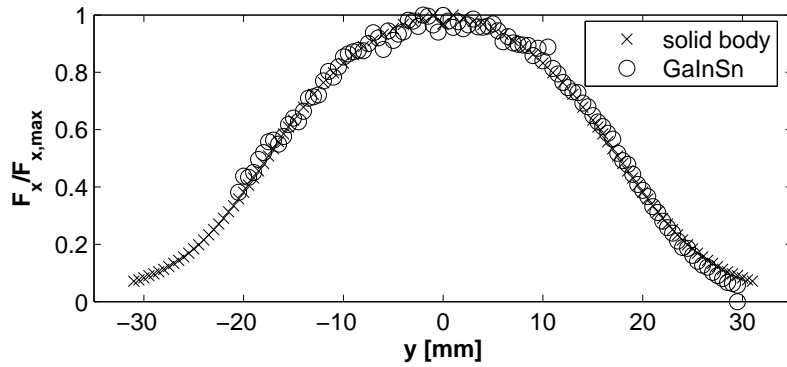
(b)
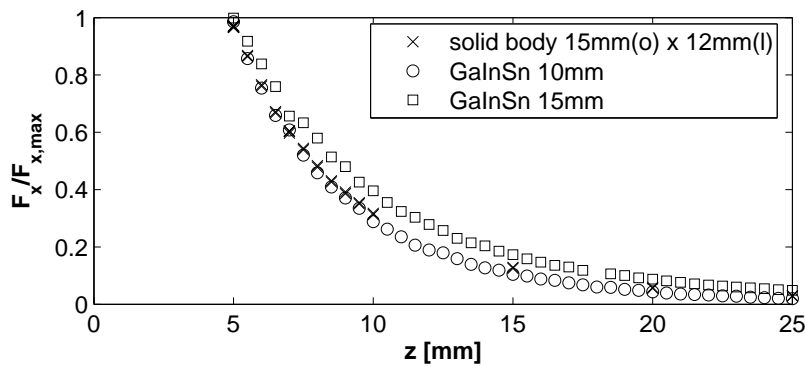
Figure 5.20: (a) Comparison of experimental data for the liquid metal duct with the solid bar experiment. (a) Drag force F_x for the two setups in dependence on the spanwise position of the magnet. Forces are normalized with the respective maximum of the profile, as the solid bar setup produces forces higher by a factor of 10^2. The two force profiles lie on top of each other except for the upper edge region of the duct. (b) Comparison of the z-profiles of the normalized force component F_x. The solid bar forces are generated with a cylindrical magnet that is intermediate in size between the smaller 10 mm cube and the larger 15 mm cube, consequently resulting in a force profile lying in between the force profile produced with the two cubes (cf. fig. 5.10b). Solid bar data is provided by R. Uhlig.
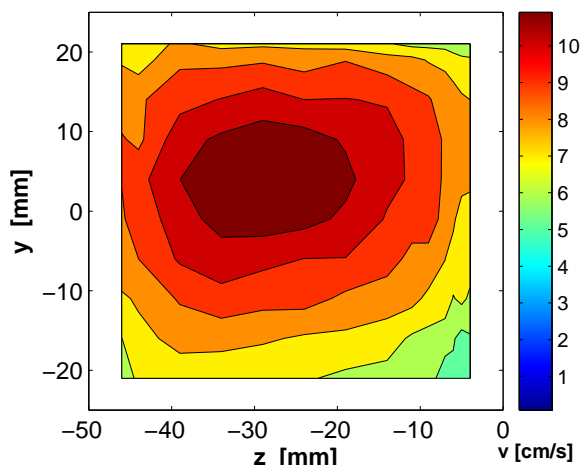
Figure 5.21: Velocity profile measured with the UDV-probe. The slightly off-center maximum of the flow velocity is probably caused by the highly uncontrolled inlet conditions.

between the mean velocity determined by the flow meter (9.6 cm/s) and the integral of the UDV velocity over the whole measured cross section (9.0 cm/s). For consistency, the mean velocity will continue to be determined from the volume flow. Fig. 5.21 shows a slight asymmetry in the velocity profile that is most likely due to the highly irregular inlet conditions (a bend shortly before the test section, the bellow and then the diffusor). Still, the measurement confirms the assumption of the flow profile being turbulent, with a sharp decrease in velocity towards the edges.

Now, probing with the magnet along the vertical side of the turbulent duct flow, it seems that the magnet "sees" a velocity around the average velocity as long as $y < 20$ mm, but mostly sees the slower boundary layer as soon as the magnet is starting to leave the metal region at $y > 20$ mm.

Fig. 5.20b depicts the z-profiles of the streamwise force components of the two experiments. All z-profiles are taken at the centerline or mid-height of the duct/bar. For comparison, drag force profiles of the liquid metal are displayed that have been generated using the standard 10 mm magnet and the 15 mm magnet, respectively. The difference in magnet size is visible in the different decay slopes, as was seen in fig. 5.10. Since the cylindrical magnet is in between the 10 mm and the 15 mm cube, the forces it generates lie between the forces of the two cubes. Apart from that, no difference in the solid bar and liquid metal force profiles can be detected.

5.3.3 Turbulent and laminar profile

So far, all liquid metal experiments have been performed at typical flow velocities of several cm per second, equivalent to Reynolds numbers of several thousands and thus well in the turbulent regime. This section explores the laminar regime with low fluid velocities. The two test velocities are 0.64 cm/s and 1.0 cm/s, corresponding to Reynolds numbers of 470 and 750, respectively. Note that the flow is not experimentally proven but rather assumed to be laminar based on the argumentation in section 2.1.1.

(a)
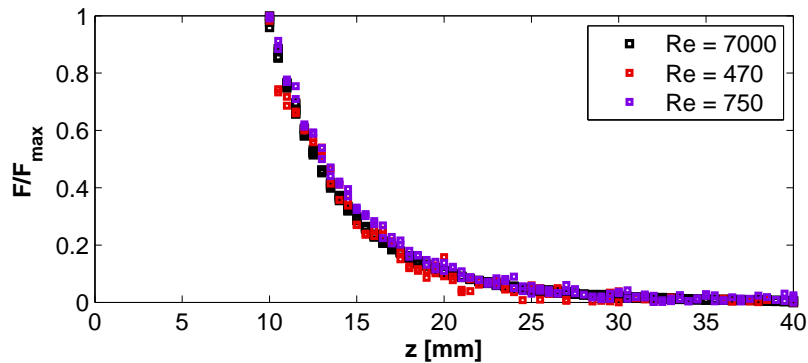
(b)
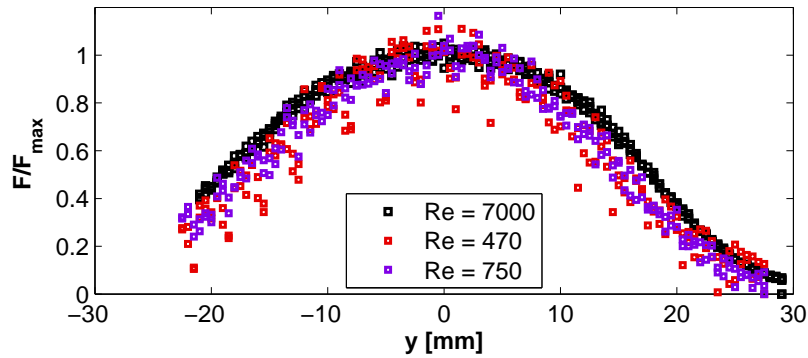
(c)
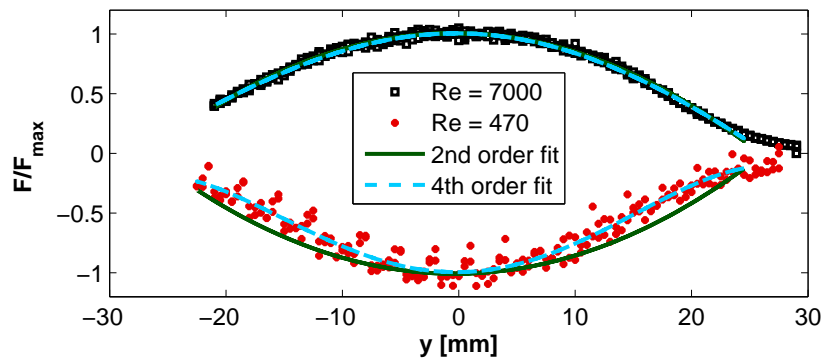
Figure 5.22: Comparison of the streamwise force profiles along z and y. Forces are normalized not with the maximum force itself but the mean of the forces measured at $y = 0$ to account for the relatively large scatter. (a) Distance dependence. Force profiles for laminar flow and turbulent flow coincide. (b) Spanwise position dependence. The laminar profile deviates significantly from the turbulent profile, indicating a slower increase of the velocity from the boundary toward the bulk flow. (c) Turbulent and one laminar profile along y. Same data as in (b). The turbulent data points are fitted with both a parabola (red) and a 4th order polynomial (blue). Both fits coincide. The laminar data (flipped below the x-axis for better visibility) is also fitted with a parabola and a 4th order polynomial. However, unlike for the turbulent data, the parabola clearly deviates from the laminar data and the 4th order fit. Therefore, the laminar profile can easily be distinguished from the turbulent profile by the shape of their fit functions.

In fig. 5.22, the z- and y-profiles of the streamwise force components of the laminar flow experiments are compared to that of the turbulent standard experiment ($Re = 7000$). Since the forces generated by the turbulent flow are considerably higher than for the laminar flow, all force profiles are normalized. Unlike before, however, not the global maximum of the force has been used for normalization, because the scatter of the laminar data is too large. Rather, the average of the forces at $y = 0$ has been used. The difference is marginal, but this procedure avoids normalizing with an outlier like that in fig. 5.22b.

The distance dependences (fig. 5.22a) are virtually identical, that is no difference can be detected between the forces from the laminar flows and turbulent flow. The spanwise force profiles (fig. 5.22b), however, do show a difference. Sharing the same maximum, the laminar profiles are lower than the turbulent profile outside the 20 mm wide center region by up to around 25 %. This is likely to be due to the lower velocities in the wall vicinity relative to the respective maximum velocity.

Moreover, laminar and turbulent force profiles can be distinguished without having the respective other for comparison, as fig. 5.22c shows: Whereas the turbulent data can be well fitted with a parabola, the shape of the laminar data deviates significantly from such a curve and must be fitted with a 4th order polynomial to obtain a reasonable agreement (see caption to fig. 5.22c for details).

5.3.4 Magnetic obstacle

Instead of solely changing the slope of the velocity profile, this and the following subsection impose an asymmetry on the flow. As has been explained in section 2.2.4, a magnet acts as an obstacle to a liquid metal duct flow forcing the metal to flow around it. In the duct experiment, the easiest way to introduce such a magnetic obstacle is to place a large magnet at the bottom. The magnet chosen is 6 cm wide spanning exactly across the outside of the bottom wall, 2 cm high (see figs. 5.23 and 5.24) and extends 3 cm in flow direction. The magnet is placed 17 cm before the measurement magnet (fig. 5.25a). On the surface, the maximum of the magnetic flux density is 504 mT in one of the corners of the magnet. The maximum flux density inside the duct is 355 mT at the bottom wall. The magnetic field distribution inside the duct is displayed in fig. 5.23. There, it can be seen that the magnetic field is decayed to 50 % of its maximum at around $y = -15$ mm.

As a result, the liquid metal flow is pushed upward to have its maximum flow velocity around $y = +15$ mm and $z = 0$ (fig. 5.24a). The velocity field shown is obtained with a UDV probe. The magnitude of the maximum velocity is 12 cm/s; in the standard profile, the maximum is 11 cm/s and located at $y = 5$ mm and $z = -30$ mm (fig. 5.21).

A scan of the force with the small magnet is naturally affected by the strong magnet in the vicinity. Thus, the force signal of the vertical scan at 9.6 cm/s is a superposition of the zero signal with still motor that stems from the relative position of the two magnets (not shown) and the actual, magnetohydrodynamic force. Subtracting the zero signal from the total force yields a mean force profile (fig. 5.25b) whose maximum is clearly off-center at $y = 5$ mm. The shape of the profile deviates from a parabola with a steeper slope on the right side (upper half of the duct) and a gentler slope on the left (bottom half); a reasonably good fit is found
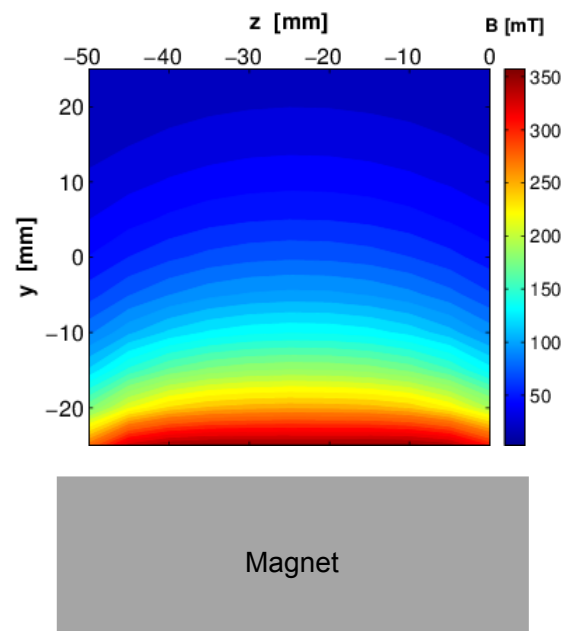
Figure 5.23: Magnetic flux density distribution B_z inside the liquid metal realm. Positioning steps with the Hall probe are 5 mm in both y and z. Profile is taken directly above the centerline of the magnetic obstacle (grey, to scale). The magnet is as wide as the duct, and therefore wider than the liquid metal region.

(a)   **(b)**
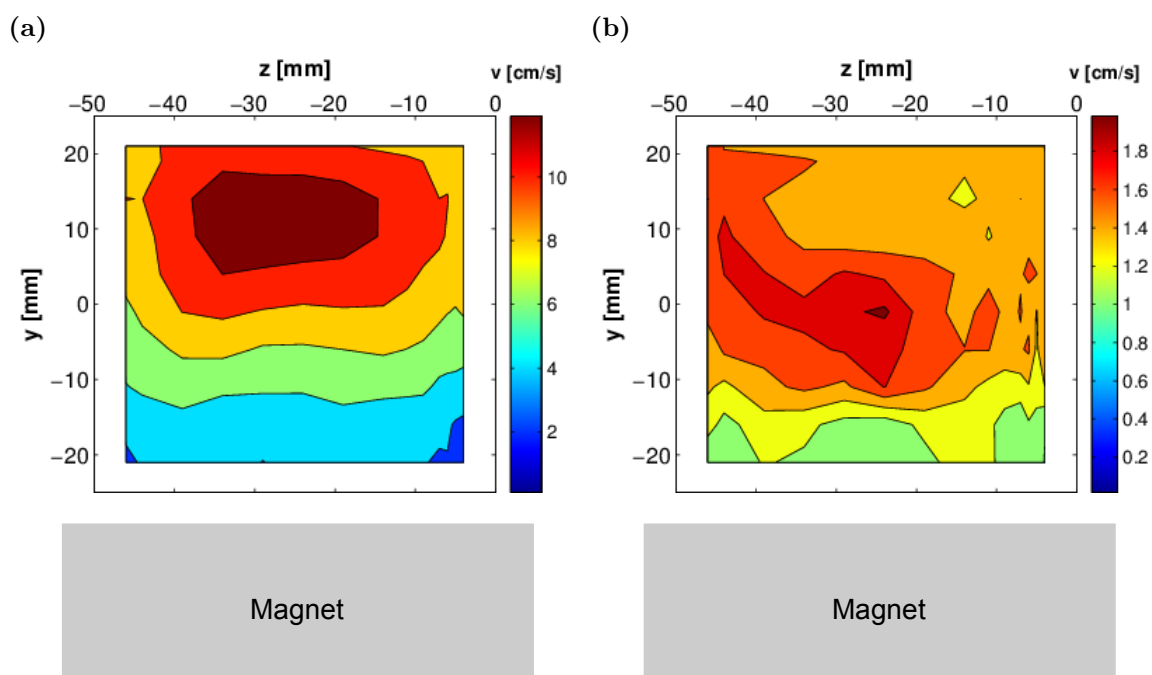
Figure 5.24: Velocity field measured with the UDV probe 17 cm downstream of the magnetic obstacle (grey). The magnet is drawn in a lighter shade to demonstrate that the velocity profile is recorded *not* directly above the magnet, but at the x-position of the small measurement magnet (also see fig. 5.25a). (a) Mean velocity field inside the duct. (b) Standard deviation of the velocity field.

in a 5th order polynomial ($R^2 = 99.57\%$). Curiously, the shape of the standard deviation profile remains unchanged in symmetry and still follows the parabolic profile (fig. 5.25c).

In fig. 5.25, both the mean force profile and standard deviation profile for the standard unperturbed flow are are for comparison. The maximum of the force along the side of the duct is 958 uN for the unperturbed flow, as opposed to a slightly lower maximum of 875 uN for the perturbed flow. The difference in standard deviation is bigger: $s(F_x)_{max}$ is 102 uN for the unhindered flow and 75 uN for the obstructed flow. Note that the difference in the force mean could be explained by a possible difference in placement of the magnet by 0.5 mm, whereas the difference in the standard deviation is significantly larger than a reasonable misplacement could explain. Clearly, the large magnet in the vicinity of the metal is damping the fluctuations in the flow. This is supported the UDV standard deviation profile in fig. 5.24b: A 5 mm wide area is visible directly above the magnet where the standard deviation is significantly lower than elsewhere (green areas).

Moreover, the different shapes for the force and standard deviation profiles indicate that the high fluctuation are not directly related to the higher force itself, i. e. the fluctuations are not merely an artefact of the stronger force on the magnet.

5.3.5 Solid obstacle

A different way to change the flow profile is the use of a solid obstacle, an obstacle that is placed in the middle of the duct and separates the metal flow into two distinct jets. If LFV is capable of localized measurements, then this is the test – it must be able to distinguish the two jets.

The obstacle is a cylinder with a diameter of 13 mm that is placed with its axis at $y = 2.5$ mm. Being 50 mm long, it spans over the entire width of the duct. In streamwise direction, the cylinder is placed roughly in the middle of the duct. The mean flow velocity is 9.3 cm/s. The velocity difference to earlier measurements is most likely caused by the high uncertainty of the reference flow meter, or the uncertainty in pump speed (input is 50 rpm as usual).

Velocity profiles are recorded at different x-positions, ranging from directly where the cylinder is to 5 cm behind the cylinder (see fig. 5.26). Force profiles are recorded at the same positions, and the resulting force profiles across the height of the duct are shown in fig. 5.27. The left column of fig. 5.27 depicts the mean forces F_x, and the right column displays the corresponding standard deviations $s(F_x)$. The expected two jets above and below the cylinder appear as two bumps in the mean force profile with a dip where the cylinder is located, the local minimum of the dip being at $y = 2$ mm.

From the larger left peak in the force profile (e.g. fig. 5.27a) it can be inferred that the lower of the two jets is faster. The UDV reference measurement (e.g. fig. 5.26a) confirms this assumption. The dip in fig. 5.27a becomes less pronounced when the distance of the magnet to the cylinder is increased, its magnitude rises from 404 uN (0 cm) to 453 uN (1 cm) and to 619 uN (2 cm), until it reaches the plateau at around 1000 uN (5 cm). The left peak has its maximum at 1 cm behind the duct, changing its magnitude from 959 uN (0 cm) over 1095 uN (1 cm and 2 cm) to 1000 uN (5 cm). The right peak shows a steady increase from 781 uN (0 cm) to 967 uN (1 cm) and 990 uN (2 cm and 5 cm).

(a)

(b)

(c)
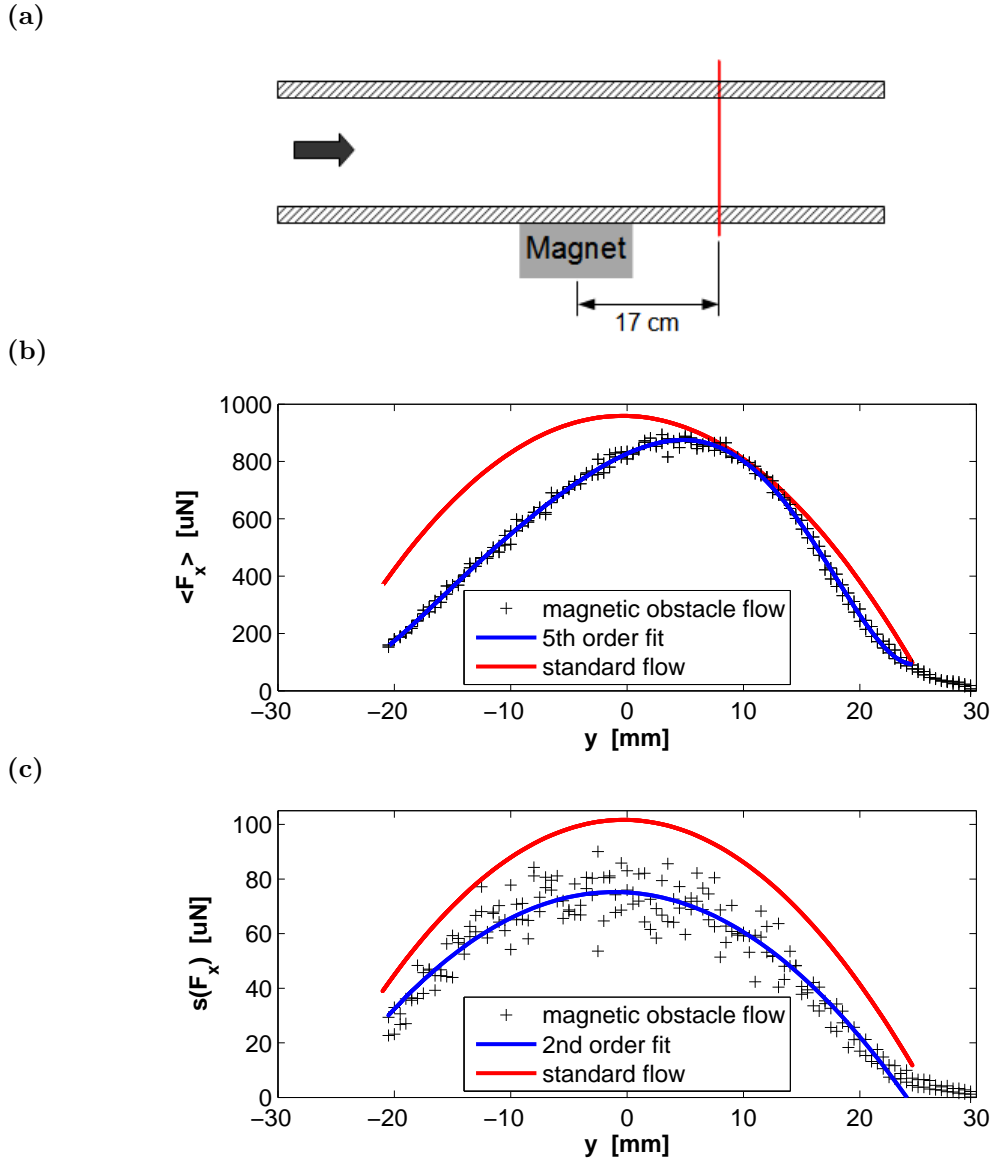
Figure 5.25: Spanwise position dependence of the force (F_x) and standard deviation ($s(F_x)$) when the flow is perturbed by a magnetic obstacle below the bottom duct wall. Average flow velocity is $9.4\,\text{cm/s}$. (a) Position of the magnetic obstacle before the measurement system (not to scale). The magnet is marked by the grey box directly below the bottom wall of the duct; the vertical red line marks both the position of the force-profile along y and of the UDV profile shown in fig. 5.24. (b) Dependence of the mean force. The force profile is shifted upward (in the positive y-direction), losing its parabolic shape. The parabolic fit (red line) of the standard profile is shown for comparison. The exact fit for the blue line is $F = 8.48\times10^{-5}y^5 + 4.24\times10^{-4}y^4 - 0.0760y^3 - 1.71y^2 + 19.58y + 834.1$ with $R^2 = 99.57\,\%$. (c) Dependence of the standard deviation. Unlike the mean force, the profile retains its parabolic shape, with its symmetry about the mid-height of the duct. The red line shows the standard profile; the maximum of $s(F_x)$ is significantly lower for the obstructed flow.
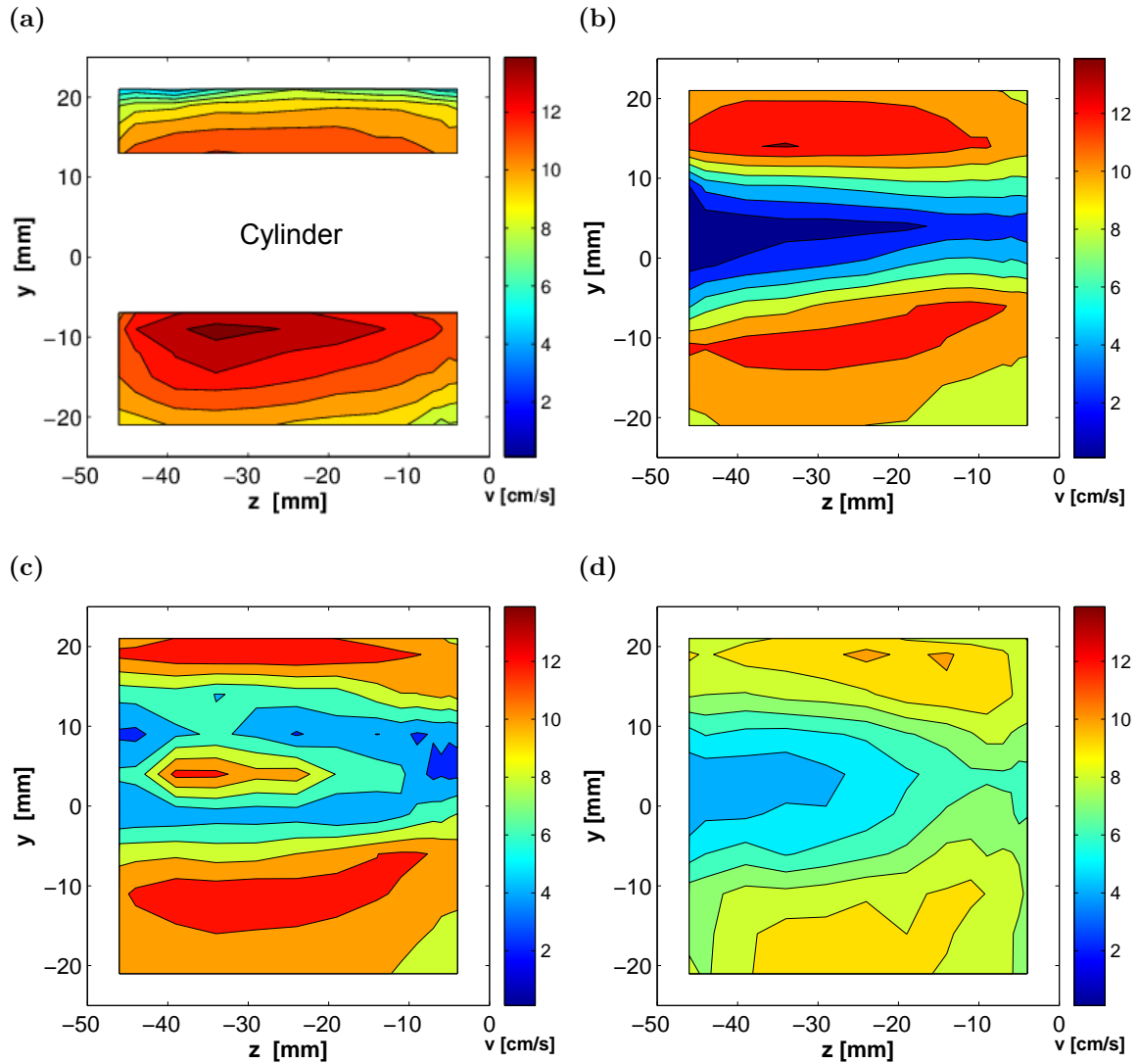
Figure 5.26: Reference measurement of the velocity profile with the UDV probe. Average velocity is $v = 9.3$ cm/s. (a) Profile taken at $x = 0$. The white area in the center marks the position of the cylinder, plus twice the radius of the UDV probe (4 mm). (b-d) Profiles at $x = 1, 2, 5$ cm.
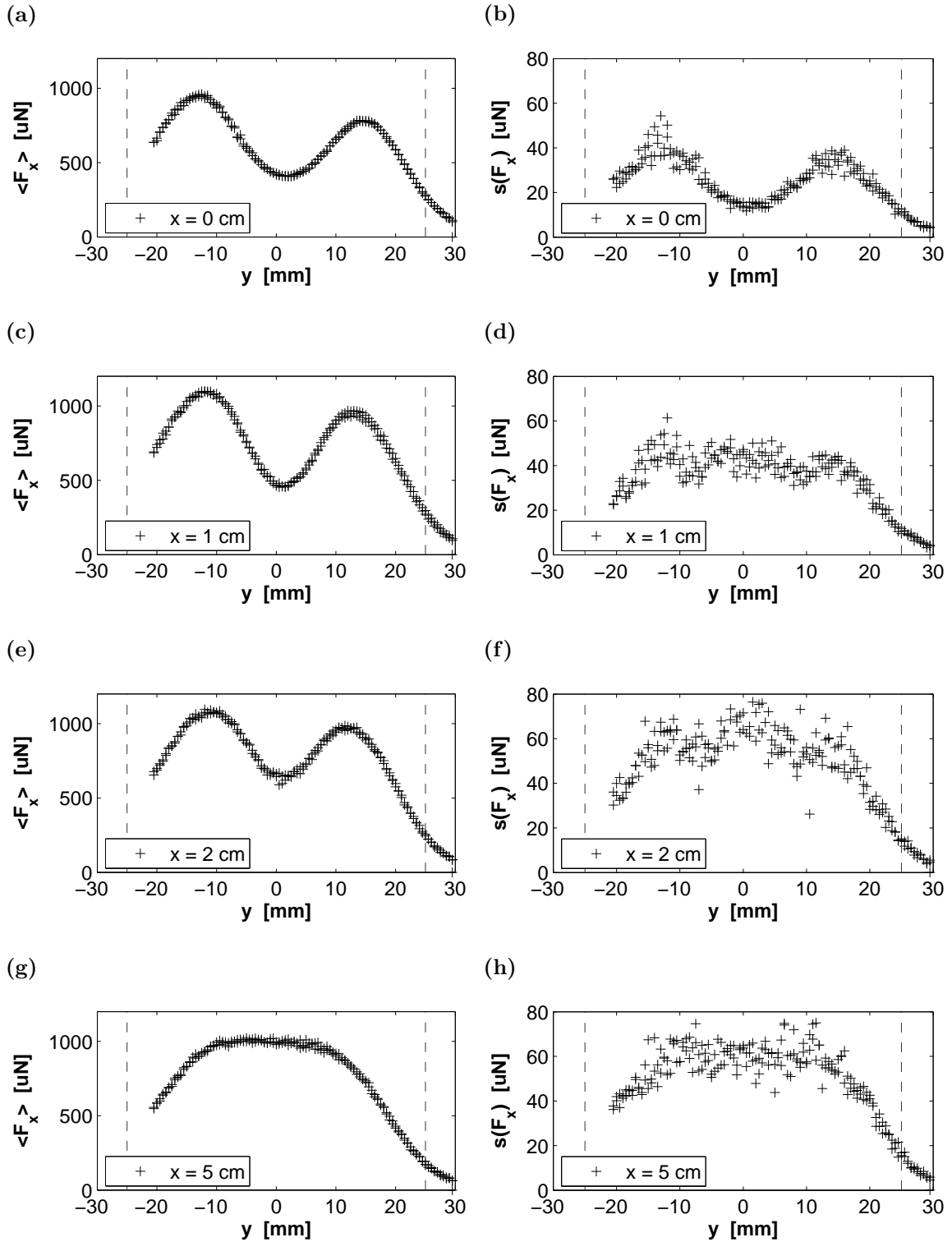
Figure 5.27: Dependence of the force profile on the vertical magnet position when the flow is obstructed by a solid cylindrical obstacle. The measurement system is placed at different streamwise positions behind the cylindrical obstacle. Distance from the duct is $z = 10\,\text{mm}$ and average velocity is $v = 9.3\,\text{cm/s}$. (a,c,e,g) Mean force profile at the denoted streamwise positions. (b,d,f,h) Standard deviations at the same x-positions. Dashed lines mark the upper and lower edges of the duct, respectively.

The increase in the left (i. e. lower) peak is contradicted by the velocity profile (fig. 5.26b), that clearly shows a smaller velocity at 1 cm behind the cylinder. Generally, it appears that the area under the force profile increases with increasing distance (by 23 %), seemingly hinting at an increasing volume flux past the measurement magnet. Note, however, that the reference velocity measurement rather suggests that the velocity distribution across z is shifting towards the right, i. e. towards the magnet from fig. 5.26a-d.

A discussion of the standard deviation of the force is omitted here, as it will be part of the following section (5.4).

5.4 Temporal resolution

So far, the focus was on the behavior of the mean force and the standard deviation of the force signal was largely neglected in the discussion. While most of the standard deviation can be explained by duct vibrations, there is indeed evidence that the local LFF can resolve turbulent fluctuations inside the metal flow at maximum frequencies of 6.3 Hz.

First, let us re-collect the evidence for the influence of the vibrations on the flow: As early as in the frequency analysis in section 5.1, an agreement was found between the vibrations the duct undergoes and the frequencies in the force signal. The coinciding vibrations depend on the speed at which the pump is turning.

According to fig. 5.7, the standard deviation representing the signal fluctuations decays at the same rate as the mean force – and is always one tenth of the mean force. The ratio of standard deviation and mean force is constant across the height of the duct and for all velocities. This indicates that the force fluctuations are merely reflecting the duct vibrations.

Unlike $< F_y >$, which is drastically lower than $< F_x >$, the standard deviation of F_y is practically as high as that of F_x (see figs. 5.17 and 5.8). Remember that the pump dependent duct vibrations were found in both horizontal directions, therefore it is reasonable to assume that the duct also vibrates in the vertical direction and that the measurement magnet picks up these tiny displacements of the liquid metal. The maximum at $y = 0$ then simply stems from the fact that the magnetic field is surrounded by a maximum volume of liquid metal at that position.

Alternatively, the force fluctuations could stem from turbulent fluctuations inside the fluid flow. Unfortunately, the standard deviation of the laminar velocity profiles has the same shape as that of the turbulent velocity profiles (not shown).

The magnetic obstacle changes the profile of the mean force but leaves the profile of its standard deviation unaltered (fig. 5.25). On the other hand, fig. 5.24 reveals that the metal flow is indeed fluctuating most strongly in the center of the duct, although the maximum of the flow is shifted upwards.

So far, the evidence clearly points towards the LFF resolving the duct vibrations originating from the discrete pulses of the electromagnetic pump.

Now, the standard deviation profile directly at the cylindrical obstacle (fig. 5.27b) could still be explained by vibrations, because the local minimum of the profile coincides with the metal-free region. The wake behind the cylinder, however, cannot be purely due to duct vibrations, because otherwise the profiles d, f, and h of fig. 5.27 should look like that in

(b)

(a)
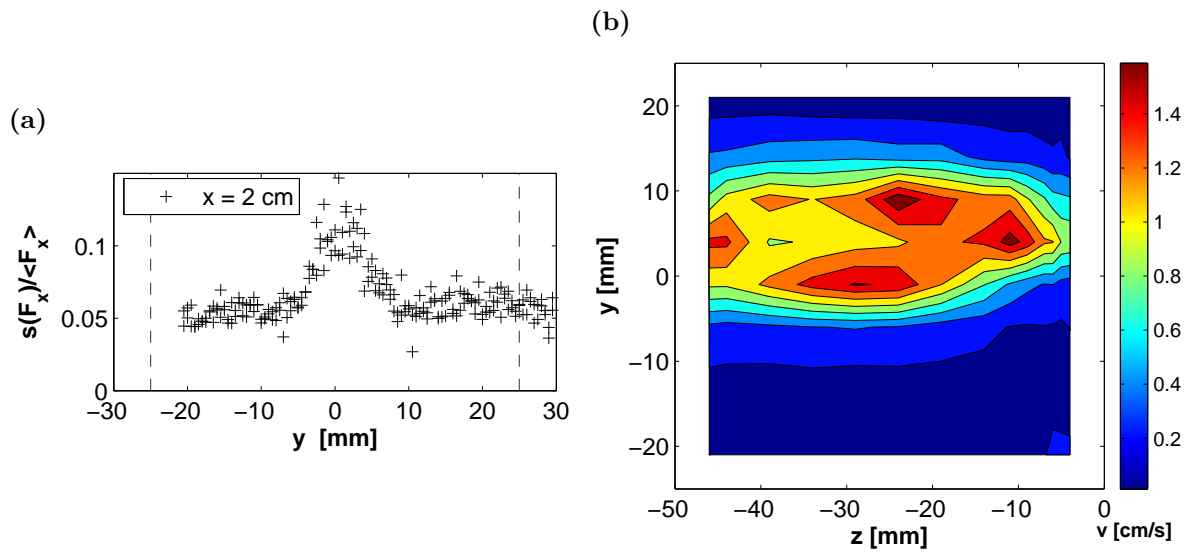
Figure 5.28: (a) Ratio of standard deviation to mean force for the force profile taken 2 cm downstream of the cylindrical obstacle (also see fig. 5.27c and d). The peak at $y = 0$ coincides with the highly turbulent wake of the cylinder. (b) Ratio of standard deviation to mean force for the velocity profile measured with the UDV probe. The turbulent wake at mid-height of the duct clearly stands out.

fig. 5.8c. Rather, the deviation of the three profiles from the expected two-peaked profile is the development of a third peak in the middle between the two peaks from the jets, which coincides with the highly turbulent wake of the cylinder (cf. section 2.1.3). To make this clear, the ratio of the standard deviation and the mean force is shown in fig. 5.28a for the profile at 2 cm downstream of the cylinder. The ratio is constant for most y, although much lower than for the standard profile (cf. fig. 5.7d), but has a marked peak around $y = 0$.

Fig. 5.28b shows the UDV profile at the same x-position as the force profile. Unlike before, in fig. 5.28b the ratio of the standard deviation to the mean velocity at each data point is depicted. The peak at $y = 0$ in the force profile is matched in the UDV profile with a strong increase in velocity fluctuations at the same height. Consequently, it is possible to not only resolve turbulent fluctuations, but to detect regions of increased turbulence with the local LFF despite the high noise level of the duct vibrations.

5.5 Summary

This chapter presented the experimental results of the new measurement setup. The experimental investigation covered four main areas: the characterization of the measurement system, the collection of standard reference data of the unperturbed duct flow, and investigations of perturbed duct flows that allowed to draw conclusions on the spatial and temporal resolution of the measurement system.

In the first section it was found that the force signal changes when the ambient temperature changes, and for a few hours each the drift is linear. Within one measurement series, the streamwise force is repeatable to within 2%, and the spanwise force to within 15% of the

mean value. The uncertainty in force measurement is significantly higher (up to 20%) for different measurement series.

Empirical laws for the dependence of the streamwise force component were determined for the four independent parameters z, y, v, and D:

$$F_x(z) = 7489 \, z_{[mm]}^{-3.80}$$

$$(y = 0, \; v = 9.6 \, \text{cm/s}, \; D = 10 \, \text{mm}, \; \text{fig. 5.7}),$$

$$F_x(y) = -1.409 \times 10^{-3} \, y_{[mm]}^2 + 0.256 \times 10^{-3} \, y_{[mm]} + 0.966$$

$$(z = 10 \, \text{mm}, \; v = 9.6 \, \text{cm/s}, \; D = 10 \, \text{mm}, \; \text{fig. 5.8}),$$

$$F_x(v) = 0.125 \, v_{[cm/s]} - 0.055$$

$$(z = 10 \, \text{mm}, \; y = 0, \; D = 10 \, \text{mm}, \; \text{fig. 5.9}), \; \text{and}$$

$$F_x(D) = 7.39 \times 10^{-7} \, D_{[mm]}^5$$

$$(s = 5 \, \text{mm}, \; y = 0, \; v = 9.6 \, \text{cm/s}, \; \text{fig. 5.12}).$$

The spanwise force is too scattered to allow for a reasonable fit. In both force directions, the standard deviation exhibits a clear dependence on z, y, and v similar to the streamwise mean force but at a lower magnitude.

Comparisons of the standard profile to different velocity profiles yielded that the local LFF is capable of distinguishing laminar from turbulent flows as well as from solid body movements. Moreover, perturbations to the flow caused by either a magnetic or a solid obstacle could be detected with a resolution of at least 3 cm.

The temporal resolution of the force measurement system is high enough to pick up the vibrations of the duct that are caused by the electromagnetic pump. Moreover, the system could be shown to detect regions of high turbulence fluctuations.

6 Conclusion and Outlook

This thesis is devoted to the investigation of the capabilities and applicabilities of local Lorentz Force Velocimetry. Previously, the principle of "standard" LFV has been studied extensively and has been found to be a viable technique for the measurement of mean flow velocities of materials that are inaccessible to other flow measurement techniques. However, the desire to resolve velocities locally has not been satisfied so far, although it arises in many laboratory and industrial applications.

In this thesis, local resolution is reached with a Lorentz Force Flow meter by implementing a permanent magnet whose dimensions are significantly smaller than that of the flow under investigation. The aim of this thesis is to substantiate the claim of locality, because unlike the usual tangibly or at least visibly bounded sensors for local velocities, the field of the permanent magnet of the LFF generally extends into infinity.

Throughout the work presented, a number of liquid metal experiments have been designed, built, and conducted. A first preliminary duct experiment was carried out to prove that the tiny forces of local LFV could be detected. Despite deficiencies in the original setup, the strain gauges that were implemented provided a force signal of considerable magnitude, and the experimental results could be used for the design of an improved setup.

The main work was performed on a square duct with a high-precision interferometric force measurement system. After an elaborate physical characterization of the measurement system itself, valuable experimental data were obtained on the force profiles of the unperturbed metal flow for different parameters. The data is now used for the validation of related numerical simulations. More importantly, a few modifications to the flow profile helped quantify the volume of liquid metal principally contributing to the force on the magnet.

With the help of these modifications it was found that the local LFF is capable of distinguishing a laminar flow from a turbulent flow, to locate the maximum of the mean flow, and detect obstructions to the flow. Although the force signal is always a superposition of force signals from different areas of the metal flow, it was possible to clearly distinguish two jets that were apart by only three times the edge length of the employed magnet, namely 3 cm.

In addition, it was found that the local LFF can be utilized for time-resolved flow measurements. The turbulent fluctuations of the liquid metal duct flow are directly reflected in the variations of the force signal. Therefore, it is possible to not only identify a turbulent flow, but also to find regions of particularly high turbulence and vortex shedding, like they can be found downstream of flow obstacles.

These traits of the local LFF are relevant for various liquid metal applications, one of them being the identification of nucleation sites of pipe clogging. A growing deposit on a pipe wall will leave a clear mark on the force profile, both by damping the highly distance-dependent force signal and by altering the shapes of the velocity and force profiles. More directly, local

LFV opens the possibility to detect and investigate design flaws like sharp corners and bends of existing setups without the detour of building an extra water model.

Further applications are possible, although with the disadvantage that the local LFF is (still) a rather bulky measurement system that is highly susceptible to environmental influences. Another drawback is the high sensitivity of the system to the distance to the duct, but this can (and should) be solved by adding a distance sensor to the measurement system.

Once both problems are solved and application to high-temperature melts is desired, a cooling system should be added to protect the sensor, the magnet, and the electronics of the system from the heat. Presumably reducing the size of the magnet does not increase the spatial resolution of the sensor significantly, however, the author believes that the 3 cm found earlier are an upper limit and that the resolution that can be achieved with the 1 cm magnet is indeed much better. Ultimately, to make the local LFF a "real" velocity sensor, the measurement method should be accompanied by a computation of the velocity profile from the measured force profile – a task beyond the scope of an experiment.

A Parameters

Parameter	Definition/Range		Meaning
Fixed input parameters			
σ	$=$	$3.46 \times 10^6\,\mathrm{S/m}$	Electrical conductivity of GaInSn
ρ	$=$	$6.36 \times 10^3\,\mathrm{kg/m^3}$	Density of GaInSn
ν	$=$	$3.4 \times 10^{-7}\,\mathrm{m^2/s}$	Kinematic viscosity of GaInSn
L	$=$	$1\,\mathrm{cm},\ 2.5\,\mathrm{cm}$	Characteristic length/duct half-height (old, new)
w	$=$	$8\,\mathrm{mm},\ 5\,\mathrm{mm}$	Wall thickness of the duct
Variable input parameters			
z	$=$	$1.3\,\mathrm{cm}\ldots 6.8\,\mathrm{cm},$ $0.75\,\mathrm{cm}\ldots 5.25\,\mathrm{cm}$	Distance of magnet to the liquid metal
y	$=$	$-4.35\,\mathrm{cm}\ldots 4.35\,\mathrm{cm},$ $-2.1\,\mathrm{cm}\ldots 3.0\,\mathrm{cm}$	Spanwise position of the magnet
D	$=$	$0.5\,\mathrm{cm}\ldots 2.0\,\mathrm{cm}$	Edge length of magnet cube
Q	$=$	$0\ldots 0.34\,\mathrm{l/s}$	Volume flux of liquid metal
v	$=$	$Q/(4L^2)$	
	$=$	$0\ldots 13.6\,\mathrm{cm/s}$	Average velocity
B_0	$=$	$1\,\mathrm{mT}\ldots 270\,\mathrm{mT}$	Maximum flux density at $x = y = z = 0$
Output parameters			
F_x	$=$	$0\ldots 10\,\mathrm{mN}$	Streamwise force component (horizontal)
F_y	$=$	$0\ldots 0.5\,\mathrm{mN}$	Spanwise force component (vertical)
General parameters			
Re	$:=$	vL/ν	
	$=$	$0\ldots 10^4$	Ratio of inertial forces to viscous forces
Ha	$:=$	$B_0 L \sqrt{\sigma/(\rho\nu)}$	
	$=$	$1\ldots 270$	Ratio of electromagnetic forces to viscous forces
N	$:=$	Ha^2/Re	
	$=$	$0\ldots 57.9$	Ratio of electromagnetic forces to inertial forces
Rm	$:=$	$\mu_0 \sigma v L$	
	$=$	$0\ldots 0.015$	Ratio of advection of magnetic field lines to their diffusion

Table A.1: Overview of the parameters accessed with at least one of the two setups. Top category: Material parameters and duct dimensions that are fixed for each setup. Second category: Adjustable input parameters. Third category: Dependent output parameters. Bottom category: Nondimensional parameters classifying the MHD regimes covered by the combined experiments. Where two parameters are given, the first refers to the old duct setup and the second to the new duct setup.

B List of Changes to the Experimental Setup

	Preliminary Setup	Final Setup
Test section		
Inside cross section (w×h×l)	$10.8\,\mathrm{cm} \times 2\,\mathrm{cm} \times 90\,\mathrm{cm}$	$5\,\mathrm{cm} \times 5\,\mathrm{cm} \times 80\,\mathrm{cm}$
Wall thickness	$8\,\mathrm{mm}$	$5\,\mathrm{mm}$
Characteristic length scale	$1\,\mathrm{cm}$	$2.5\,\mathrm{cm}$
Bellows	no	yes
Lids	loose	fixed with clamps
Motor		
Input	manual with turn-dial	via computer in steps of $1\,\mathrm{rpm}$
Maximum flow velocity	$13.6\,\mathrm{cm/s}$	$13.6\,\mathrm{cm/s}$
Repeatability	$1\,\mathrm{cm/s}$	$< 0.1\,\mathrm{cm/s}$
Placement	same table as duct	separate stand
Force measurement system		
Placement	same table as duct below test section	separate stand on stone beside test section
Resolution	$10\,\mathrm{\mu N}$	$0.015\,\mathrm{\mu N}$
Maximum dead load	$1.5\,\mathrm{N}$	$0.25\,\mathrm{N}$
Repeatability	$36\,\%$	$4\,\%$
Reproducibility	$50\,\%$	$20\,\%$
Temporal resolution	$5\,\mathrm{Hz}$	$6\,\mathrm{Hz}$
Positioning system		
Input of *relative* position	manual	automatic
Repeatability of z	$1\,\mathrm{mm}$	$< 0.05\,\mathrm{mm}$

Table B.1: Overview of the improvements that have been implemented in the new duct setup. Test section, motor, force measurement system, and positioning system have been replaced. The geometry of the test section has been adjusted to match the geometry of the two other groups of the RTG, and the wall thickness has been decreased to increase the maximum achievable forces. The bellows have been introduced to decouple the thin-walled plexiglass test section from the heavy steel pipe system. The new motor has been moved from the table where the duct is placed, to an extra stand beside the table to reduce the transmission of motor vibrations over the pipe system to the measurement system. Additionally, the new motor runs more smoothly and is more easily controlled than the old motor. Further changes are the replacement of the force measurement and positioning system, increasing not only the resolution of the force but also the force itself and decreasing the uncertainty of the measured values. In the new setup, all components (positioning, motor control, force recording) can be controlled remotely via computer, reducing noise from the presence of an experimentalist.

C Measurement Procedure

Below is an outline of the standard procedure that was found to be best for conducting measurements at the liquid metal duct:

1. The measurement system is turned on well before the start of the measurement, at least 24 hours, to allow the electronics to warm up.

2. The GaInSn level inside the duct is checked at the 1 cm-gap in the lid. It should be such that the lids are just not lifted off the sidewalls (without clamps) or just above the bottom of the lids (tightened clamps). This typically needs to be adjusted before a new measurement series. Additionally, the GaInSn must be checked regularly for build-up of foam inside the duct; this foam must be replaced with liquid GaInSn. The generation of foam is especially strong when the duct has been re-filled recently and the pump is operated at high speeds over several hours.

3. The magnet system must be checked to yield a proper signal, i.e. the magnet must be oscillating freely.

4. A short test run is performed at $\omega = 70$ rpm, and the magnet is placed as close to the duct as possible. The motor must be running, as the duct vibrations at 70 rpm make an extra space of approx. 0.1 mm necessary. It can be seen immediately from the output force signal when the magnet touches the duct wall.

5. The first measurement step is always with still motor to obtain the zero signal.

6. Next, the motor is set to its final rotation speed in steps of no more than 10 rpm.

7. Afterwards, the automated positioning system is activated to move the magnet along z (changes distance to duct) or y (changes vertical position).

8. The waiting time between the positions is a trade-off between the advantage of long and therefore statistically utilizable time series and the disadvantage of possible thermal drifts that can be avoided or at least deducted for measurement series of only a few hours. A 50-s-waiting time yields a total measurement time of 2.5 hrs (z-variation) or 3 hrs (y-variation); if not for irregular outside disturbances, the drift of the signal can almost always be avoided. The sampling frequency is 6.35 Hz. Minus a few seconds dead time during which the magnet is moved, the 50-s-period gives around 250 values. As the spanwise force signal is low compared to the random fluctuations, a longer waiting time seems appropriate for F_y-measurements. The longer waiting period, however, is bought with the high chance of thermal drifts (and other disturbances) obscuring the actual signal and enforcing a repetition of the measurement series.

Bibliography

[1] B.G. Lipták. *Flow Measurement*. CRC Press, 1993.

[2] VDI-Book. *Strömungsmesstechnik*. Springer, 2006.

[3] R. Miller. *Flow Measurement Engineering Handbook*. McGraw-Hill Professional, 1996.

[4] C.G. Lomas. *Fundamentals of Hot Wire Anemometry*. Cambridge University Press, reissue edition, 2011.

[5] H.H. Bruun. *Hot-Wire Anemometry: Principles and Signal Analysis*. Oxford University Press, 1995.

[6] H.-E. Albrecht, N. Damaschke, M. Borys, and C. Tropea. *Laser Doppler and Phase Doppler Measurement Techniques*. Experimental Fluid Mechanics. Springer, 2002.

[7] M. Raffel, C.E. Willert, S.T. Wereley, and J. Kompenhans. *Particle Image Velocimetry: A Practical Guide*. Experimental Fluid Mechanics. Springer, 2007.

[8] K. C. Mills and R. F. Brooks. Measurements of thermophysical properties in high temperature melts. *Materials Science and Engineering*, A178:77–81, 1994.

[9] Y. Kolesnikov, C. Karcher, and A. Thess. Lorentz Force Flowmeter for liquid aluminum: Laboratory experiments and plant tests. *Metall. Mater. Trans. B*, 42(3), 2011.

[10] C. Weidermann, A. Thess, D. Lieftucht, and M. Reifferscheid. Application of Lorentz Force Velocimetry (LFV) in continuous casting of steel. Key note lecture at the 5th International Congress on the Science and Technology of Steelmaking, Dresden, 2012.

[11] B.G. Thomas. *Modeling for Casting and Solidification Processing*, chapter 15, pages 499–540. Materials Engineering. Marcel Dekker, 2001.

[12] F. Fuhr, C. Cicutti, G. Walter, and G. Torga. Relationship between nozzle deposits and inclusion composition in the continuous casting of steels. *Iron & Steelmaker*, pages 53–58, December 2003.

[13] C. G. Dudczig, S.; Aneziris. Werkstoff- und Prozessevaluierung von Feuerfestsystemen in einem Stahlgusssimulator. Freiberger Feuerfestforum, 2010.

[14] S. Tympel. *Magnetohydrodynamic duct flow in the presence of a magnetic dipole*. PhD thesis, Ilmenau University of Technology, 2012.

[15] G. Pulugundla. *Numerical Modelling of Liquid Metal Flows Interacting with Strongly Inhomogeneous Magnetic Fields*. PhD thesis, Ilmenau University of Technology, 2012.

[16] J. A. Shercliff, editor. *The Theory of Electromagnetic Flow Measurement*. Cambridge University Press, 1962.

[17] A. Thess, E. Votyakov, B. Knaepen, and O. Zikanov. Theory of the Lorentz force flowmeter. *New Journal of Physics*, 9(8):299, 2007.

[18] J. D. Jackson. *Classical Electrodynamics.* Wiley, New York, 3rd edition, 1998.

[19] P. H. Roberts, editor. *An Introduction to Magnetohydrodynamics.* American Elsevier Publishing Company, Inc., New York, 1967.

[20] R.J. Moreau. *Magnetohydrodynamics.* Fluid mechanics and its applications. Kluwer Academic Publishers, 1990.

[21] P. A. Davidson. *An Introduction to Magnetohydrodynamics.* Cambridge University Press, 2006.

[22] L. Bogan C. S. MacLatchy, P. Backman. A quantitative magnetic braking experiment. *American Journal of Physics*, 61(12), 1993.

[23] A. Thess, E. Votyakov, and Y. Kolesnikov. Lorentz Force Velocimetry. *Physical Review Letters*, 96(16):164501, 2006.

[24] L. C. Hoagland. *Fully Developed Turbulent Flow in Straight Rectangular Ducts – Secondary Flow, Its Cause and Effect On The Primary Flow.* PhD thesis, Massachusetts Institute of Technology, September 1960.

[25] G.K. Batchelor. *An Introduction to Fluid Dynamics.* Cambridge Mathematical Library. Cambridge University Press, 2000.

[26] I. Tosun, D. Uner, and C. Ozgen. Critical Reynolds number for Newtonian flow in rectangular ducts. *Industrial & Engineering Chemistry Research*, 27:1957, 1988.

[27] R. W. Hanks and H.-C. Ruo. Laminar-turbulent transition in ducts of rectangular cross section. *I&EC Fundamentals*, 5(4):558–561, 1966.

[28] B. Hof, J. Westerweel, T. M. Schneider, and B. Eckhardt. Finite lifetime of turbulence in shear flows. *Nature*, 443(7):59–62, 2006.

[29] K. Avila, D. Moxey, A. de Lozar, M. Avila, D. Barkley, and B. Hof. The onset of turbulence in pipe flow. *Science*, 333:192–196, 2011.

[30] B. Eckhardt. A critical point for turbulence. *Science*, 333:165–166, 2011.

[31] Y. A. Cengel and R. H. Turner. *Fundamentals of Thermal-Fluid Sciences.* McGraw-Hill Science/Engineering/Math, 2nd edition, 2004.

[32] C. C. T. Pringle and R. R. Kerswell. Asymmetric, helical, and mirror-symmetric traveling waves in pipe flow. *Physical Review Letters*, 99, 2007.

[33] A. Melling and J.H. Whitelaw. Turbulent flow in a rectangular duct. *Journal of Fluid Mechanics*, 78(2):289–315, 1976.

[34] C. Pozrikidis, editor. *Introduction to Theoretical and Computational Fluid Dynamics.* Oxford University Press, 1997.

[35] R.J. Garde. *Turbulent Flow.* John Wiley & Sons, 1994.

[36] M. H. Buschmann and M. Gad-el Hak. Turbulent boundary layers: reality and myth. *International Journal of Computing Science and Mathematics*, 1(2-4):159–176, 2008.

[37] S.H. Maslen. Transverse velocities in fully developed flows. *Quarterly of Applied Mathematics*, 16:173, 1958.

[38] R. Moissis. Secondary flow in rectangular ducts. Master's thesis, Massachusetts Institute of Technology, June 1957.

[39] J. Nikuradse. Turbulente Strömungen in nicht kreisförmigen Rohren. *Ingenieur-Archiv*, 1:306–332, 1930.

[40] L. Prandtl. *Ludwig Prandtl – Gesammelte Abhandlungen. Zweiter Teil.*, chapter Über die ausgebildete Turbulenz, pages 736–751. 1961. First published in: Verhandlungen des II. Internationalen Kongresses für Technische Mechanik, Zurich, 1926.

[41] F. B. Gessner. Origin of secondary flow in turbulent corner flow. *Journal of Fluid Mechanics*, 58(1):1–25, 1973.

[42] E. Brundrett and W.D. Baines. The production and diffusion of vorticity in duct flow. *Journal of Fluid Mechanics*, 19:375–394, 1964.

[43] B. Galletti and A. Bottaro. Large-scale secondary structures in duct flow. *Journal of Fluid Mechanics*, 512:85–94, 2004.

[44] S. Gavrilakis. Numerical simulation of low Reynolds-number turbulent flow through a straight square duct. *Journal of Fluid Mechanics*, 244:101–129, 1992.

[45] V. Strouhal. Über eine besondere Art der Tonerregung. *Annalen der Physik*, 241(10):216–251, 1878.

[46] C.H.K. Williamson. Vortex dynamics in the cylinder wake. *Annual Review of Fluid Mechanics*, 28:477–539, 1996.

[47] L. Prandtl. *Ludwig Prandtl – Gesammelte Abhandlungen. Zweiter Teil.*, chapter The Generation of Vortices in Fluids of Small Viscosity, pages 752–777. 1961. First published in: Wilbur Wright Memorial Lecture, 16th May, 1927 and Royal Aeronautical Society, Vol. 31, pp. 720-743, 1927.

[48] A.H. Techet. Lecture notes: 13.42 vortex induced vibrations. Online: http://ocw.mit.edu (retrieved on 2012-09-25), April 2005.

[49] A. Roshko. On the development of turbulent wakes from vortex streets. Technical report, California Institute of Technology, 1954. Report 1191 to the National Advisory Committee For Aeronautics.

[50] L. Ong and J. Wallace. The velocity field of the turbulent very near wake of a circular cylinder. *Experiments in Fluids*, 20:441–453, 1996.

[51] L. Zovatto and G. Pedrizzetti. Flow about a circular cylinder between parallel walls. *Journal of Fluid Mechanics*, 440(1-25), 2001.

[52] K. Thorne. Lecture notes: Chapter 18: Magnetohydrodynamics. Online: http://www.pma.caltech.edu (retrieved on 2012-11-16), March 2005.

[53] S. Molokov, R. Moreau, and K. Moffatt. *Magnetohydrodynamics – Historical Evolution and Trends.* Fluid Mechanics And Its Applications. Springer, 2007.

[54] B. A. Sivak, V. G. Grachev, V. M. Parshin, A. D. Chertov, S. V. Zarubin, V. G. Fisenko, and A. A. Solovev. Magnetohydrodynamic processes in the electromagnetic mixing of liquid phase in the ingot on continuous bar- and bloom-casting machines. *Steel in Translation*, 39(9):774–782, 2009.

[55] C. T. Russell. *Correlated Interplanetary and Magnetopsheric Observations*, chapter The Solar Wind and Magnetospheric Dynamics, pages 3–47. D. Reidel Publishing Co., Dordrecht, Holland, 1974.

[56] ESA. Electrifying aurorae. Online: http://sci.esa.int/science-e (retrieved on 2012-11-16), May 2003.

[57] ESA. Plasma regions – the auroral zone. Online: http://sci.esa.int/science-e (retrieved on 2012-11-16), month = November, year = 2010.

[58] K. Schlegel. *Vom Regenbogen zum Polarlicht: Leuchterscheinungen in der Atmosphäre*. Spektrum Akademischer Verlag, 2001.

[59] A. Otto. Lecture notes: Magnetospheric physics. Online: http://how.gi.alaska.edu/ao/msp/ (retrieved on 2011-10-11), May 2006.

[60] D. Hampton. Why are we still studying the aurora? Presentation at Physics Dept. Journal Club of the University of Alaska Fairbanks, November 2011.

[61] S. W. H. Cowley. Earth's plasma environment: Magnetic reconnection and its effect on magnetospheric fields and flows. *Philosophical Transactions: Physical Sciences and Engineering*, 349(1690):237–247, 1994.

[62] E. G. Zweibel and M. Yamada. Magnetic reconnection in astrophysical and laboratory plasmas. *Annual Review of Astronomy and Astrophysics*, 47:291–332, 2009.

[63] W. I. Axford. Connection and reconnection. *Advances in Space Research*, 29(7):1025–1033, 2002.

[64] S.J. Schwartz, C.J. Owen, and D. Burgess. Lecture notes: Astrophysical plasmas. Online: www.sp.ph.ic.ac.uk (retrieved on 2011-12-12), January 2004.

[65] V.P. Pavlenko and L. Rosenqvist. *Fluid Mechanics. Compendium.* Dpt. of Astronomy and Space Physics, Uppsala University, 3 edition, 2008.

[66] J. Hartmann. Hg-dynamics I. Theory of the laminar flow of an electrically conductive liquid in a homogeneous magnetic field. *Kongelige Danske Videnskabernes Selskab: Matematisk-fysiske Meddelelser*, 15(6):1–28, 1937.

[67] J. Hartmann and F. Lazarus. Hg-dynamics II. Experimental investigations on the flow of mercury in a homogeneous magnetic field. *Kongelige Danske Videnskabernes Selskab. Matematisk-fysiske Meddelelser*, 15(7):1–45, 1937.

[68] S. Cuevas, S. Smolentsev, and M. A. Abdou. On the flow past a magnetic obstacle. *Journal of Fluid Mechanics*, 553:227–252, 2006.

[69] E. V. Votyakov and S.C. Kassinos. On the analogy between streamlined magnetic and solid obstacles. *Physics of Fluids*, 21(097102), 2009.

[70] B. Thomas and R. Chaudhary. State of the art in electromagnetic flow control in continuous casting of steel slabs: Modeling and plant validation. In *6th International Conference on Electromagnetic Processing of Materials (EPM)*, Dresden, 2009.

[71] K. Timmel, X. Miao, S. Eckert, D. Lucas, and G. Gerbeth. Experimental and numerical modelling of the steel flow in a continuous casting mould under the influence of a transverse DC magnetic field. *Magnetohydrodynamics*, 46(4):437–448, 2010.

[72] M. Faraday. The bakerian lecture: Experimental researches in electricity. second series. *Philosophical Transactions of the Royal Society*, 122:175, 1832.

[73] C. Wollaston. Tidally induced emf's in cables. *Journal of the Society of Telegraph Engineers and of Electricians*, 10:50, 1881.

[74] H. Ryckborst and R. O. Christie. Feasibility of electromagnetic streamflow measurements using the earth's magnetic field. *Hydrological Sciences*, 22(2):241–255, 1977.

[75] F. Hofmann. Fundamental principles of electromagnetic flow measurement. Technical report, KROHNE Messtechnik GmbH & Co. KG, 2003.

[76] W. Hogrefe. Design questions with the implementation of magnet-inductive flow meters. III. *Regelungstechnische Praxis*, 21(11):331, 1979.

[77] W. L. Engl. Der induktive Durchflußmesser mit inhomogenem Magnetfeld – Teil I. Allgemeine Grundlagen und Lösung des ebenen Problems. *Electrical Engineering*, 53(6):344–359, 1970.

[78] V. Minchenya, C. Karcher, Y. Kolesnikov, and A. Thess. Lorentz force flow meter in industrial application. *Magnetohydrodynamics*, 45(3):459–465, 2009.

[79] G. Pulugundla, C. Heinicke, C. Karcher, and A. Thess. Lorentz force velocimetry with a small permanent magnet. Accepted for publication in European Journal of Mechanics - B/Fluids.

[80] J. Priede, D. Buchenau, and G. Gerbeth. Force-free and contactless sensor for electromagnetic flowrate measurements. *Magnetohydrodynamics*, 45(3):451–458, 2009.

[81] J. Priede, D. Buchenau, and G. Gerbeth. Single-magnet rotary flowmeter for liquid metals. *Journal of Applied Physics*, 110(3), 2011.

[82] I. Bucenieks. Perspectives of using rotating permanent magnets in the design of electromagnetic induction pumps. *Magnetohydrodynamics*, 36(2), 2000.

[83] H. Lehde and W.T. Lang. Device for measuring rate of fluid flow. Patent US 2,435,043, 1948.

[84] C. C. Feng, W. E. Deeds, and C. V. Dodd. Analysis of eddy-current flowmeters. *Journal of Applied Physics*, 46(7):2935–2940, 1975.

[85] D. E. Wiegand. Summary of an analysis of the eddy-current flowmeter. *IEEE Transactions on Nuclear Science*, 15(1):28–36, 1968.

[86] D. E. Wiegand and C.W. Michels. Performance tests on an eddy-current flowmeter. *IEEE Transactions on Nuclear Science*, 16(1):192–195, 1969.

[87] S. Poornapushpakala, C. Gomathy, J.I. Sylvia, B. Krishnakumar, and P. Kalyanasundaram. *An analysis on eddy current flowmeter – A review.* In: Recent Advances in Space Technology Services and Climate Change (RSTSCC), conference proceedings: 185-188. 2010.

[88] J. Priede, D. Buchenau, and G. Gerbeth. Contactless electromagnetic phase-shift flowmeter for liquid metals. *Measurement Science and Technology*, 22(5), 2011.

[89] J. Baumgartl, A. Hubert, and G. Müller. The use of magnetohydrodynamic effects to investigate fluid flow in electrically conducting melts. *Physics of Fluids A*, 5(12):3280–3289, 1993.

[90] F. Stefani, T. Gundrum, and G. Gerbeth. Contactless Inductive Flow Tomography. *Physical Review E*, 70(5):056306, 2004.

[91] W. Yin, A. J. Peyton, F. Stefani, and G. Gerbeth. Theoretical and numerical approaches to the forward problem and sensitivity calculation of a novel contactless inductive flow tomography (CIFT). *Measurement Science and Technology*, 20(105503), 2009.

[92] T. Gundrum, G. Gerbeth, F. Stefani, and M. Xu. Experimental aspects of contactless inductive flow tomography. *Magnetohydrodynamics*, 42(2-3):153–160, 2006.

[93] T. Wondrak, V. Galindo, G. Gerbeth, T. Gundrum, F. Stefani, and K. Timmel. Contactless inductive flow tomography for a model of continuous steel casting. *Measurement Science and Technology*, 21(045402), 2010.

[94] T. Schulenberg and R. Stieglitz. Experimental techniques for heavy liquid metals. In *Proceedings of the workshop on Experiments and CFD Code Application to Nuclear Reactor Safety (XCFD4NRS), Grenoble, France, 10-12 September 2008.*

[95] R. Stieglitz. *Handbook on Lead-Bismuth Eutectic Alloy and Lead Properties, Materials Compatibility, Thermal-hydraulics and Technologies*, chapter 11. Instrumentation. Nuclear Energy Agency (NEA), 2007.

[96] R. Ricou and C. Vives. Local velocity and mass transfer measurements in molten metals using an incorporated magnet probe. *International Journal of Heat and Mass Transfer*, 25:1579–1588, 1982.

[97] T. v. Weißenfluh. Probes for local velocity and temperature measurements in liquid metal flow. *International Journal of Heat and Mass Transfer*, 28(8):1563–1574, 1985.

[98] B.P. Axcell and A. Walton. Thermoelectric effects in miniature permanent magnet probes used for velocity measurement in flowing sodium. *Experimental Thermal and Fluid Science*, 6(3):309–323, 1993.

[99] J.U. Knebel and L. Krebs. Calibration of a miniature permanent magnet flowmeter probe and its application to velocity measurements in liquid sodium. *Experimental Thermal and Fluid Science*, 8(2):135–148, 1994.

[100] U. Müller, R. Stieglitz, and S. Horanyi. Experiments at a two-scale dynamo test facility. *Journal of Fluid Mechanics*, 552:419–440, 2006.

[101] Y. Takeda. Measurement of velocity profile of mercury flow by ultrasound Doppler shift method. *Nuclear Technology*, 79:120–124, 1987.

[102] S. Eckert, G. Gerbeth, and V.I. Melnikov. Velocity measurements at high temperatures by ultrasound Doppler velocimetry using an acoustic wave guide. *Experiments in Fluids*, 35:381–388, 2003.

[103] V. Minchenya, C. Karcher, Y. Kolesnikov, and A. Thess. Calibration of the Lorentz force flowmeter. *Flow Measurement and Instrumentation*, 22:242–247, 2011.

[104] M. Gramß and C. Karcher. Calibration of a Lorentz force flowmeter. In *Contribution to the 56th International Scientific Colloquium at Ilmenau University of Technology, 2011.*

[105] M. Gramß. Project ForMaT. Calibration of a Lorentz force flowmeter . Progress Report for the 3rd Closed Session of the Research Training Group "Lorentz Force Velocimetry and Lorentz Force Eddy Current Testing", 21-24 May 2012, Decin, 2012.

[106] C. Weidermann. *Design and laboratory test of a Lorentz force flowmeter for pipe flows.* PhD thesis, Ilmenau University of Technology, 2012.

[107] A. Viré, B. Knaepen, and A. Thess. Lorentz Force Velocimetry based on time-of-flight measurements. *Physics of Fluids*, 22(125101), 2010.

[108] D. Jian and C. Karcher. Electromagnetic flow measurements in liquid metals using time-of-flight Lorentz Force Velocimetry. *Measurement Science and Technology*, 23(074021), 2012.

[109] A. Wegfraß, C. Diethold, M. Werner, T. Fröhlich, B. Halbedel, F. Hilbrunner, C. Resagk, and A. Thess. A universal noncontact flowmeter for liquids. *Appl. Phys. Lett.*, 100(194103), 2012.

[110] A. Alferenok, M. Werner, M. Gramß, U. Lüdtke, and B. Halbedel. Numerical optimization of the magnet system for the Lorentz Force Velocimetry of electrolytes. *International Journal of Applied Electromagnetics and Mechanics*, 38:79–92, 2012.

[111] A. Wegfraß, C. Diethold, M. Werner, C. Resagk, T. Fröhlich, B. Halbedel, and A. Thess. Flow rate measurement of weakly conducting fluids using Lorentz Force Velocimetry. *Measurement Science and Technology*, 23(105307), 2012.

[112] T. Hibiya and I. Egry. Thermophysical property measurements of high temperature melts: results from the development and utilization of space. *Measurement Science and Technology*, 16:317–326, 2005.

[113] H.-J. Fecht, R. Wunderlich, L. Battezzati, J. Etay, E. Ricci, S. Seetharaman, and I. Egry. Thermophysical properties of materials. *Europhysics News*, 39(5):19–21, 2008.

[114] T. Iida and R.I.L. Guthrie. *The Physical Properties of Liquid Metals.* Clarendon Press, 1988.

[115] M.J. Assael, K. Kakosimos, R.M. Banish, J. Brillo, Ivan Egry, R. Brooks, P.N. Quested, K.C. Mills, A. Nagashima, Y. Sato, and W.A. Wakeham. Reference data for the density and viscosity of liquid aluminum and liquid iron. *Journal of Physical and Chemical Reference Data*, 35(1):285–300, 2006.

[116] Gerbeth G. and Fautrelle Y., editors. *Proceedings of the 6th International Conference on Electro-magnetic Processing of Materials, 19-23 October 2009, Dresden, Germany, www.epm-2009.de*, 2009.

[117] Brodova I.G., Popel P.S., and Eskin G.I. *Liquid Metal Processing.* Taylor & Francis, New York, 2002.

[118] B. J. Monaghan. A four-probe DC method for measuring the electrical resistivities of molten metals. *International Journal of Thermophysics,*, 20(2):677–690, 1999.

[119] Y. Plevachuk, V. Sklyarchuk, W. Hoyer, and I. Kaban. Electrical conductivity, thermoelectric power and viscosity of liquid Sn-based alloys. *Journal of Materials Science*, 41:4632–4635, 2006.

[120] Y. Plevachuk, V. Sklyarchuk, A. Yakymovych, S. Eckert, B. Willers, and K. Eigenfeld. Density, viscosity, and electrical conductivity of hypoeutectic Al-Cu liquid alloys. *Metallurgic and Materials Transactions A*, 39A:3040–3045, 2008.

[121] W. Braunbek. Eine neue Methode elektrodenloser Leitfähigkeitsmessung. *Zeitschrift für Physik*, 73:312–334, 1932.

[122] S. G. Teodorescu, R. A. Overfelt, and S. I. Bakhtiyarov. An inductive technique for electrical conductivity measurements on molten metals. *International Journal of Thermophysics*, 22(5):1521–1535, 2001.

[123] S. I. Bakhtiyarov, R. A. Overfelt, and S. G. Teodorescu. Electrical and thermal conductivity of A319 and A356 aluminum alloys. *Journal of Materials Science*, 36:4643–4648, 2001.

[124] C. Li, H. Ban, B. Lin, R. N. Scripa, C.-H. Su, S. L. Lehoczky, and S. Zhu. Transient torque method: A fast and nonintrusive technique to simultaneously determine viscosity and electrical conductivity of semiconducting and metallic melts. *Review of Scientific Instruments*, 75(9):2810–2816, 2004.

[125] I. Egry, G. Lohöfer, and S. Sauerland. Measurements of thermophysical properties of liquid metals by noncontact techniques. *International Journal of Thermophysics*, 14(3):573–584, 1993.

[126] I. Egry, G. Lohöfer, and S. Sauerland. Measurements of thermophysical properties of liquid metals relevant to Marangoni effects. *Philosophical Transactions of the Royal Society London A*, 356:845–856, 1998.

[127] T. Richardsen. *Ein induktives Messverfahren zur Bestimmung der elektrischen Leitfähigkeit an unterkühlten Metallschmelzen.* PhD thesis, RWTH Aachen, July 2001.

[128] Y. Kolesnikov, A. Thess, and C. Heinicke. Erfindungsmeldung für ein mobiles Lorentz-Force-Sigmometer (M-LOFOS): Verfahren und Vorrichtung zur Messung der elektrischen Leitfähigkeit von Flüssigmetallen. Patent application, July 2012.

[129] Y. Kolesnikov and A. Thess. Non-contact measurement of electrical conductivity using lorentz forces: Lorentz Force Sigmometry. Technical report, Ilmenau University of Technology, September 2011.

[130] C. Heinicke, S. Tympel, G. Pulugundla, I. Rahneberg, T. Boeck, and A. Thess. Interaction of a small permanent magnet with a liquid metal duct flow. *Journal of Applied Physics*, 112:124914, 2012.

[131] S. Abt. Konstruktion eines Flüssigmetall-Kanalabschnitts für experimentelle Arbeiten. Project work, October 2010.

[132] I. Rahneberg. A2 / Multi-component force measurement systems. Progress Report for the 1st Closed Session of the Research Training Group "Lorentz Force Velocimetry and Lorentz Force Eddy Current Testing", 25-27 May 2010, Heyda, 2010.

[133] I. Rahneberg. A2 / Multi-component force measurement systems. Progress Report for the 2nd Closed Session of the Research Training Group "Lorentz Force Velocimetry and Lorentz Force Eddy Current Testing", 09-13 March 2011, Kleinwalsertal, 2011.

[134] M. Münster. Measurements of local velocities in spiraling pipe flows of liquid metals. Master's thesis, Ilmenau University of Technology, January 2012.

[135] R. Füßl. Interferenzoptische Kraftsensoren für den Lastbereich bis 0,1 Newton. Habilitation, Ilmenau University of Technology, 2007.

[136] R. Füßl and G. Jäger. The influence of the force feed-in system on high-accuracy low force measurement. XIX IMEKO World Congress – Fundamental and Applied Metrology, Lisbon, Portugal, September 6?11, 2009 2009.

[137] C. Heinicke. Measurements at the liquid metal duct with the preliminary magnet system. Scientific report, Ilmenau University of Technology, 2010.

[138] J. A. Shercliff. Experiments on the dependence of sensitivity on velocity profile in electromagnetic flowmeters. *Journal of Scientific Instruments*, 32:441–442, 1955.

[139] J. A. Shercliff. Relation between the velocity profile and the sensitivity of electromagnetic flowmeters. *Journal of Applied Physics*, 25(6):817–818, 1954.

[140] Krohne. Magnetisch-induktive Durchflussmesser. Montageanleitung. Installation Instructions, May 1998.

[141] L. Kirkup and B. Frenkel. *An Introduction to Uncertainty in Measurement*. Cambridge University Press, 2006.

[142] C. Weidermann. private communications, September 2012.

[143] C. Heinicke. Spatially resolved measurements in a liquid metal flow with Lorentz Force Velocimetry. Accepted for publication in Experiments in Fluids.

[144] A. Thess. Comment on "primary instability mechanisms on the magnetohydrodynamic boundary layer flow over a rotating disk subject to a uniform radial flow". *Physics of Fluids*, 22(029102), 2010.

[145] A. Thess. Comment on "oblique axisymmetric stagnation flows in magnetohydrodynamics". *Physics of Fluids*, 20(069102), 2008.

[146] R.-P. Uhlig. *Identification of Material Defects in Metallic Materials Using Lorentz Force Eddy Current Testing – Fundamentals, Metrological Implementation and Verification*. PhD thesis, Ilmenau University of Technology, 2012.

Acknowledgments

However, no one walks alone on the journey of life. The success of any project depends largely on the encouragement and guidelines of many others. I take this opportunity to express my gratitude to the people who have been instrumental in the successful completion of this thesis.

First I would like to thank my supervisor André Thess for his valuable guidance and advice even before the start of this particular project. I appreciate the freedom you permitted me and your contagious enthusiasm that helped me over initially unyielding results. My second supervisor, Christian Karcher, deserves my gratitude for his constant support.

My time in the lab would have been much more frustrating if it had not been for the abundant help and technical assistance by Eckhart Roth, for Michel Rivero's help with Labview, and the ever optimistic Ilko Rahneberg who always patiently explained even the most obvious technical details to me.

Over the years, I enjoyed the continuing support of the members of my group, the Institute of Thermo- and Fluid Dynamics. Out of these, I would particularly like to thank Gautam Pulugundla and Saskia Tympel for the many vivid and fruitful discussions. Christian Weidermann often made me feel like I had plenty of time compared to him, typically by depriving me of mine. Thank you, André Wegfraß, for sharing your troubles with your experimental setup and making me feel relieved about how comparably easy-going my experiment is. And, thank you, Farzaneh Samsami for being the only one to return equipment to lab R122 after borrowing.

I also owe my gratitude to Antonius Otto and his student Tapas Bhattacharya (well, and to Miss Aurora) for making my stay in Fairbanks as wonderful as it was. For the times when I was not traveling the world I am indebted to my office mate Matthias Müller for his technical, software, and day-to-day support.

Finally, I would like to thank Hanjo Hamann for distracting me from time to time, for confusing my juridical world view, and for resisting the urge to strangle, bury, and desert me on my bitchy days. And really, me falling asleep during a movie does not imply the movie is bad. Also, I thank my parents and Anton for raising me like they did.

Erklärung

gemäß Anlage 1 der Siebten Änderung der Promotionsordnung der TU Ilmenau – Allgemeine Bestimmungen

Ich versichere, dass ich die vorliegende Arbeit ohne unzulässige Hilfe Dritter und ohne Benutzung anderer als der angegebenen Hilfsmittel angefertigt habe. Die aus anderen Quellen direkt oder indirekt übernommenen Daten und Konzepte sind unter Angabe der Quelle gekennzeichnet.

Bei der Auswahl und Auswertung folgenden Materials haben mir die nachstehend aufgeführten Personen in der jeweils beschriebenen Weise unentgeltlich geholfen:

- Prof. André Thess sowie

- PD Dr.-Ing. habil. Christian Karcher haben mich fachlich betreut.

- Dipl.-Ing. Marian Münster hat für seine Masterarbeit Messungen mit dem 2D-Dehnmessstreifensystem durchgeführt und ausgewertet.

- B.Sc. Seyed Omid Taghizadeh Motlagh hat als wissenschaftliche Hilfskraft Geschwindigkeitsmessungen mit dem UDV durchgeführt.

Weitere Personen waren an der inhaltlich-materiellen Erstellung der vorliegenden Arbeit nicht beteiligt. Insbesondere habe ich hierfür nicht die entgeltliche Hilfe von Vermittlungs- bzw. Beratungsdiensten (Promotionsberater oder anderer Personen) in Anspruch genommen. Niemand hat von mir unmittelbar oder mittelbar geldwerte Leistungen für Arbeiten erhalten, die im Zusammenhang mit dem Inhalte der vorgelegten Dissertation stehen.

Die Arbeit wurde bisher weder im In- noch im Ausland in gleicher oder ähnlicher Form einer Prüfungsbehörde vorgelegt.

Ich bin darauf hingewiesen worden, dass die Unrichtigkeit der vorstehenden Erklärung als Täuschungsversuch bewertet wird und gemäß § 7 Abs. 10 der Promotionsordnung den Abbruch des Promotionsverfahrens zur Folge hat.

Ilmenau, 21.11.2012